DEVELOPMENT OF A NOVEL MODEL-INDEPENDENT MONITORING AND ANALYZING SYSTEM TO TACKLE VARIOUS OSCILLATIONS IN HIGH POWER ELECTRONIC CONVERTER-PENETRATED POWER SYSTEMS

HU YONG

PhD

The Hong Kong Polytechnic University

2023

The Hong Kong Polytechnic University

Department of Electrical Engineering

Development of A Novel Model-independent Monitoring and Analyzing System to Tackle Various Oscillations in High Power Electronic Converter-penetrated Power Systems

HU YONG

A thesis submitted in partial fulfillment of the requirements for the degree of Doctor of Philosophy

August 2022

CERTIFICATE OF ORIGINALITY

I hereby declare that this thesis is my own work and that, to the best of my knowledge and belief, it reproduces no material previously published or written, nor material that has been accepted for the award of any other degree or diploma, except where due acknowledgement has been made in the text.

_____(Signed)

__HU Yong__(Name of student)

Abstract

The investigation of various oscillations is crucial for the stable operation of high power electronic converter (PEC)-penetrated power systems. In order to tackle the various oscillations, a precise system modeling would be important. The commonly-used modeling-based methods include the damping torque analysis (DTA) and modal analysis (MA). However, the large quantities of system components make the system modeling nearly an impossible task. To date, the energy flow analysis (EFA) has been applied in the stability analysis of power grids, which is based on the measurement technology. Nevertheless, the existing research of EFA is still insufficient. Specifically, the relationship between EFA and the modeling-based methods (i.e., DTA and MA) is not essentially revealed. Moreover, EFA is mainly used for monitoring and analyzing the oscillations of synchronous generator-dominated power grids, but has not been extended and generalized to that of PEC-penetrated power systems.

In this thesis, firstly, the connection between DTA and EFA are systematically examined and revealed for the better understanding of the oscillatory damping mechanism of the electromechanical oscillation. Specifically, the concepts of the aggregated damping torque coefficient and frequency-decomposed energy attenuation coefficient are proposed and derived. On this basis, the frequency spectrum analysis of the energy attenuation coefficient is employed to rigorously prove that the results of DTA and EFA are essentially equivalent, which is valid for arbitrary models of

synchronous generators in multi-machine power systems.

Secondly, a novel EFA is proposed based on the signal reconstruction and decomposition to quantitatively investigate the electromechanical oscillations in multi-machine power systems. Specifically, the time-domain implementation (TDI) and frequency-domain implementation (FDI) of the proposed EFA are designed. On this basis, the consistency between the proposed EFA and MA is strictly proved, which is applicable for arbitrary models of synchronous generators in the multi-machine environment. Also, the application procedure of the proposed EFA in monitoring and analyzing the electromechanical oscillations is given.

Thirdly, as a major part of the full converter-based wind generation (FCWG), the potential dynamics of the permanent magnet synchronous generator (PMSG) can be utilized to improve the oscillatory stability of the PEC-penetrated power grid with the introduction of the auxiliary resonance controller (ARC) to the machine-side control of FCWG. However, the machine-side oscillations (MSOs) of FCWG would also be complicated. Thus, the proposed EFA is extended to the machine side of FCWG for numerically investigating multiple types of MSOs of FCWG.

Finally, a generalized oscillation loop is structured based on the second-order differential operations of a studied control loop of PEC. On this basis, a generalized EFA is proposed for monitoring and analyzing of the various oscillations of PEC-penetrated power grids. Taking the control loops of the grid-side converter (GSC) of FCWG as an example, the application of the generalized oscillation loop and generalized EFA is further discussed considering the potential modal resonance

between GSC oscillations (GSOs) and external grid oscillations (EGOs) to consolidate the oscillatory stability of the PEC-penetrated power system.

Acknowledgments

Time flies, and my PhD study is nearing the end. Looking back on the life in The Hong Kong Polytechnic University, my heart is filled with gratitude.

My deepest gratitude is first to my chief supervisor, Prof. Siqi Bu, for his constant encouragement and care. I am very grateful to Prof. Siqi Bu for giving me the opportunity to study for the PhD degree in Hong Kong. My thesis is completed smoothly because of his usual and enlightening guidance. Each achievement I made is condensed with the patient help of Prof. Siqi Bu. His knowledge and personal character have deeply inspired me.

Meanwhile, I would like to thank Dr. Jianqiang Luo, Dr. Jiaxin Wen, Dr. Qian Hu, Dr. Qi Wang, Mr. Ruoheng Wang, Ms. Jiangfeng Zhang, Ms. Chaoyun Wang, Mr. Chao Huang, Ms. Xianyu Zhou, Mr. Zhaoyuan Wang, Mr. Qifan Chen, Mr. Chao Lei, Mr. Runzhuo Ma, and the other students in the research offices, for their care and help. The experience with them in the past few years is unforgettable. Also, I would like to thank my roommates and the staffs of the university's student halls, for providing me with a comfortable living environment.

Moreover, I would like to thank my dear parents for their selfless love and generous support for many years. They are the people who love me most and I owe the most. Their encouragement and dedication have been the motivation in my life. I will work harder and never fail to live up to their expectations. I wish my parents will always be healthy and happy.

Last but not least, I would like to thank the financial grant of The Hong Kong Polytechnic University to support my research work. Also, I would like to express my heartfelt thanks to all the experts who participate in the review of the thesis and the oral examination.

Table of Contents

Lists of Figures

Lists of Tables

Lists of Abbreviations

PEC	Power electronic converter
SSO/SSR	Sub-synchronous oscillation/resonance
LFO	Low-frequency oscillation
DTA	Damping torque analysis
MA	Modal analysis
SMIB	Single-machine infinite-bus
EFA	Energy flow analysis
PMU	Phasor measurement unit
WAMS	Wide area measurement system
EGO	External grid oscillation
FCWG	Full converter-based wind generation
PMSG	Permanent magnet synchronous generator
MSC	Machine-side converter
MSO	Machine-side oscillation
ARC	Auxiliary resonance controller
TDI	Time-domain implementation
FDI	Frequency-domain implementation
GSC	Grid-side converter
GSO	GSC oscillation
AVR	Automatic voltage regulator
PSS	Power system stabilizer
4M2A	4-machine 2-area
16M5A	16-machine 5-area
PLL	Phase locked loop

Chapter 1

Introduction

1.1 Background

Energy depletion and environmental problems boost the development of renewable power generations [1], among which the wind and photovoltaic power generations are the most representative. Unlike the conventional power generation, the power electronic converter (PEC) is indispensable for the integration of the renewable power generation to the power grid [2][3]. In addition, the development of new transmission technologies, such as the flexible AC transmission system and high-voltage DC system, also lead to the consequence that the conventional power equipment (e.g., synchronous generators, transmission lines, transformers, series compensation equipment) has to coexist with the large number of PECs [4][5]. The current status of the power grid with multiple emerging technologies can be illustrated by Fig. 1.1. In some optimization-related studies of the local distribution network, the external power grid is usually seen as an ideal infinite power source (e.g., the research in [6] and [7]). However, the big amount of PECs have brought complex non-linearity and dynamics to the power grid [8][9]. Thus, the external power grid can no longer be regarded as the ideal infinite power source, but the weak grid [10]. As an important aspect of power system dynamics, the stability issue has been significantly impacted [11]. The aforementioned multiple emerging technologies inevitably bring potential risks to the overall stability of power

systems, as well as the secure operation of power grids [12][13].

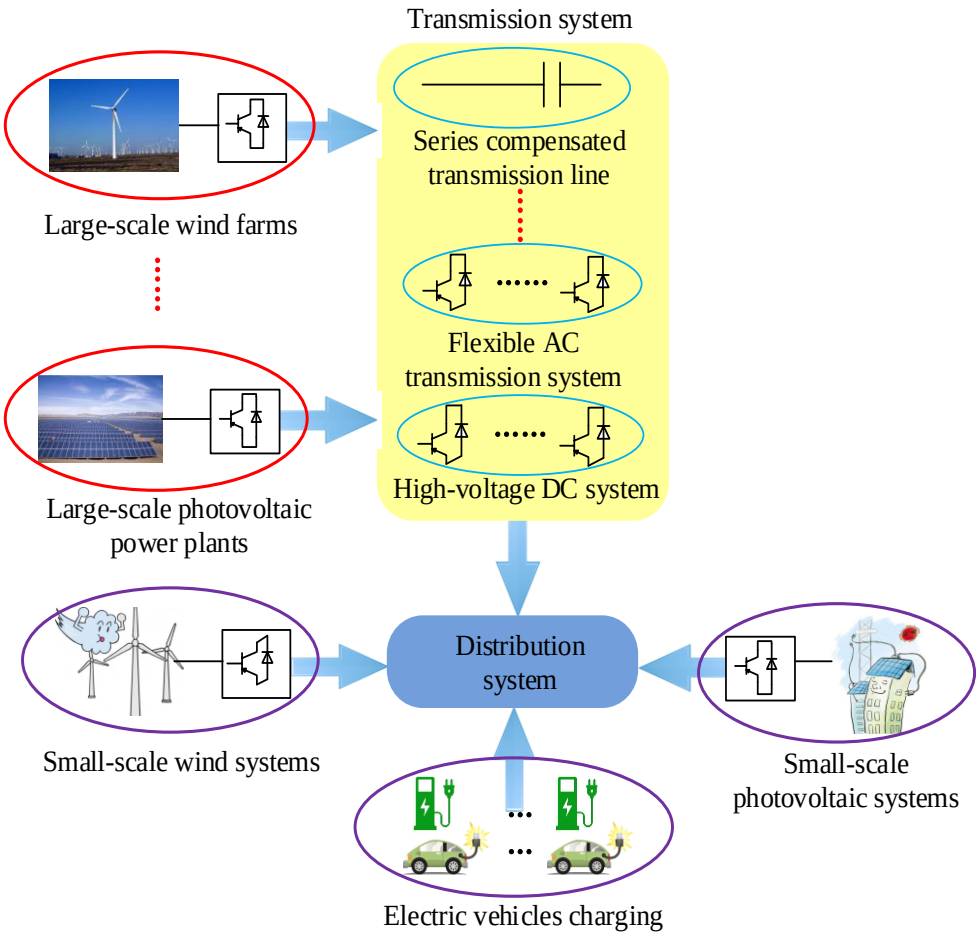

Fig. 1.1 Current status of power grids with emerging technologies.

The oscillation is an inherent phenomenon in the large-scale or interconnected system operation [14]. The oscillation events can be triggered by various factors such as the sudden change in transmission line parameters, generator faults and load fluctuations [15][16].

Since the PECs bring more complex dynamics in some frequency ranges, they have a great potential to generate various types of interactions with the external grid and bring the emerging oscillation issues [17]. On the other hand, with the number of PECs becomes huge, it is more difficult to identify which device in the system is the main source of the oscillation, which further complicates the oscillation investigation. In the

existing literature of oscillation issues, the sub-synchronous oscillation/resonance (SSO/SSR) and the low-frequency oscillation (LFO) have attracted the major attention of researchers.

An SSO/SSR incident caused by the interactions between the type-3 wind turbines and the series compensation equipment happened in Texas in 2009, which has led to the damage to system devices and motivated the research on the SSO/SSR issues caused by the power electronics [18][19]. Shortly after this accident, the authors in [20] put forward the dynamic model of the type-3 wind turbines for the SSO/SSR analysis. In recent few years, more SSO/SSR phenomena have been observed in the power systems with growing number of power electronics, such as the SSO/SSR occurring in Guyuan, Hebei Province, China in 2011 [21], and the SSO/SSR among PEC-interfaced wind generators in Hami, Xinjiang, China in 2015 [22][23]. These incidents have revealed a pressing need to investigate the emerging SSO/SSR phenomena. At present, there are some task forces in IEEE which focus on the SSO/SSR phenomena, such as the IEEE wind SSO Task Force established in 2017 [24] and the IEEE PES Task Force on Oscillation Source Location [25]. Some academic activities on SSO/SSR issues have also been organized, such as the analysis of SSO/SSR issues of the wind integration system at 2018 IEEE PES General Meeting [26]. According to the IEEE report, SSR refers to the oscillation resulting from the interactions of the turbine-generator with series compensation equipment, while SSO refers to the oscillation resulting from the interactions of the turbine-generator with quick acting control devices [27]. However, with the appearance of many new types of SSO/SSR, the conventional classification

may be no longer applicable. The authors in [28] make the attempts to refine the classification of SSO/SSR based on the oscillation modes. Specifically, the SSO/SSR is divided into three types according to [28]: (1) SSO/SSR caused by the torsional vibration of rotating machines; (2) SSO/SSR caused by the electric resonance between the capacitance and the inductance in the power grid, especially the reactive power compensation and filtering devices; and (3) SSO/SSR caused by the interactions of the various PECs with the external grid or other PECs. Ref. [29] reveals some characteristics of the SSO/SSR caused by the type-3 and type-4 wind farms through analyzing the real-life measurement data.

LFO initially originates from the small-signal stability issues of synchronous generators in power grids, which is more common and conventional. Over the past years, more LFO events have occurred in power grids all over the world: for example, the LFO phenomena have been observed at different frequencies in Texas [30]; [31] reports that one LFO incident happened in the south power grid of China in 2005; [32] presents the LFO observation at 0.38 Hz in 2013 summer in the US. These incidents have also aroused the interest of some researchers. In recent years, there have been some studies on LFO, such as the research in [33]-[35]. Typically, the LFO can be classified into two types: the intra-area LFO and the inter-area LFO [36], and the latter is of more general concerns. The growing number of LFO incidents have set a high requirement for the accuracy of the identification of LFO characteristics [37]. However, with the increasing number of PECs being connected to the power grid, the LFO modes show more complexities, such as the LFO induced by the variation of the wind power in [38], and

the LFO existing in the train-traction network in [39] and [40]. Generally, the LFO and SSO/SSR have different frequency ranges of interests. The LFO can occur at the very low frequency, even as low as 0.1 Hz [41], while the frequency range of the SSO/SSR is normally higher than that of the LFO.

1.2 Literature Review

As the statement in Section 1.1, the emerging oscillation problems seriously threaten the safe and stable operation of power grids. Therefore, the various oscillations need to be investigated in the PEC-penetrated power system. In the existing literature, the stability problem caused by the oscillation in power systems is usually known as the oscillatory stability [42]-[46]. In this thesis, the oscillatory stability is adopted as the academic terminology.

After an oscillation accident occurs, if the oscillating power lasts for a while and then gradually decays, the oscillation is considered to be stable [47]. The investigation of an oscillation involves two aspects, i.e., its frequency and damping performance. The frequency of an oscillation can reflect its type and potential causes. The damping performance of an oscillation characterizes its decaying rate, which is a quantitative characterization to evaluate the oscillatory stability, and the better damping performance indicates a shorter oscillation duration. For the power systems with weak natural damping, the damping performance is normally enhanced by using the external equipment [48]-[51], and the damping performance should be carefully investigated for the installation planning and parameter setting.

At present, there are two commonly-used modeling-based methods for the damping performance assessment, i.e., the damping torque analysis (DTA) and modal analysis (MA).

DTA originates from the concept of the electric torque of synchronous generators in the electromechanical oscillation. The generator rotor movement produces the torque effect, which provides a clear physical explanation [52]. As a component of the electric torque, the damping torque contributes to the damping of power oscillations [52]. At present, DTA is a common method to examine the effect of excitation control on the power system small-signal stability and gradually extended to the damping performance assessment as well as the design of stabilizer controllers. DTA relies on the mathematical model of the components [53]. The mathematical models of the doubly-fed induction generator, fixed-speed induction generator and three transitional wound rotor generators are established in [54] to realize the damping torque assessment. A model reduction strategy of doubly-fed induction generators is mathematically proposed in [55] to improve the efficiency of dynamic DTA. The dynamic mathematical model of doubly-fed induction generators with least orders but acceptable accuracy is established in [56] to investigate the damping torque from different dynamic components of doubly-fed induction generators. DTA is proved to be equivalent to the conventional eigenvalue analysis [57]. The damping torque coefficient is an important index to represent the relationship between the damping torque and angular frequency. Ref. [58]-[60] study the damping torque coefficient through the mathematical modeling based on a linearized model. In a single-machine infinite-bus (SMIB) power system,

there is only one dominant oscillation mode and the damping torque coefficient can directly characterize the damping performance of the whole power system. However, the damping torque coefficients of multiple generators are presented in the matrix form for multi-machine power systems [52]. The damping contribution of the whole power system is distributed to the generators associated with the oscillation mode, which makes the analysis more complex for multi-machine power systems. Therefore, there is a lack of a useful concept for DTA that can characterize the integration effect of the damping contribution from the whole power system, which should be applicable for arbitrary types of synchronous generator models in multi-machine power systems.

The modal analysis (MA) is another commonly-used modeling-based method to examine the oscillations [61][62]. MA usually requires the mathematical modeling of the whole power system. The state-space modeling is widely adopted in MA, and the advantage is that it can handle the nonlinear system modeling for the oscillatory stability analysis. Refs. [63]-[67] adopt the state-space modeling approach to build the state-space matrix and use the eigenvalues of the state-space matrix to assess the oscillatory stability in power systems with the wind power integration, photovoltaic power integration and new transmission technologies. Generally, MA focuses on the oscillation modes or corresponding eigenvalues without paying much attention to the physical mechanism of oscillations [68]. The eigenvalue is a fundamental and conventional index for the studies of the oscillatory stability in the power grid [69][70]. The imaginary part of the eigenvalue represents the angular frequency of the oscillation, and the real part of the eigenvalue can accurately indicate the relevant damping of the

oscillation [71]. Some recent work of MA is summarized as follows. The modal sensitivity is derived as a new index in [72] to represent the impact of dynamic interactions introduced by double-fed induction generators on the electromechanical oscillations. The authors in [73] propose a modal superposition theory to classify the modal interactions between wind power oscillations and electromechanical oscillations. MA and DTA are the well-developed methods, but they have the certain difficulties when applied in the large-scale power systems. Firstly, the large number of system components leads to a high-dimension modeling [74], which has significantly raised the modeling difficulty as well as the computational burden of computers and affected the efficiency of oscillatory stability studies [75][76]. In addition, the components of modern power grids are becoming increasingly diversified and time-varying, which makes it difficult to obtain the accurate model and parameters of each component.

In view of the above restrictions of DTA and MA, it is urgent to develop an alternative method to investigate the oscillations, which does not largely reply on the precise and high-dimensional modeling. Apart from the modeling-based method, the measurement-based method is an emerging way to assess the stability of modern power systems [77][78].

The oscillation events are accompanied by the transmission and dissipation of the oscillatory energy flow in the power network [79]. For a stable oscillation event, the oscillatory energy flow is eventually dissipated by the generators as well as external stabilizers if any. Based on this fact, the energy flow analysis (EFA) is developed and able to provide a clear explanation on the physical mechanism of the electromechanical

oscillation. Hence, the EFA provides a clear description for the oscillation mechanism. In recent years, the phasor measurement unit (PMU) and wide area measurement system (WAMS) have been applied in the stability analysis of the power system [80][81], which facilitates the measurement of the oscillatory energy flow at the terminal of a local power generation and thus enabled a convenient EFA [82]. Therefore, the measurement-based EFA gradually becomes popular to the oscillatory stability analysis. Compared with DTA and MA, EFA is a type of method that mainly replies on the measurement technology and shows apparent advantages: no complex high-dimensional modeling process is required, especially for the large-scale power system. The merits have attracted quite a few research efforts in developing EFA for the studies of the oscillatory stability. The basic components of the oscillatory energy flow are presented in [83] and the oscillatory energy flow is utilized to determine the location of oscillation sources. The calculation of the oscillatory energy flow on the bus level is given in [84], and then the oscillation source is determined according to the variation tendency of the oscillatory energy flow at each generator. On the basis of [84], the authors in [85] propose a scheme of the cut-set energy construction to make full use of the measurement data. The authors in [86] divide the whole system into closed-contour regions to locate the oscillation source on the region level considering the incomplete measurement coverage. A two-level method is proposed in [87] for locating the oscillation source from both the bus level and the control device level. The above-mentioned work on the source location is a typical application of EFA, but the investigation of the damping performance of oscillations is not included.

Thus, in order to make EFA more capable and valid, the researchers apply EFA to conduct the numerical analysis for the oscillatory stability. Some of the latest work are summarized as follows. The components of the oscillatory energy flow are analyzed with more details in [88], which lays a foundation for the EFA-based numerical analysis for oscillations. In order to quantitatively characterize the change of damping contributions, the damping loss factor of the generator is defined and derived in [89] and [90]. However, the limitation of [89] and [90] is that the feasibility analysis of the defined concept is limited to the specified generator model. The dissipation of the oscillatory energy flow is revealed to be connected with the damping torque of generators in [91]-[93] to offer a capability of the qualitative analysis for the oscillatory stability. The EFA-based work is further extended to the SSO/SSR with higher frequencies in [94]. However, the limitation of [91]-[94] is that the dissipation of the oscillatory energy flow is not further linked with the damping ratio (or eigenvalue) in the multi-machine power system, which has restricted their capability in the quantitative analysis. The rate of change of the dissipation of the oscillatory energy flow is recommended in [95] and [96] to assess the damping performance of an electromechanical oscillation. However, the proposed method in [95] employs a linear fitting for the dissipation of the oscillatory energy flow, which may be inaccurate under some operating conditions. The proposed method in [96] relies on the availability of parameters of the power network, which is not quite a generalized approach. The connection between EFA and MA as well as DTA is attempted to be revealed in [97]-[100]. However, the strict proof is provided for the SMIB power system based on the

certain model and parameters of the synchronous generator, which lacks a complete validation for arbitrary models of synchronous generators. For the multi-machine power system, the validation is obtained from the repeated simulations and curve-fittings in [97], and the strict theoretical proof is not provided.

Therefore, there is no research seen so far to rigorously justify the consistency between EFA and MA as well as DTA for the damping performance assessment. In addition, the measurement at the terminal of a local generator involves multiple oscillation modes with respect to different frequencies in the multi-machine power system. Thus, the pre-processing of the measurements at the terminal of a local generator should be conducted so that the damping contribution with respect to the interested frequency can be screened. Considering the above discussion, the EFA-based numerical analysis for the oscillatory stability should be further improved. Specifically, there is a pressing need to rigorously prove the consistency between EFA and MA as well as DTA for investigating the oscillations especially in multi-machine power systems, and the expected conclusions should be applicable for the arbitrary models and parameters of synchronous generators, as well as arbitrary topologies and parameters of power networks.

As described in Section 1.1, the large number of PECs have brought the emerging oscillation issues to the conventional power system. With the growing number of PECs integrated into the power grid, the PECs have become an obvious source of complex dynamics. Moreover, the emerging oscillation of PECs may even have the potential resonance with the external grid oscillation (EGO), which can increase the harm of

oscillation accidents. The instability of the PEC-penetrated power grid has been frequently reported and drawn increasing attention recently from both academia and industry [101]-[105]. The quantitative investigation of the damping and frequency feature of various oscillations becomes particularly important in PEC-penetrated power grids [106]. However, the above-mentioned EFA research does not involve the PECs, which reduces the popularity and timeliness of the work. That is to say, the EFA-based quantitative analysis is still limited to the oscillatory stability studies of the synchronous generator-dominated power grid and needs to be generalized to that of the PEC-dominated power system.

Among the different kinds of renewable generations, the wind power is a predominant and typical one [107]. Like the conventional power generation, the stable operation of the wind generation is of critical importance to the reliable power supply to the external power grid [108]. The full converter-based wind generation (FCWG) is a preferable option for the wind power integration [109]. Compared with the doubly fed induction generator-based wind power generation, FCWG has a very different nature in dynamics. The permanent magnet synchronous generator (PMSG) and machine-side converter (MSC) of FCWG are decoupled by the DC-link from the external power grid and become relatively independent [110][111]. However, the intermittence and fluctuation of the wind speed can trigger the inherent machine-side oscillation (MSO) of FCWG. The improper parameter settings of controllers can lead to the poor damping performance of MSO [112]. The poorly damped MSO can have a severe impact on the wind power supply to the external power grid. On the other hand,

the dynamics in the rotor of PMSG can be effectively utilized to mitigate the modal resonance between the FCWG system and weak grid and hence improve the oscillatory stability by equipping with an auxiliary resonance controller (ARC) on the machine side of FCWG [113]. However, the utilization of ARC can unfortunately introduce the EGO to the originally dynamics-decoupled machine side of FCWG, and even cause the modal resonance with the inherent MSO of FCWG, which would dramatically complicate and aggravate the machine-side dynamics of FCWG.

Based on the facts above, investigating the damping feature of multiple MSOs of FCWG becomes more important. Specifically, investigating the characteristics of MSOs of FCWG can help wind farm operators understand the condition of wind generation units to provide the reliable wind power supply and improve the oscillatory stability of the PEC-penetrated power grid, which is helpful to further increase the penetration of FCWG in the modern power systems. However, the MSO issue of FCWG is often ignored by researchers. Thus, the machine-side dynamics of FCWG with/without ARC should be comprehensively and quantitatively studied. It should be noted that the MSOs mentioned in this thesis not only refer to the inherent MSOs of FCWG, but also the EGOs introduced by ARC (i.e., the non-inherent MSOs of FCWG). When ARC introduces the dynamics of the external grid to the MSC controls, the machine-side dynamics of FCWG are no longer independent. Thus, the calculation of relevant eigenvalues requires the dynamic modelling of the whole power systems. In practice, it is difficult for wind farm operators to obtain the detailed models and accurate parameters of all components in the external power systems. Even if the information of

the full system model is available, the modelling and computational complexity can be significantly raised for the oscillatory stability studies especially considering the large-scale power system [114]. Hence, the above-mentioned points limit the application of the mathematical modeling-based methods, and the EFA of conventional synchronous generators urgently needs to be extended to PMSG to investigate MSOs of FCWG.

1.3 Primary Contributions

Considering all the points in Section 1.2, the primary contributions of this thesis are listed as follows.

(1) The connection between DTA and EFA for qualitatively evaluating the damping performance of electromechanical oscillations of multi-machine power systems is revealed.

For DTA, in order to characterize the integration effect of the damping contribution from the whole power system, a concept of the aggregated damping torque coefficient is proposed and derived. It can be applied to arbitrary types of synchronous generator models in multi-machine power systems. The aggregated damping torque coefficient lays a foundation for identifying the theoretical connection between DTA and EFA.

For EFA, the pre-processing of measurements at the terminal of a local generator is conducted in the time domain. Based on that, a concept of the frequency-decomposed energy attenuation coefficient is newly defined to pick out the damping contribution with respect to the interested frequency. Then, the connection between DTA and EFA is strictly proven and the consistency of the aggregated damping torque coefficient and

frequency-decomposed energy attenuation coefficient is revealed for the first time, which is a general conclusion for arbitrary types of synchronous generator models in both SMIB power system and multi-machine power system.

(2) A novel EFA is proposed based on the signal reconstruction and decomposition, which can be implemented in two forms, i.e., the time-domain implementation (TDI) and frequency-domain implementation (FDI). Compared with the research in (1), the proposed EFA is strictly proved to be consistent with MA especially for the multi-machine power systems, and the proof stays valid for arbitrary models of synchronous generators as well as arbitrary types of power networks.

For TDI of the proposed EFA, the measurements at the terminal of a local generator are reconstructed and then decomposed in the time domain based on the principle of the Laplace analysis. After that, the mode-screened damping torque coefficient is defined to extract the damping torque coefficient with respect to an electromechanical oscillation mode from the perspective of a local generator. Then, FDI is derived to transform the proposed EFA from the time domain to frequency domain using the Parseval's Theorem. The mode-screened damping torque coefficient with respect to the interested oscillation mode from the perspective of FDI is consistent with that from TDI.

Then, the connection between the proposed EFA and MA in quantitatively investigating the electromechanical oscillations is strictly proved in the multi-machine power system for the first time. The proof is effective for arbitrary models of synchronous generators as well as arbitrary types and parameters of power networks. Moreover, the application procedure of the proposed EFA for quantitatively estimating

the damping performance with respect to an electromechanical oscillation mode is given.

(3) The proposed EFA in (2) is applied to quantitatively investigate the inherent and non-inherent MSOs of FCWG (including the potential modal resonance among them) for the first time.

Specifically, the proposed EFA in (2) is extended to the machine side of FCWG in the time domain to extract the damping feature of interested MSOs of FCWG without any modelling requirement. Then, the consistency between the extended EFA and MA when studying MSOs of FCWG is proved and revealed, which is general for the arbitrary control schemes of FCWG in the multi-machine environment. With the help of the extended EFA, the damping feature of multiple types of MSOs in different scenarios is quantitatively assessed for the first time.

(4) The proposed EFA in (2) is further applied to quantitatively investigate the various oscillations of the PEC-penetrated power system (including the potential modal resonance among them) for the first time.

Specifically, the generalized oscillation loop is structured based on the second-order differential operations in the studied control loop of the PEC. On this basis, the generalized EFA is proposed for monitoring and analyzing the various oscillations of the PEC-penetrated power system. In other words, the proposed EFA in (2) is generalized to any control loop of the PEC with the second-order differential operations. Taking the grid-side converter (GSC) of FCWG as the example, the application of the generalized oscillation loop and generalized EFA are further demonstrated and

discussed for quantitatively investigating the GSC oscillation (GSO), which provides the reference for the parameter setting and adjustment of GSC.

1.4 Thesis Layout

The rest of this thesis consists of five chapters, which is summarized as follows.

Chapter 2 studies the connection between DTA and EFA for qualitatively evaluating the damping performance of electromechanical oscillations of multi-machine power systems. Specifically, a DTA in the frequency domain is presented and the aggregated damping torque coefficient is defined. Then, EFA is conducted based on the pre-processing of measurements in the time domain and the frequency-decomposed energy attenuation coefficient is defined. The frequency spectrum analysis of the energy attenuation coefficient is conducted, which reveals the consistency between DTA and EFA.

In Chapter 3, a novel EFA is proposed in multi-machine power systems and its connection with MA is proved for quantitatively investigating the electromechanical oscillations. Specifically, TDI of the proposed EFA is developed, and FDI of the proposed EFA is conducted equivalently in the multi-machine power system. Then, the connection between the proposed EFA and MA is strictly proved, and the application procedure of the proposed EFA is given.

In Chapter 4, the proposed EFA in Chapter 3 is extended and applied for quantitatively investigating the MSOs of FCWG systems. Specifically, the main configuration and machine-side control loops of FCWG are briefly introduced. Then,

the proposed EFA in Chapter 3 is extended to the machine side of FCWG in the time domain, and the consistency between the extended EFA and MA is strictly revealed for MSOs of FCWG in the frequency domain.

In Chapter 5, the generalized oscillation loop is structured in the control loop of the PEC, and then the proposed EFA in Chapter 3 is further generalized to quantitatively investigate the various oscillations of the PEC-penetrated power system. Then, the generalized oscillation loop and generalized EFA are further derived and tested in the control loops of GSC of FCWG for GSOs considering the potential resonance.

Finally, the conclusions and future work of the thesis are summarized and drawn in Chapter 6.

Chapter 2

The Connection between Damping Torque Analysis and Energy Flow Analysis in Evaluating Damping Performance of Electromechanical Oscillations

2.1 Overview

The damping performance assessment of electromechanical oscillations of power systems is crucial for the stable operation of power grids. In this chapter, the connection between a modeling-based method (i.e., DTA) and a measurement-based method (i.e., EFA) are systematically examined and revealed for the better understanding of the oscillatory damping mechanism. Firstly, a concept of the aggregated damping torque coefficient is proposed and derived based on DTA of multi-machine power systems, which can characterize the integration effect of the damping contribution from the whole power system. Then, the pre-processing of measurements at the terminal of a local generator is conducted for EFA, and a concept of the frequency-decomposed energy attenuation coefficient is defined to characterize the damping contribution with respect to the frequency of interest. On this basis, the frequency spectrum analysis of the energy attenuation coefficient is employed to rigorously prove that the results of DTA and EFA are essentially equivalent, which is valid for arbitrary types of synchronous generator models in multi-machine power systems. Additionally, the consistency between the aggregated damping torque coefficient and frequency-

decomposed energy attenuation coefficient is further verified by the numerical calculation in case studies. The relation between the proposed coefficients and the eigenvalue (or damping ratio) is finally revealed, which consolidates the application of the proposed concepts in the qualitative assessment of the damping performance.

2.2 Damping Torque Analysis in Frequency Domain

In this section, a DTA is conducted in the frequency domain via the mathematical modeling. Compared with the Phillips-Heffron model-based analysis in [52], the derivations presented in this section are order-independent for the synchronous generator models and can effectively evaluate the integration effect of the damping contribution from multi-machine power systems.

The swing equation of the *i*-th generator in a power system is expressed by

$$\begin{cases} \dfrac{\mathrm{d}\delta_i(t)}{\mathrm{d}t} = \omega_0\left(\omega_i(t)-1\right) \\ \dfrac{\mathrm{d}\omega_i(t)}{\mathrm{d}t} = \dfrac{1}{T_{J,i}}\left(P_{m,i}(t)-P_{e,i}(t)-D_i\left(\omega_i(t)-1\right)\right) \end{cases} \tag{2.1}$$

where t is the time variable; $\delta_i(t)$ denotes the power angle of the i-th generator; $\omega_i(t)$ denotes the angular frequency of the i-th generator; ω_0 denotes the synchronous angular frequency; $P_{e,i}(t)$ denotes the electric power of the i-th generator; $P_{m,i}(t)$ denotes the mechanical power of the i-th generator; D_i denotes the natural damping of the i-th generator; $T_{J,i}$ denotes the inertia constant of the i-th generator; and $\mathrm{d}(\cdot)$ is the differential operator. It is noted that i can be omitted for an SMIB power system.

For DTA, some other equations should be further involved besides (2.1), e.g., the

equations that characterize automatic voltage regulators (AVRs), power system stabilizers (PSSs), etc. Define a vector $\boldsymbol{Z}(t)$ that includes the state variables of the generator(s) except $\delta_i(t)$ and $\omega_i(t)$. The dimension of $\boldsymbol{Z}(t)$ is $(\sum_{i=1}^{k} n_i - 2)\times 1$, where n_i is the order of the i-th generator model and k is the number of the generator(s). Then, the linearized model of a power system can be derived as

$$\begin{bmatrix} \dfrac{\mathrm{d}\Delta\delta_i(t)}{\mathrm{d}t} \\ \dfrac{\mathrm{d}\Delta\omega_i(t)}{\mathrm{d}t} \\ \dfrac{\mathrm{d}\Delta\boldsymbol{Z}(t)}{\mathrm{d}t} \end{bmatrix} = \begin{bmatrix} 0 & \omega_0 & \mathbf{0} \\ A_{21} & -\dfrac{D_i}{T_{J,i}} & \boldsymbol{A}_{23} \\ \boldsymbol{A}_{31} & \boldsymbol{A}_{32} & \boldsymbol{A}_{33} \end{bmatrix} \begin{bmatrix} \Delta\delta_i(t) \\ \Delta\omega_i(t) \\ \Delta\boldsymbol{Z}(t) \end{bmatrix} \tag{2.2}$$

where A_{21}, $\boldsymbol{A}_{23}$, $\boldsymbol{A}_{31}$, $\boldsymbol{A}_{32}$ and $\boldsymbol{A}_{33}$ are the block sub-matrices of the state matrix; $\Delta\delta_i(t)$ denotes the power angle deviation of the i-th generator; $\Delta\omega_i(t)$ denotes the angular frequency deviation of the i-th generator; $\Delta\boldsymbol{Z}(t)$ denotes the deviation of the state variables aggregated in $\boldsymbol{Z}(t)$; and $\mathbf{0}$ represents the $1\times(\sum_{i=1}^{k} n_i - 2)$ vector in which the elements are all 0. It is noted that the dimensions of $\boldsymbol{A}_{23}$, $\boldsymbol{A}_{31}$, $\boldsymbol{A}_{32}$ and $\boldsymbol{A}_{33}$ are $1\times(\sum_{i=1}^{k} n_i - 2)$, $(\sum_{i=1}^{k} n_i - 2)\times 1$, $(\sum_{i=1}^{k} n_i - 2)\times 1$ and $(\sum_{i=1}^{k} n_i - 2)\times(\sum_{i=1}^{k} n_i - 2)$, respectively.

The representation of (2.2) is transformed from the time domain to frequency domain through the Fourier analysis, as given by (2.3).

$$\begin{bmatrix} \mathrm{j}2\pi f\Delta\delta_i(f) \\ \mathrm{j}2\pi f\Delta\omega_i(f) \\ \mathrm{j}2\pi f\Delta\boldsymbol{Z}(f) \end{bmatrix} = \begin{bmatrix} 0 & \omega_0 & \mathbf{0} \\ A_{21} & -\dfrac{D_i}{T_{J,i}} & \boldsymbol{A}_{23} \\ \boldsymbol{A}_{31} & \boldsymbol{A}_{32} & \boldsymbol{A}_{33} \end{bmatrix} \begin{bmatrix} \Delta\delta_i(f) \\ \Delta\omega_i(f) \\ \Delta\boldsymbol{Z}(f) \end{bmatrix} \tag{2.3}$$

where f is the frequency variable; $\Delta\delta_i(f)$, $\Delta\omega_i(f)$ and $\Delta\boldsymbol{Z}(f)$ denote the frequency-domain

forms of $\Delta\delta_i(t)$, $\Delta\omega_i(t)$ and $\Delta\boldsymbol{Z}(t)$ under the Fourier analysis, respectively.

Based on (2.1) and (2.3), the linearized representation of a multi-machine power system can be derived as the form in Fig. 2.1 under the Fourier analysis.

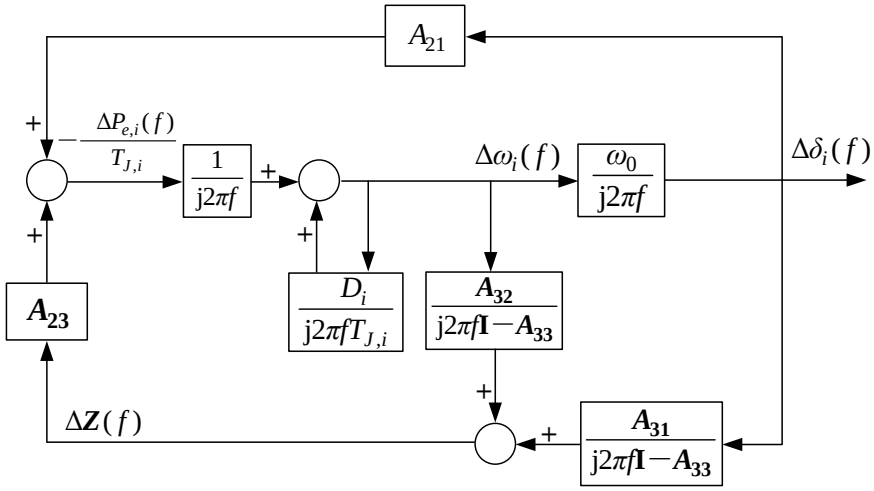

Fig. 2.1. Linearized model of a multi-machine power system under the Fourier analysis.

From Fig. 2.1, the relationships among the major variables are clearly revealed. Then, (2.4)-(2.6) can be derived, respectively.

$$\Delta P_{e,i}(f) = -T_{J,i}\left(A_{21}\Delta\delta_i(f) + \boldsymbol{A_{23}}\Delta\boldsymbol{Z}(f)\right) \tag{2.4}$$

$$\Delta\delta_i(f) = \frac{\omega_0}{\mathrm{j}2\pi f}\Delta\omega_i(f) \tag{2.5}$$

$$\Delta\boldsymbol{Z}(f) = \frac{\boldsymbol{A_{31}}}{\mathrm{j}2\pi f\mathbf{I} - \boldsymbol{A_{33}}}\Delta\delta_i(f) + \frac{\boldsymbol{A_{32}}}{\mathrm{j}2\pi f\mathbf{I} - \boldsymbol{A_{33}}}\Delta\omega_i(f) \tag{2.6}$$

where $\mathbf{I}$ is the $(\sum_{i=1}^{k} n_i - 2)\times(\sum_{i=1}^{k} n_i - 2)$ identity matrix and $\Delta P_{ei}(f)$ is the electric power deviation of the i-th generator in the frequency domain.

Substitute (2.5) and (2.6) into (2.4), and (2.7) can be derived step by step.

$$\begin{aligned}
\Delta P_{e,i}(f) &= -T_{J,i}\left(A_{21}\Delta\delta_i(f) + \boldsymbol{A}_{23}\Delta\boldsymbol{Z}(f)\right) \\
&= -T_{J,i}\left(\left(A_{21} + \boldsymbol{A}_{23}\frac{\boldsymbol{A}_{31}}{\mathrm{j}2\pi f\mathbf{I} - \boldsymbol{A}_{33}}\right)\Delta\delta_i(f) + \left(\boldsymbol{A}_{23}\frac{\boldsymbol{A}_{32}}{\mathrm{j}2\pi f\mathbf{I} - \boldsymbol{A}_{33}}\right)\Delta\omega_i(f)\right) \\
&= -T_{J,i}\left(\left(A_{21} + \boldsymbol{A}_{23}\frac{\boldsymbol{A}_{31}}{\mathrm{j}2\pi f\mathbf{I} - \boldsymbol{A}_{33}}\right)\frac{\omega_0}{\mathrm{j}2\pi f} + \left(\boldsymbol{A}_{23}\frac{\boldsymbol{A}_{32}}{\mathrm{j}2\pi f\mathbf{I} - \boldsymbol{A}_{33}}\right)\right)\Delta\omega_i(f)
\end{aligned} \tag{2.7}$$

The electric torque consists of two components: the damping torque and synchronizing torque. According to the discussion in Chapter 1, the damping torque contributes to the damping of power oscillations. The electric power is considered to be approximately equal to the electric torque. According to the definition of the damping torque, the real part of the ratio of $\Delta P_{e,i}(f)$ and $\Delta\omega_i(f)$, i.e. $K_{da,i}(f)$ in (2.8) can be regarded as the damping torque coefficient. Eq. (2.7) and (2.8) will play an important role in revealing the connection between DTA and EFA in Section 2.4.

$$K_{da,i}(f) = \mathrm{Re}\left(-T_{J,i}\left(\left(A_{21} + \boldsymbol{A}_{23}\frac{\boldsymbol{A}_{31}}{\mathrm{j}2\pi f\mathbf{I} - \boldsymbol{A}_{33}}\right)\frac{\omega_0}{\mathrm{j}2\pi f} + \left(\boldsymbol{A}_{23}\frac{\boldsymbol{A}_{32}}{\mathrm{j}2\pi f\mathbf{I} - \boldsymbol{A}_{33}}\right)\right)\right) \tag{2.8}$$

where Re(·) is the real part operator.

For an SMIB power system, (2.8) is actually the damping torque coefficient of this single generator according to the conventional definition of the damping torque.

For a multi-machine power system, the damping torque coefficients of multiple generators are usually presented in the matrix form. Eq. (2.8) essentially implies the integration effect of the damping contribution from the whole power system but projected to the *i*-th generator, which is different from the conventional definition of the damping torque. Hence, a useful concept is given as **Definition 2.1**.

Definition 2.1. *The aggregated damping torque coefficient of the i-th generator with respect to the interested oscillation frequency f_d is defined as $K_{da,i}(f_d)$ by*

substituting f_d into (2.8).

The physical explanation of this concept is that all the damping contribution from the whole power system is aggregated and then reflected from a selected generator.

2.3 Energy Flow Analysis in Time Domain

As indicated in [98] and [99], the oscillatory energy flow from node *a* to node *b* can be calculated by

$$\begin{aligned} W_{ab} &= \int \left(P_{ab} \mathrm{d}\theta_a + Q_{ab} \mathrm{d}\left(\ln U_a \right) \right) \\ &= \int \left(P_{ab,s} + \Delta P_{ab} \right) \mathrm{d}\left(\theta_{a,s} + \Delta \theta_a \right) + \int \left(Q_{ab,s} + \Delta Q_{ab} \right) \mathrm{d}\left(\ln(U_{a,s} + \Delta U_a) \right) \\ &= \int P_{ab,s} \mathrm{d}\Delta\theta_a + \int \Delta P_{ab} \mathrm{d}\Delta\theta_a + \int \left(Q_{ab,s} + \Delta Q_{ab} \right) \mathrm{d}\left(\ln(U_{a,s} + \Delta U_a) \right) \end{aligned} \tag{2.9}$$

where W_{ab} is the oscillatory energy flow from node *a* to node *b*; P_{ab} is the active power flow from node *a* to node *b*; Q_{ab} is the reactive power flow from node *a* to node *b*; U_a and θ_a are the amplitude and phase angle of the voltage of node *a*; the subscript $(\cdot)_s$ in (2.9) denotes the steady-state value of the corresponding variable; and the operator $\Delta(\cdot)$ in (2.9) denotes the deviation of the corresponding variable from its steady-state value.

Normally, the reactive power in (2.9) is ignored. Then, it is seen that the oscillatory energy flow in (2.9) consists of two components, as listed in (2.10).

$$\begin{cases} W_{ab}^1 = \int P_{ab,s} \mathrm{d}\Delta\theta_a \\ W_{ab}^2 = \int \Delta P_{ab} \mathrm{d}\Delta\theta_a \end{cases} \tag{2.10}$$

where W_{ab}^1 is the oscillatory energy component with respect to $P_{ab,s}$; and W_{ab}^2 is the oscillatory energy component with respect to ΔP_{ab}. W_{ab}^2 reflects the dissipation of the oscillatory energy flow [98].

The electric power of the generator is considered to be numerically equal to the active power flow between the two nodes, and the phase angle of the node voltage is approximately regarded as the power angle of the generator. On this basis, the dissipation of the oscillatory energy flow of the *i*-th generator can be calculated by (2.11) using the measurements at the terminal of a local generator.

$$W_{d,i} = \int \Delta P_{e,i}(t) \mathrm{d}\Delta\delta_i(t) \tag{2.11}$$

where $W_{d,i}$ is the dissipation of the oscillatory energy flow of the *i*-th generator; and $\Delta P_{e,i}(t)$ is the electric power deviation of the *i*-th generator.

The electric power is considered to be approximately equal to the electric torque. Then, the dissipation of the oscillatory energy flow of the *i*-th generator can also be represented as

$$W_{d,i} = \omega_0 \int \Delta T_{e,i}(t) \Delta\omega_i(t) \mathrm{d}t \tag{2.12}$$

where $\Delta T_{e,i}(t)$ is the electric torque deviation of the *i*-th generator.

Generally, the electric torque can be divided into synchronizing torque and damping torque [52], i.e., (2.13).

$$\Delta T_{e,i}(t) = K_{d,i}\Delta\omega_i(t) + K_{s,i}\Delta\delta_i(t) \tag{2.13}$$

where $K_{d,i}$ is the damping torque coefficient of the *i*-th generator; and $K_{s,i}$ is the synchronizing torque coefficient of the *i*-th generator.

The integral of the product of power angle deviation and angular frequency deviation is equal to zero, and then (2.14) can be further derived based on (2.11)-(2.13).

$$\int \Delta P_{e,i}(t) \mathrm{d}\Delta\delta_i(t) = \omega_0 \int K_{d,i} \Delta\omega_i^{\,2}(t) \mathrm{d}t \tag{2.14}$$

The damping torque coefficient can be derived from (2.14), as given by

$$K_{d,i} = \frac{\int_0^{+\infty} \Delta P_{e,i}(t) \mathrm{d}\Delta\delta_i(t)}{\omega_0 \int_0^{+\infty} \left(\Delta\omega_i(t)\right)^2 \mathrm{d}t} \tag{2.15}$$

$K_{d,i}$ can reflect the energy attenuation brought by the damping torque of the generator, and hence we define the calculation result of (2.15) as the energy attenuation coefficient $K_{de,i}$ in this chapter. Using the measurements at the terminal of a local generator, the energy attenuation coefficient of the i-th generator can be estimated by

$$K_{de,i} = \frac{\int_0^{+\infty} \Delta P_{e,i}(t) \Delta\omega_i(t) \mathrm{d}t}{\int_0^{+\infty} \left(\Delta\omega_i(t)\right)^2 \mathrm{d}t} \tag{2.16}$$

where $K_{de,i}$ is the energy attenuation coefficient of the i-th generator based on EFA.

For an SMIB power system, the measurement at the terminal of the generator involves only one oscillation mode. Eq. (2.16) can be directly used to estimate the energy attenuation coefficient of this single generator.

For a multi-machine power system, the measurement at the terminal of a local generator involves multiple oscillation modes. It is difficult to directly estimate the energy attenuation coefficient using (2.16). Therefore, it is necessary to conduct the pre-processing for the measurements at the terminal of a local generator in the time domain. According to the Fourier analysis, the signal that satisfies the Dirichlet condition can be decomposed into a series of sub-signals, as given by

$$g(t) = \sum_{j=0}^{p} A_j \cos(2\pi f_j t + \alpha_j) \tag{2.17}$$

where $g(t)$ denotes a signal in the time domain; p is the number of sub-signals

decomposed from $g(t)$; A_j denotes the amplitude of the j-th sub-signal; f_j denotes the frequency of the j-th sub-signal; and α_j denotes the phase angle of the j-th sub-signal.

The amplitude-frequency characteristic and phase-frequency characteristic of $g(t)$ can be obtained by (2.18)-(2.20).

$$G(f)=\int_{-\infty}^{+\infty} g(t)e^{-\mathrm{j}2\pi ft}\mathrm{d}t \tag{2.18}$$

$$\boldsymbol{A}_{1\times p}=\left|G(f)\right| \tag{2.19}$$

$$\boldsymbol{\alpha}_{1\times p}=\arg\left(G(f)\right) \tag{2.20}$$

where $G(f)$ is the frequency-domain form of $g(t)$ under the Fourier analysis; $|\cdot|$ denotes the magnitude of a complex number; $\arg(\cdot)$ denotes the phase angle of a complex number; $\boldsymbol{A}_{1\times p}$ denotes the p-dimensional vector that includes the amplitudes of sub-signals at each frequency; and $\boldsymbol{\alpha}_{1\times p}$ denotes the p-dimensional vector that includes the phase angles of sub-signals at each frequency.

The amplitude A_d ($A_d \in \boldsymbol{A}_{1\times p}$) and phase angle α_d ($\alpha_d \in \boldsymbol{\alpha}_{1\times p}$) at the interested frequency f_d can be observed from the amplitude-frequency characteristic and phase-frequency characteristic of $g(t)$, and then the decomposed sub-signal with respect to the interested frequency f_d is given as

$$g^{f_d}(t)=A_d\cos(2\pi f_d t+\alpha_d) \tag{2.21}$$

where $g^{f_d}(t)$ is the decomposed sub-signal from $g(t)$ with respect to f_d.

Based on (2.18)-(2.21), the decomposition is conducted for the electric power deviation and angular frequency deviation of the i-th generator, and the decomposed sub-signals with respect to f_d are substituted into (2.16) to characterize the damping

contribution with respect to f_d. Then, a concept is given as **Definition 2.2**.

Definition 2.2. *The frequency-decomposed energy attenuation coefficient of the i-th generator with respect to an interested frequency f_d is defined as $K_{de,i}^{f_d}$ by (2.22).*

$$K_{de,i}^{f_d} = \frac{\int_0^{+\infty} \Delta P_{e,i}^{f_d}(t) \Delta \omega_i^{f_d}(t) \mathrm{d}t}{\int_0^{+\infty} \left(\Delta \omega_i^{f_d}(t) \right)^2 \mathrm{d}t} \tag{2.22}$$

where $K_{de,i}^{f_d}$ denotes the frequency-decomposed energy attenuation coefficient of the i-th generator with respect to f_d; $\Delta P_{e,i}^{f_d}(t)$ denotes the decomposed sub-signal from $\Delta P_{e,i}(t)$ with respect to f_d; and $\Delta \omega_i^{f_d}(t)$ denotes the decomposed sub-signal from $\Delta \omega_i(t)$ with respect to f_d.

If we repeat the calculation in (2.22) with respect to multiple frequencies (e.g., f_a, f_b, f_c, f_d …), the set $\left\{ K_{de,i}^{f_a} \; K_{de,i}^{f_b} \; K_{de,i}^{f_c} \; K_{de,i}^{f_d} \cdots \right\}$ can be obtained. It is seen that the frequency-decomposed energy attenuation coefficients calculated in the time domain can be represented as a spectrum with respect to multiple frequencies, which will be further analyzed in Section 2.4.

In the case studies of Section 2.5, the time-domain data of the electric power and angular frequency can be obtained by the real-life measurements or solving differential equations. In this chapter, the time-domain data of the electric power and angular frequency is obtained by solving the differential equations based on synchronous generator models. The power flow calculation is needed in the process of solving differential equations.

2.4 The Connection between Energy Flow Analysis and Damping Torque Analysis

In this section, the frequency spectrum analysis of the energy attenuation coefficient is conducted to demonstrate the consistency between EFA and DTA.

Using the Parseval's Theorem, the integral of the product of two real signals in the time domain can be conducted equivalently in the frequency domain, i.e., (2.23). It is noted that $g_1(t)=0$ and $g_2(t)=0$ when $t<0$.

$$\int_{-\infty}^{+\infty} g_1(t)g_2(t)\mathrm{d}t = \int_{-\infty}^{+\infty} G_1(f)G_2^*(f)\mathrm{d}f = \int_{-\infty}^{+\infty} G_1^*(f)G_2(f)\mathrm{d}f \tag{2.23}$$

where $g_1(t)$ and $g_2(t)$ are two signals in the time domain; $G_1(f)$ and $G_2(f)$ are the frequency-domain forms of $g_1(t)$ and $g_2(t)$ under the Fourier analysis; and $(\cdot)^*$ is the conjugate operator.

Let $G_1(f)=R_1(f)+\mathrm{j}X_1(f)$ and $G_2(f)=R_2(f)+\mathrm{j}X_2(f)$, and then (2.24) can be derived.

$$\begin{aligned} &G_1(f)G_2^*(f) = \big(R_1(f)+\mathrm{j}X_1(f)\big)\big(R_2(f)-\mathrm{j}X_2(f)\big) \\ &= R_1(f)R_2(f)+X_1(f)X_2(f)+\mathrm{j}\big(R_2(f)X_1(f)-R_1(f)X_2(f)\big) \end{aligned} \tag{2.24}$$

According to the Fourier analysis, (2.25) can be derived.

$$\begin{cases} R_1(f) = \int_{-\infty}^{+\infty} g_1(t)\cos(2\pi ft)\mathrm{d}t \\ X_1(f) = -\int_{-\infty}^{+\infty} g_1(t)\sin(2\pi ft)\mathrm{d}t \\ R_2(f) = \int_{-\infty}^{+\infty} g_2(t)\cos(2\pi ft)\mathrm{d}t \\ X_2(f) = -\int_{-\infty}^{+\infty} g_2(t)\sin(2\pi ft)\mathrm{d}t \end{cases} \tag{2.25}$$

It can be seen from (2.25) that $R_1(f)$ and $R_2(f)$ are the even functions with respect to f, while $X_1(f)$ and $X_2(f)$ are the odd functions with respect to f. On this basis, $R_1(f)R_2(f)$ and $X_1(f)X_2(f)$ are the even functions, while $R_1(f)X_2(f)$ and $R_2(f)X_1(f)$ are the odd

functions. Therefore, (2.23) can be further derived as (2.26).

$$\begin{aligned}&\int_{-\infty}^{+\infty} g_1(t)g_2(t)\mathrm{d}t = \int_{-\infty}^{+\infty} G_1(f)G_2^*(f)\mathrm{d}f \\ &= 2\int_0^{+\infty} \left(R_1(f)R_2(f) + X_1(f)X_2(f)\right)\mathrm{d}f \\ &= 2\int_0^{+\infty} \mathrm{Re}\left(G_1(f)G_2^*(f)\right)\mathrm{d}f\end{aligned} \tag{2.26}$$

By applying (2.26), (2.16) can be derived as (2.27). Eq. (2.27) implies that EFA is transformed from the time domain to frequency domain.

$$\frac{\int_0^{+\infty} \Delta P_{e,i}(t)\Delta\omega_i(t)\mathrm{d}t}{\int_0^{+\infty} \left(\Delta\omega_i(t)\right)^2 \mathrm{d}t} = \frac{\int_0^{+\infty} \mathrm{Re}\left(\Delta P_{e,i}(f)\Delta\omega_i^*(f)\right)\mathrm{d}f}{\int_0^{+\infty} \mathrm{Re}\left(\Delta\omega_i(f)\Delta\omega_i^*(f)\right)\mathrm{d}f} \tag{2.27}$$

Normally, for an oscillation mode with respect to the particular frequency f_d, (2.27) becomes (2.28).

$$\frac{\int_0^{+\infty} \Delta P_{e,i}^{f_d}(t)\Delta\omega_i^{f_d}(t)\mathrm{d}t}{\int_0^{+\infty} \left(\Delta\omega_i^{f_d}(t)\right)^2 \mathrm{d}t} = \frac{\int_0^{+\infty} \mathrm{Re}\left(\Delta P_{e,i}(f_d)\Delta\omega_i^*(f_d)\right)\mathrm{d}f}{\int_0^{+\infty} \mathrm{Re}\left(\Delta\omega_i(f_d)\Delta\omega_i^*(f_d)\right)\mathrm{d}f} \tag{2.28}$$

It should be noted that $\Delta P_{e,i}(f_d)$, $\Delta\omega_i(f_d)$ and $\Delta\omega_i^*(f_d)$ are all constant complex numbers at the frequency f_d, and hence the integral operator in (2.28) actually collapses. In fact, the product of $\Delta\omega_i(f_d)$ and $\Delta\omega_i^*(f_d)$ is a real number. Considering the coefficient proposed in (2.22), (2.29) can be obtained.

$$K_{de,i}^{f_d} = \mathrm{Re}\left(\frac{\Delta P_{e,i}(f_d)\Delta\omega_i^*(f_d)}{\Delta\omega_i(f_d)\Delta\omega_i^*(f_d)}\right) = \mathrm{Re}\left(\frac{\Delta P_{e,i}(f_d)}{\Delta\omega_i(f_d)}\right) \tag{2.29}$$

The following **Theorem 2.1** can be summarized by comparing (2.29) with (2.7) and (2.8).

Theorem 2.1. *For the i-th generator, the aggregated damping torque coefficient is essentially equivalent to the frequency-decomposed energy attenuation coefficient with*

respect to the oscillation frequency f_d, i.e.,

$$K_{de,i}^{f_d} = K_{da,i}(f_d) \tag{2.30}$$

2.5 Case Studies

The consistency of the proposed coefficients reflecting the damping performance calculated by (2.8), (2.22) and (2.29) is verified by the numerical calculation in both the SMIB power system and multi-machine power system in this section. The 6th-order model of synchronous generators [115] and the transfer functions of AVR and PSS are given by (A.1) and Fig. A.1 in the Appendix A.1.

Matlab programming is employed to conduct the numerical calculations of $K_{da,i}(f_d)$ and $K_{de,i}^{f_d}$, i.e., Step 1-Step 6.

Step 1: assume a set-up disturbance happens at the i-th generator in a power system;

Step 2: the time-domain solutions of $P_{e,i}(t)$ and $\omega_i(t)$ of the i-th generator are obtained by solving the differential equations; then, $\Delta P_{e,i}(t)$ and $\Delta\omega_i(t)$ are calculated from $P_{e,i}(t)$ and $\omega_i(t)$;

Step 3: the amplitude-frequency characteristic of $\Delta P_{e,i}(t)$ is obtained through the Fourier analysis, where the frequency of each dominant oscillation mode can be observed; then, select an interested oscillation mode at the frequency f_d;

Step 4: the modeling is conducted via (2.3); then, $K_{da,i}(f_d)$ is calculated by substituting the block sub-matrices of the state matrix and f_d into (2.8);

Step 5: $\Delta P_{e,i}(t)$ and $\Delta\omega_i(t)$ are decomposed as $\Delta P_{e,i}^{f_d}(t)$ and $\Delta\omega_i^{f_d}(t)$ by applying (2.18)-(2.21) with respect to f_d, and then (2.22) is applied to calculate $K_{de,i}^{f_d}$ in the time domain;

Step 6: Eq. (2.29) is applied to calculate $K_{de,i}^{f_d}$ in the frequency domain.

Finally, the numerical results from (2.8), (2.22) and (2.29) need to be compared to verify the consistency of DTA and EFA.

2.5.1 Verification in a Single-machine Infinite-bus Power System

The line diagram of the SMIB power system is shown in Fig. 2.2.

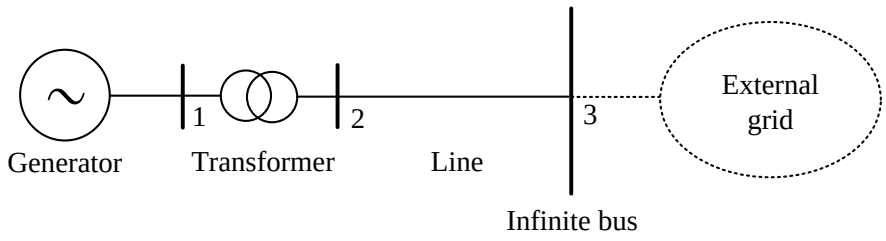

Fig. 2.2. Line diagram of an SMIB power system.

The parameters of this power system are given in the Appendix A.1. A step-up disturbance happens to the mechanical power of the generator at 0.2 s, i.e., P_m=1.1P_{m0}, and lasts for 0.1 s. There is no installation of PSS. The eigenvalue of the state matrix is computed to be -0.1021+j7.9095.

The simulation results of $\Delta P_e(t)$ and its amplitude-frequency characteristic are shown in Fig. 2.3. It is seen that there is only one dominant oscillation mode at around 1.26 Hz.

The plot of the angular frequency deviation $\Delta\omega(t)$ and its amplitude-frequency characteristic are given by Fig. 2.4. It is seen that there is only one oscillation mode at around 1.26 Hz, which is consistent with that in Fig. 2.3 (b).

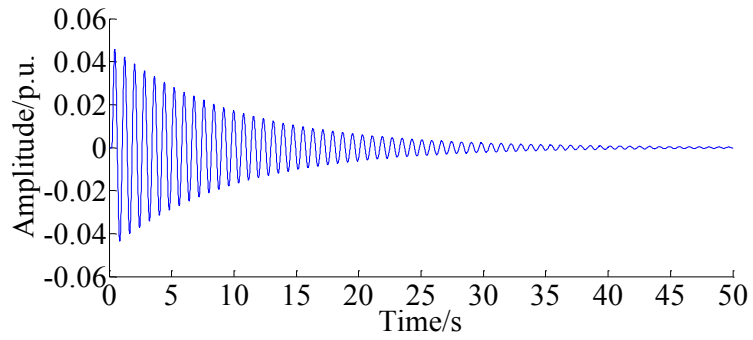

(a)

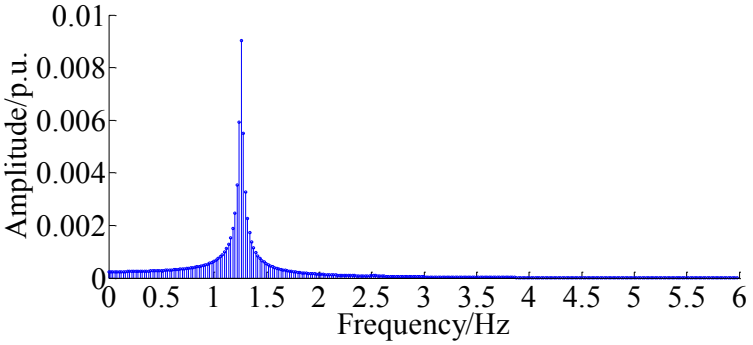

(b)

Fig. 2.3. $\Delta P_e(t)$ and its amplitude-frequency characteristic. (a) Plot of $\Delta P_e(t)$ in time domain. (b) Amplitude-frequency characteristic of $\Delta P_e(t)$ in frequency domain.

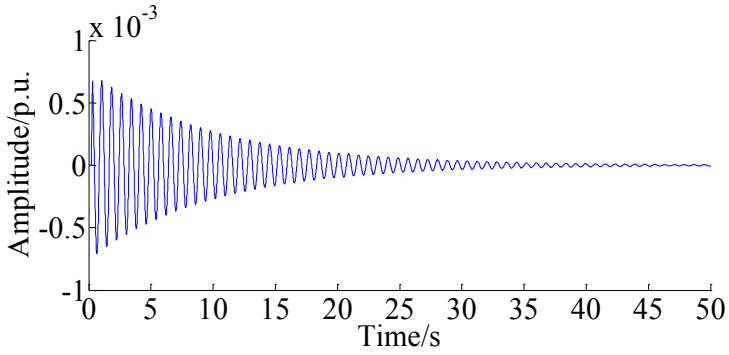

(a)

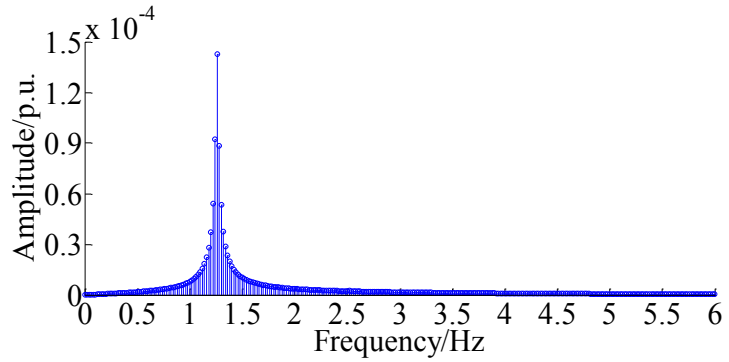

(b)

Fig. 2.4. $\Delta\omega(t)$ and its amplitude-frequency characteristic. (a) Plot of $\Delta\omega(t)$ in time domain. (b) Amplitude-frequency characteristic of $\Delta\omega(t)$ in frequency domain.

The aggregated damping torque coefficient and frequency-decomposed energy

attenuation coefficient at 1.26 Hz are calculated by (2.8), (2.22) and (2.29), respectively. The calculation results are shown in Table 2.1, which verifies the consistency.

Table 2.1 Calculation of proposed coefficients in an SMIB power system.

	DTA by (2.8)	EFA by (2.22)	EFA by (2.29)
Calculation results	1.6221	1.6054	1.6308

Generally, the numerical calculation from DTA is considered to be accurate because DTA is a modeling-based method. While the numerical calculation from EFA is regarded as an estimation because EFA is a measurement-based method.

Eq. (2.8) is from DTA, (2.22) is from EFA in the time domain and (2.29) is from EFA in the frequency domain. The computing time by (2.8), (2.22) and (2.29) in this SMIB power system is 0.12 s, 0.14 s and 0.03 s, respectively. Compared with DTA (i.e., (2.8)), the error of (2.22)-based EFA is -1.03%, while the error of (2.29)-based EFA is 0.54%. It is seen that the error of EFA is within an acceptable range.

2.5.2 Verification in a 4-machine 2-area Power System

The 4-machine 2-area (4M2A) power system is used as an example in this sub-section, which is illustrated by Fig. 2.5.

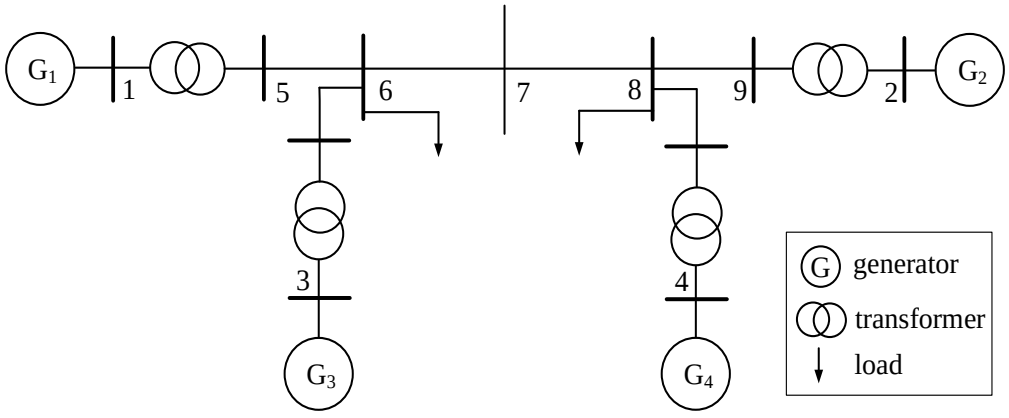

Fig. 2.5. Line diagram of a 4M2A power system.

The parameters of the generators, transmission lines and loads are presented in the Appendix A.1, which is cited from [115] and [116]. The based capacity of this 4M2A power system is 100 MVA. A step-up disturbance occurs in the mechanical power of the G_1 at 0.5 s, i.e., $P_{m,1}$=1.05$P_{m0,1}$, and lasts for 0.05 s.

The four generators are all equipped with AVR and PSS with the same parameter settings. Three scenarios are designed as follows:

Scenario 1.1: $K_{a,i}$=60.0, $T_{a,i}$=0.055 s; $K_{pss,i}$=8.0, $T_{1,i}$=$T_{3,i}$=5.0 s, $T_{2,i}$=$T_{4,i}$=3.0 s;

Scenario 1.2: $K_{a,i}$=70.0, $T_{a,i}$=0.055 s; $K_{pss,i}$=7.0, $T_{1,i}$=$T_{3,i}$=5.0 s, $T_{2,i}$=$T_{4,i}$=3.0 s;

Scenario 1.3: $K_{a,i}$=80.0, $T_{a,i}$=0.055 s; $K_{pss,i}$=6.0, $T_{1,i}$=$T_{3,i}$=5.0 s, $T_{2,i}$=$T_{4,i}$=3.0 s.

As for the neglecting of the reactive power in (2.9), the comparison of the oscillatory energy flow with and without the consideration of the reactive power is conducted at G_1 in Scenario 1.1. The results are given in Fig. 2.6. It is seen that the influence of the reactive power is very small, which can be ignored.

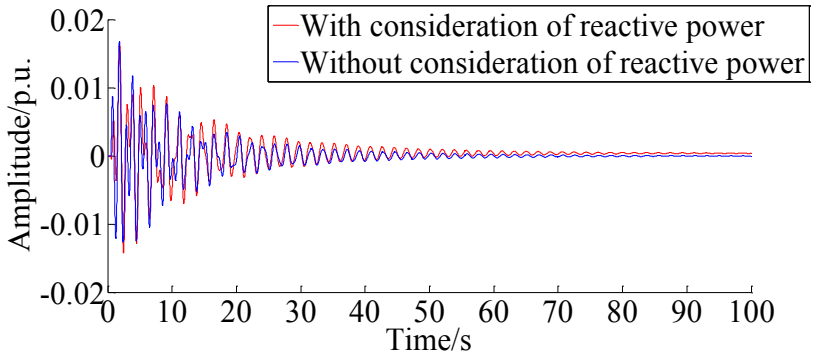

Fig. 2.6. Oscillatory energy flow with and without consideration of reactive power at G_1 in Scenario 1.1.

$\Delta P_{e,1}(t)$ and the amplitude-frequency characteristics for three scenarios are displayed in Fig. 2.7-2.9, respectively.

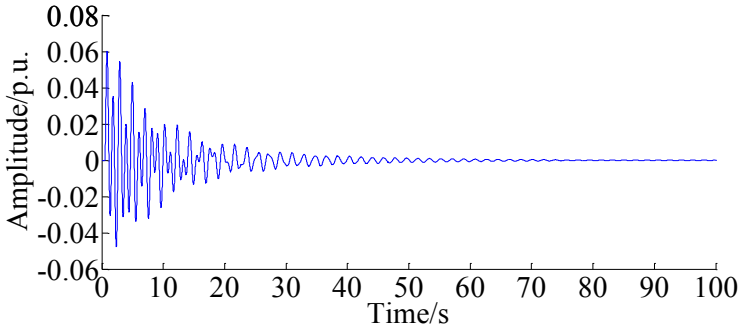

(a)

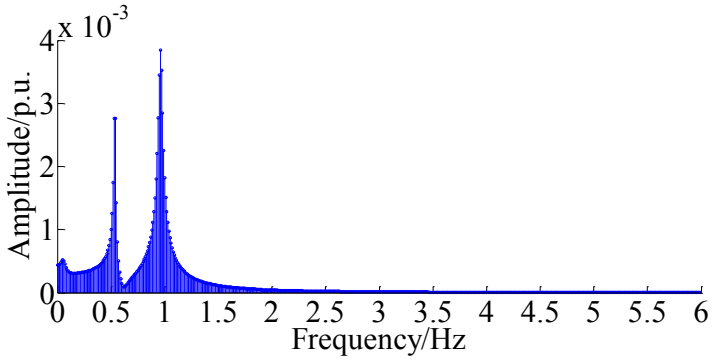

(b)

Fig. 2.7. $\Delta P_{e,1}(t)$ and its amplitude-frequency characteristic in Scenario 1.1. (a). Plot of $\Delta P_{e,1}(t)$ in time domain. (b). Amplitude-frequency characteristic of $\Delta P_{e,1}(t)$ in frequency domain.

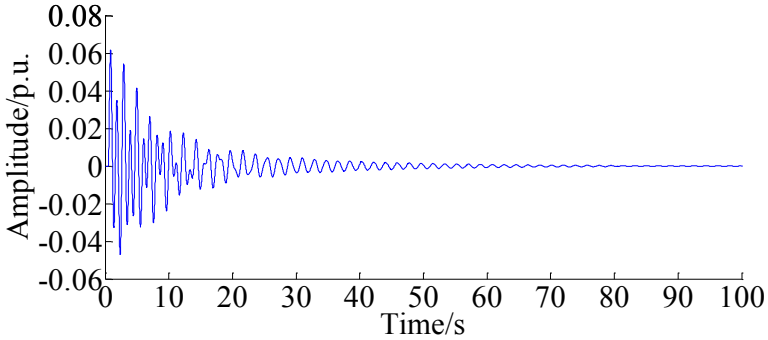

(a)

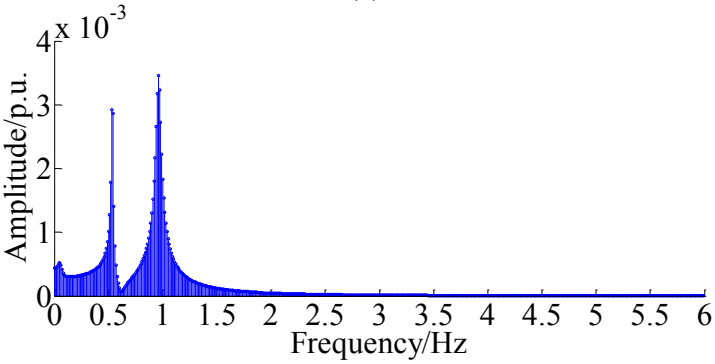

(b)

Fig. 2.8. $\Delta P_{e,1}(t)$ and its amplitude-frequency characteristic in Scenario 1.2. (a) Plot of $\Delta P_{e,1}(t)$ in time domain. (b) Amplitude-frequency characteristic of $\Delta P_{e,1}(t)$ in frequency domain.

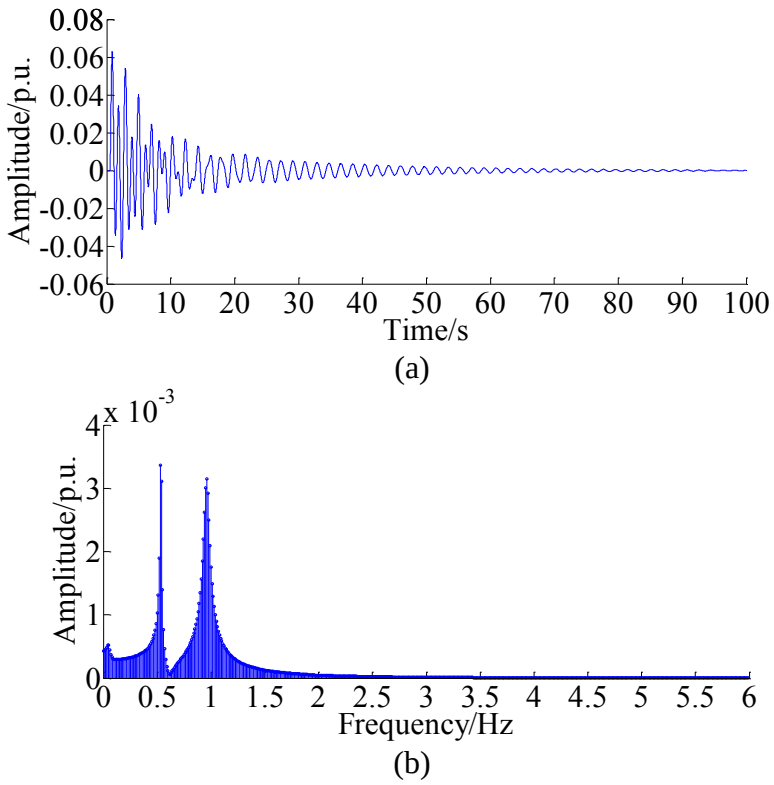

Fig. 2.9. $\Delta P_{e,1}(t)$ and its amplitude-frequency characteristic in Scenario 1.3. (a) Plot of $\Delta P_{e,1}(t)$ in time domain. (b) Amplitude-frequency characteristic of $\Delta P_{e,1}(t)$ in frequency domain.

It can be seen that there is an inter-area oscillation mode at around 0.53-0.54 Hz, which is the focus of this case study. The eigenvalues of the inter-area oscillation mode for the three scenarios are -0.0590+j3.3618, -0.0541+j3.3608 and -0.0454+j3.3580. The real part of the eigenvalue indicates the damping. By comparing the real parts of the three eigenvalues, it can be found that the damping performance of Scenario 1.1 is better.

The calculation results of the aggregated damping torque coefficient by (2.8) and frequency-decomposed energy attenuation coefficient by (2.22) and (2.29) for the three scenarios are demonstrated by Table 2.2, which shows the consistency.

Table 2.2 Calculation of proposed coefficients in a 4M2A power system.

	DTA by (2.8)	EFA by (2.22)	EFA by (2.29)
Calculation in Scenario 1.1	44.71	45.34	45.37
Calculation in Scenario 1.2	43.94	44.18	44.21
Calculation in Scenario 1.3	38.93	38.11	38.14

The difference between EFA and DTA mainly comes from the following aspects: (1) the fast Fourier transform is applied to analyze the amplitude-frequency characteristic of a signal in Matlab. Since the fast Fourier transform is discrete, the frequency of an oscillation mode may fall between two adjacent spectral lines, which brings a slight error to the displayed amplitude; (2) the reactive power is ignored in (2.9), which leads to a slight error; and (3) the integral operation is obtained by accumulating the rectangular areas within the time interval, which causes a slight error. However, the results are generally within the acceptable range.

The damping performance assessment through different approaches is given by Table 2.3, and their assessment results are consistent. It is noted that the number of ☆ indicates the degree of damping performance. It can be concluded from the case studies that the proposed coefficients can be the new indicator for the qualitative assessment of the damping performance, which can be obtained from either the time or frequency domain.

Table 2.3 Comparison of qualitative assessment of damping performance through multiple approaches.

	Via eigenvalue	Via DTA	Via EFA
Assessment in Scenario 1.1	☆☆☆	☆☆☆	☆☆☆
Assessment in Scenario 1.2	☆☆	☆☆	☆☆
Assessment in Scenario 1.3	☆	☆	☆

In order to demonstrate the relationship between the eigenvalue (or damping ratio) and the proposed frequency-decomposed energy attenuation coefficient (or aggregated damping torque coefficient), $K_{a,i}$ is randomly adjusted 1000 times between 40.0 and 80.0, and $K_{pss,i}$ is randomly adjusted 1000 times between 4.0 and 8.0. Thus, 1000 simulation scenarios are established to obtain a dense scatter diagram, as shown by the blue scatter points in Fig. 2.10 and 2.11. The fitting is represented by the red curves in Fig. 2.10 and 2.11.

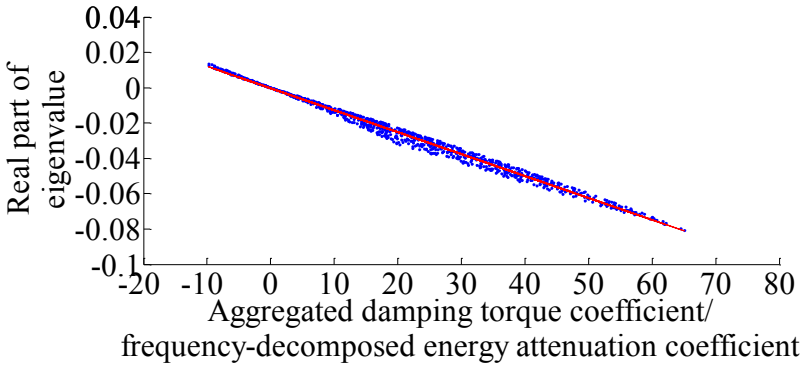

Fig. 2.10. Relationship between frequency-decomposed energy attenuation coefficient (or aggregated damping torque coefficient) and real part of eigenvalue.

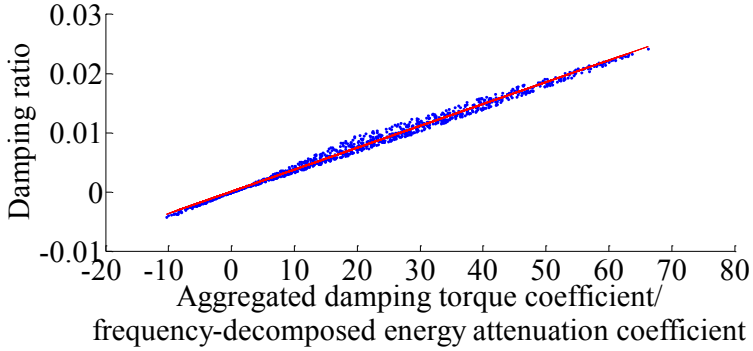

Fig. 2.11. Relationship between frequency-decomposed energy attenuation coefficient (or aggregated damping torque coefficient) and damping ratio.

It can be revealed that there is an approximate linear relationship between the frequency-decomposed energy attenuation coefficient (or aggregated damping torque coefficient) and the damping ratio (or real part of the eigenvalue). In other words, the frequency-decomposed energy attenuation coefficient (or aggregated damping torque

coefficient) provides a new indicator to qualitatively assess the damping performance of the whole system, which provides the important reference for the parameter setting of external stabilizers.

The application of the proposed concepts to qualitatively investigate the electromechanical oscillations of the multi-machine power system is suggested as follows.

In order to qualitatively evaluate the damping performance based on the concept of the aggregated damping torque coefficient, the mathematical models of all power components should be available, and the state-space modelling of the whole power system should be conducted. Then, (2.8) is applied to calculate the aggregated damping torque coefficient.

The concept of the frequency-decomposed energy attenuation coefficient proposed for EFA shows a clear advantage in the large-scale power system with a large number of complex power components. The mathematical models of power components are unnecessary to be known, and the high-dimensional modeling can be avoided. In order to qualitatively evaluate the damping performance based on EFA, the measurements at the terminal of a local generator should be monitored. After that, (2.22) or (2.29) can be applied to calculate the frequency-decomposed energy attenuation coefficient.

2.6 Summary

The key findings of this chapter are summarized as follows: (1) through the case studies in both the SMIB power system and 4M2A power system, the consistency of

the aggregated damping torque coefficient and the frequency-decomposed energy attenuation coefficient is numerically verified; and (2) the relationship between the frequency-decomposed energy attenuation coefficient (or aggregated damping torque coefficient) and the eigenvalue (or damping ratio) is numerically disclosed, which further demonstrates the application of the proposed concepts in the qualitative assessment of the system damping.

Chapter 3

A Novel Energy Flow Analysis and Its Connection with Modal Analysis for Investigating Electromechanical Oscillations

3.1 Overview

In Chapter 2, the consistency between EFA and DTA is derived and discussed to explain the oscillatory damping mechanism. The conclusion in Chapter 2 can be used for the qualitative investigation of the electromechanical oscillation, but the related quantitative analysis is limited. In this chapter, a novel EFA is proposed based on the signal reconstruction and decomposition to quantitatively investigate the electromechanical oscillations. In contrast to the research in Chapter 2, the connection between the proposed EFA and MA can be quantitatively revealed for arbitrary models of synchronous generators in multi-machine power systems. Firstly, TDI of the proposed EFA is designed. Specifically, the measurements at the terminal of a local generator are reconstructed through an exponential operator and then decomposed with respect to an angular frequency. Then, the mode-screened damping torque coefficient is defined to extract the damping feature with respect to an electromechanical oscillation mode. After that, FDI is derived. Specifically, the Parseval's Theorem is applied to transform the proposed EFA from the time domain to frequency domain. On

this basis, the consistency between the proposed EFA and MA is strictly proved, which is applicable for arbitrary models of synchronous generators in multi-machine power systems. Additionally, the application procedure of the proposed EFA in quantitatively investigating electromechanical oscillations is given. Finally, the proposed EFA are substantially demonstrated in multiple case studies.

3.2 Time-domain Implementation

In this section, TDI of the proposed EFA is developed based on the signal reconstruction and decomposition to quantitatively extract the damping feature with respect to an electromechanical oscillation mode in the multi-machine power system. When an electromechanical oscillation event occurs, the damping effect of generators as well as external stabilizers leads to the dissipation of the oscillatory energy flow. According to [91], the oscillatory energy flow into the generator is divided into two parts. One is related to the active power–frequency control loop, and the other is related to the reactive power–voltage control loop. In fact, the change of the damping contribution is essentially owing to the regulation of the active power by the relevant controllers. Thus, the oscillatory energy flow related to the active power–frequency control loop of the *i*-th generator is mainly analyzed.

According to the discussion in Chapter 2, the dissipation of the oscillatory energy flow of the *i*-th generator can be calculated by (2.11) using the measurements at the terminal of the local generator. Additionally, in the studies of the oscillatory stability, the electric power deviation is considered approximately be equal to the electric torque

deviation. In this view, the damping torque coefficient can be derived as (2.15).

For a power system with multiple generators, the measurements at the terminal of a local generator are coupled with multiple electromechanical oscillation modes. Thus, $K_{d,i}$ obtained by (2.15) is actually associated with multiple oscillation modes, which cannot be effectively used to quantitatively indicate the damping feature with respect to an electromechanical oscillation mode.

In order to enable (2.15) to quantitatively characterize the damping feature with respect to an electromechanical oscillation mode, the pre-processing of the measurements in Chapter 2 should be improved. According to the Laplace analysis, the concept of signal reconstruction and decomposition is discussed. The principle of the Laplace analysis can be expressed by (3.1), which is the analysis of double-variables, i.e., $s=\sigma+\mathrm{j}w$.

$$G(s)=\int_0^{+\infty} g(t)\mathrm{e}^{-st}\mathrm{d}t=\int_0^{+\infty}\left(g(t)\mathrm{e}^{-\sigma t}\right)\mathrm{e}^{-\mathrm{j}wt}\mathrm{d}t \tag{3.1}$$

where s is the Laplacian operator; σ is the real part of s; w is the imaginary part of s; $G(s)$ is the frequency-domain form of $g(t)$ under the Laplace analysis. The meanings of other variables are the same as those in Chapter 2.

For a real signal, it should be noted that $g(t)=0$ when $t<0$. Then, it can be seen from (3.1) that the Laplace analysis of $g(t)$ can be regarded as the Fourier analysis of $g(t)\mathrm{e}^{-\sigma t}$. On this basis, the signal reconstruction is defined as

$$g(t\,|\,\sigma)=g(t)\mathrm{e}^{-\sigma t} \tag{3.2}$$

where $g(t\,|\,\sigma)$ is the reconstructed signal from $g(t)$ by operator $\mathrm{e}^{-\sigma t}$.

In practice, the integral interval of (3.1) is $0<t<t_z$, where t_z is the signal length in the time domain. When $\sigma=0$, $e^{-\sigma t}=1$ and the Laplace analysis of $g(t)$ becomes its Fourier analysis. For an electromechanical oscillation mode $\lambda_d=\sigma_d\pm jw_d$ associated with a local generator, the amplitude-frequency and phase-frequency spectrum of the reconstructed signal $g(t \mid \sigma_d)$ can be obtained by (3.3)-(3.5). $G(w \mid \sigma_d)$ is the Fourier analysis of $g(t \mid \sigma_d)$ or the Laplace analysis of $g(t)$ with respect to $\sigma=\sigma_d$ and a set of angular frequencies $\boldsymbol{w}_{1\times q}=[w_1, w_2, \ldots, w_q]$. It noted that the angular frequency variable w is adopted in Chapter 3.

$$G(w \mid \sigma_d)=\int_0^{+\infty} g(t \mid \sigma_d)e^{-jwt}\mathrm{d}t \tag{3.3}$$

$$\boldsymbol{M}_{1\times q}=\left|G(w \mid \sigma_d)\right| \tag{3.4}$$

$$\boldsymbol{\beta}_{1\times q}=\arg\left(G(w \mid \sigma_d)\right) \tag{3.5}$$

where λ_d is a pair of eigenvalues with respect to an electromechanical oscillation mode; σ_d is the real part of λ_d; w_d is the imaginary part of λ_d; $g(t \mid \sigma_d)$ is $g(t \mid \sigma)$ with respect to $\sigma=\sigma_d$; $G(w \mid \sigma_d)$ is the frequency-domain form of $g(t \mid \sigma_d)$ under the Fourier analysis; q is the number of decomposed sub-signals from $g(t \mid \sigma_d)$; $\boldsymbol{w}_{1\times q}$ is the q-dimensional vector of angular frequencies of decomposed sub-signals from $g(t \mid \sigma_d)$; w_q is the q-th element in $\boldsymbol{w}_{1\times q}$; $\boldsymbol{M}_{1\times q}$ is the q-dimensional vector of amplitudes of decomposed sub-signals from $g(t \mid \sigma_d)$; and $\boldsymbol{\beta}_{1\times q}$ is the q-dimensional vector of phase angles of decomposed sub-signals from $g(t \mid \sigma_d)$. The meanings of other variables are the same as those in Chapter 2.

In the time domain, the reconstructed signal $g(t \mid \sigma_d)$ is equivalent to the sum of a series of sub-signals with the form of (3.6) with respect to $\sigma=\sigma_d$ and a set of angular

frequencies $\boldsymbol{w}_{1\times q}=[w_1, w_2, \ldots, w_q]$.

$$g(t \mid \sigma_d) = \sum_{k=1}^{q} M_k \cos(w_k t + \beta_k) \tag{3.6}$$

where w_k is the angular frequency of the k-th decomposed sub-signal from $g(t \mid \sigma_d)$; M_k is the amplitude of the k-th decomposed sub-signal from $g(t \mid \sigma_d)$; and β_k is the phase angle of the k-th decomposed sub-signal from $g(t \mid \sigma_d)$.

The amplitude M_d ($M_d \in \boldsymbol{M}_{1\times q}$) and phase angle β_d ($\beta_d \in \boldsymbol{\beta}_{1\times q}$) with respect to the angular frequency w_d ($w_d \in \boldsymbol{w}_{1\times q}$) can be observed from the amplitude-frequency and phase-frequency spectrum. It should be noted that w_d indicates the imaginary part of λ_d rather than the d-th element in $\boldsymbol{w}_{1\times p}$. M_d is the amplitude of the decomposed sub-signal with respect to $w=w_d$, and β_d is the phase angle of the decomposed sub-signal with respect to $w=w_d$. Then, the decomposed sub-signal from $g(t \mid \sigma_d)$ with respect to the angular frequency w_d is given by

$$g^{w_d}(t \mid \sigma_d) = M_d \cos(w_d t + \beta_d) \tag{3.7}$$

where $g^{w_d}(t \mid \sigma_d)$ is the decomposed sub-signal from $g(t \mid \sigma_d)$ with respect to $w=w_d$.

Based on the discussion above, let $\sigma=\sigma_d$ and (3.2) is applied to reconstruct $\Delta P_{e,i}(t)$ and $\Delta\omega_i(t)$ as $\Delta P_{e,i}(t \mid \sigma_d)$ and $\Delta\omega_i(t \mid \sigma_d)$ with respect to σ_d, i.e., (3.8) and (3.9).

$$\Delta P_{e,i}(t \mid \sigma_d) = \Delta P_{e,i}(t)\mathrm{e}^{-\sigma_d t} \tag{3.8}$$

$$\Delta\omega_i(t \mid \sigma_d) = \Delta\omega_i(t)\mathrm{e}^{-\sigma_d t} \tag{3.9}$$

where $\Delta P_{e,i}(t \mid \sigma_d)$ is the reconstructed signal from $\Delta P_{e,i}(t)$ by operator $\mathrm{e}^{-\sigma_d t}$; and $\Delta\omega_i(t \mid \sigma_d)$ is the reconstructed signal from $\Delta\omega_i(t)$ by operator $\mathrm{e}^{-\sigma_d t}$.

Then, (3.3)-(3.5) and (3.7) are applied to decompose $\Delta P_{e,i}(t \mid \sigma_d)$ and $\Delta\omega_i(t \mid \sigma_d)$ to

be $\Delta P_{e,i}^{w_d}(t \mid \sigma_d)$ and $\Delta \omega_i^{w_d}(t \mid \sigma_d)$ with respect to w_d. On this basis, a new concept $K_{d,i}^{\lambda_d}$ is given in the **Definition 3.1** below. Compared with the research in Chapter 2, the damping feature with respect to $\lambda_d=\sigma_d \pm \mathrm{j}w_d$ is quantitatively extracted from the perspective of the *i*-th generator via (3.10).

Definition 3.1. *The mode-screened damping torque coefficient with respect to the electromechanical oscillation mode λ_d is defined as*

$$K_{d,i}^{\lambda_d}=\frac{\int_0^{+\infty}\Delta P_{e,i}^{w_d}(t \mid \sigma_d)\Delta \omega_i^{w_d}(t \mid \sigma_d)\mathrm{d}t}{\int_0^{+\infty}\left(\Delta \omega_i^{w_d}(t \mid \sigma_d)\right)^2 \mathrm{d}t} \tag{3.10}$$

where $\Delta P_{e,i}^{w_d}(t \mid \sigma_d)$ is the decomposed sub-signal from $\Delta P_{e,i}(t \mid \sigma_d)$ with respect to $w=w_d$; $\Delta \omega_i^{w_d}(t \mid \sigma_d)$ is the decomposed sub-signal from $\Delta \omega_i(t \mid \sigma_d)$ with respect to $w=w_d$; and $K_{d,i}^{\lambda_d}$ is the mode-screened damping torque coefficient of the *i*-th generator with respect to λ_d.

3.3 Frequency-domain Implementation

In this section, the proposed EFA in Section 3.2 is transformed from the time domain to frequency domain (i.e., its FDI), which is later employed for essentially revealing the connection between the proposed EFA and MA in the next section.

According to the discussion in Chapter 2, the integral of the product of two real signals can be conducted equivalently in the frequency domain through the Parseval's Theorem. The equation of the Parseval's Theorem with respect to the angular frequency is represented by

$$\int_{-\infty}^{+\infty} g_1(t)g_2(t)\mathrm{d}t = \frac{1}{2\pi}\int_{-\infty}^{+\infty} G_1(w)G_2^*(w)\mathrm{d}w$$
$$= \frac{1}{\pi}\int_0^{+\infty} \mathrm{Re}\left(G_1(w)G_2^*(w)\right)\mathrm{d}w \tag{3.11}$$

where $G_1(w)$ and $G_2(w)$ are the frequency-domain forms of $g_1(t)$ and $g_2(t)$ under the Fourier analysis with respect to the angular frequency. The meanings of other variables are the same as those in Chapter 2.

It should be emphasized here that the frequency variable *f* is used in Chapter 2, and the angular frequency variable *w* is used in Chapter 3. Thus, the equation of the Parseval's Theorem is slightly different from that in Chapter 2.

Based on (3.2), two real signals $g_1(t)$ and $g_2(t)$ are reconstructed as

$$g_1(t \mid \sigma_d) = g_1(t)e^{-\sigma_d t} \tag{3.12}$$

$$g_2(t \mid \sigma_d) = g_2(t)e^{-\sigma_d t} \tag{3.13}$$

where $g_1(t \mid \sigma_d)$ is the reconstructed signal from $g_1(t)$ by operator $e^{-\sigma_d t}$; and $g_2(t \mid \sigma_d)$ is the reconstructed signal from $g_2(t)$ by operator $e^{-\sigma_d t}$.

Substitute $g_1(t \mid \sigma_d)$ and $g_2(t \mid \sigma_d)$ into (3.11), and then (3.14) can be obtained.

$$\int_{-\infty}^{+\infty} g_1(t \mid \sigma_d)g_2(t \mid \sigma_d)\mathrm{d}t = \frac{1}{\pi}\int_0^{+\infty} \mathrm{Re}\left(G_1(w \mid \sigma_d)G_2^*(w \mid \sigma_d)\right)\mathrm{d}w \tag{3.14}$$

where $G_1(w \mid \sigma_d)$ and $G_2(w \mid \sigma_d)$ are the frequency-domain forms of $g_1(t \mid \sigma_d)$ and $g_2(t \mid \sigma_d)$ under the Fourier analysis.

The measurements $\Delta P_{e,i}(t)$ and $\Delta\omega_i(t)$ monitored at the terminal of the *i*-th generator are reconstructed based on (3.8) and (3.9). Then, (3.15) can be derived by applying (3.14).

$$\frac{\int_0^{+\infty}\Delta P_{e,i}(t\,|\,\sigma_d)\Delta\omega_i(t\,|\,\sigma_d)\mathrm{d}t}{\int_0^{+\infty}\left(\Delta\omega_i(t\,|\,\sigma_d)\right)^2\mathrm{d}t}=\frac{\int_0^{+\infty}\mathrm{Re}\left(\Delta P_{e,i}(w\,|\,\sigma_d)\Delta\omega_i^*(w\,|\,\sigma_d)\right)\mathrm{d}w}{\int_0^{+\infty}\mathrm{Re}\left(\Delta\omega_i(w\,|\,\sigma_d)\Delta\omega_i^*(w\,|\,\sigma_d)\right)\mathrm{d}w} \tag{3.15}$$

where $\Delta P_{e,i}(w\,|\,\sigma_d)$ and $\Delta\omega_i(w\,|\,\sigma_d)$ are the frequency-domain forms of $\Delta P_{e,i}(t\,|\,\sigma_d)$ and $\Delta\omega_i(t\,|\,\sigma_d)$ under the Fourier analysis.

For a specific electromechanical oscillation mode λ_d, (3.10) can be equivalently derived as (3.16) based on (3.15).

$$\begin{aligned}K_{d,i}^{\lambda_d}&=\frac{\int_0^{+\infty}\Delta P_{e,i}^{w_d}(t\,|\,\sigma_d)\Delta\omega_i^{w_d}(t\,|\,\sigma_d)\mathrm{d}t}{\int_0^{+\infty}\left(\Delta\omega_i^{w_d}(t\,|\,\sigma_d)\right)^2\mathrm{d}t}\\&=\frac{\int_0^{+\infty}\mathrm{Re}\left(\Delta P_{e,i}(w_d\,|\,\sigma_d)\Delta\omega_i^*(w_d\,|\,\sigma_d)\right)\mathrm{d}w}{\int_0^{+\infty}\mathrm{Re}\left(\Delta\omega_i(w_d\,|\,\sigma_d)\Delta\omega_i^*(w_d\,|\,\sigma_d)\right)\mathrm{d}w}\end{aligned} \tag{3.16}$$

where $\Delta P_{e,i}(w_d\,|\,\sigma_d)$ is $\Delta P_{e,i}(w\,|\,\sigma_d)$ with respect to $w=w_d$; and $\Delta\omega_i(w_d\,|\,\sigma_d)$ is $\Delta\omega_i(w\,|\,\sigma_d)$ with respect to $w=w_d$.

It is noted that $\Delta P_{e,i}(w_d\,|\,\sigma_d)$, $\Delta\omega_i(w_d\,|\,\sigma_d)$ and $\Delta\omega_i^*(w_d\,|\,\sigma_d)$ are the constant complex numbers, and the product of $\Delta\omega_i(w_d\,|\,\sigma_d)$ and $\Delta\omega_i^*(w_d\,|\,\sigma_d)$ is a real number. Therefore, the integral operator in (3.16) collapses, i.e., (3.17).

$$K_{d,i}^{\lambda_d}=\mathrm{Re}\left(\frac{\Delta P_{e,i}(w_d\,|\,\sigma_d)\Delta\omega_i^*(w_d\,|\,\sigma_d)}{\Delta\omega_i(w_d\,|\,\sigma_d)\Delta\omega_i^*(w_d\,|\,\sigma_d)}\right)=\mathrm{Re}\left(\frac{\Delta P_{e,i}(w_d\,|\,\sigma_d)}{\Delta\omega_i(w_d\,|\,\sigma_d)}\right) \tag{3.17}$$

The discussion in this section implies that the proposed EFA is transformed from the time domain to frequency domain. TDI and FDI of the proposed EFA are essentially equivalent. In other words, (3.10) and (3.17) are essentially consistent.

3.4 The Connection between the Proposed Energy Flow Analysis and Modal Analysis

In Section 3.2, a novel EFA is proposed based on the signal reconstruction and decomposition in the time domain, i.e., its TDI. In Section 3.3, the proposed EFA is converted from the time domain to frequency domain, i.e., its FDI. In this section, the proposed EFA is proved to be consistent with MA in the frequency domain. The proposed mode-screened damping torque coefficient is connected with the eigenvalue, which lays a foundation for the application procedure of the proposed EFA in Section 3.5.

In order to represent the whole power system considering the arbitrary models of synchronous generators, the linearization of a multi-machine power system is derived as (3.18) through the Laplace analysis by adding the equations that characterize the AVRs, PSSs, etc.

$$\begin{bmatrix} s\Delta\delta_i(s) \\ s\Delta\omega_i(s) \\ s\Delta\boldsymbol{Z}(s) \end{bmatrix} = \begin{bmatrix} 0 & \omega_0 & \mathbf{0} \\ A_{21} & -\dfrac{D_i}{T_{J,i}} & \boldsymbol{A}_{23} \\ \boldsymbol{A}_{31} & \boldsymbol{A}_{32} & \boldsymbol{A}_{33} \end{bmatrix} \begin{bmatrix} \Delta\delta_i(s) \\ \Delta\omega_i(s) \\ \Delta\boldsymbol{Z}(s) \end{bmatrix} \tag{3.18}$$

where $\Delta\delta_i(s)$, $\Delta\omega_i(s)$ and $\Delta\boldsymbol{Z}(s)$ are the frequency-domain forms of $\Delta\delta_i(t)$, $\Delta\omega_i(t)$ and $\Delta\boldsymbol{Z}(t)$ under the Laplace analysis. The meanings of other variables are the same as those in Chapter 2.

Similar to the discussion in Chapter 2, $\Delta\boldsymbol{Z}(s)$ includes the state variables of the *i*-th generator excluding $\Delta\delta_i(s)$ and $\Delta\omega_i(s)$, as well as all the state variables of other generators. Eq. (3.18) uses the *i*-th generator as an example, and the damping contribution of the whole power system is aggregated to the selected generator (i.e., the *i*-th generator). The

linearized representation of a multi-machine power system under the Laplace analysis can be shown in Fig. 3.1, where $\Delta P_{e,i}(s)$ is the frequency-domain form of $\Delta P_{e,i}(t)$ under the Laplace analysis.

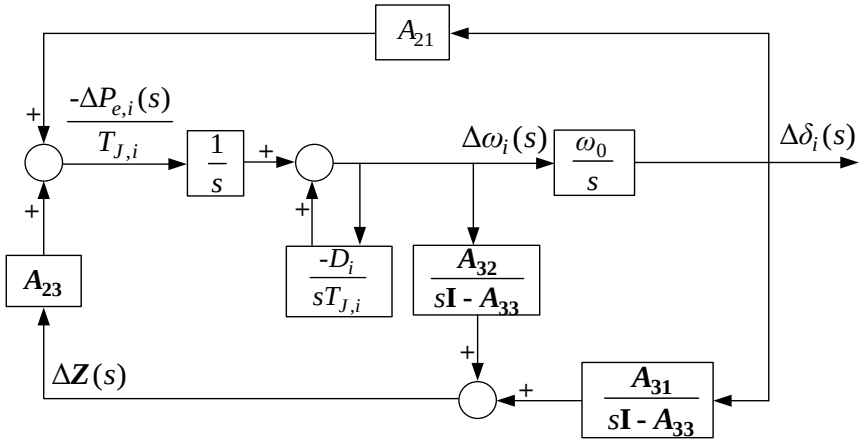

Fig. 3.1. Linearized representation of a multi-machine power system under the Laplace analysis.

Similar to the derivation in Chapter 2, (3.19)-(3.21) can be obtained, respectively.

$$\Delta\delta_i(s) = \frac{\omega_0}{s}\Delta\omega_i(s) \tag{3.19}$$

$$\Delta\omega_i(s) = \frac{1}{s}\left(A_{21}\Delta\delta_i(s) + \boldsymbol{A_{23}}\Delta\boldsymbol{Z}(s)\right) \tag{3.20}$$

$$\Delta\boldsymbol{Z}(s) = \frac{\boldsymbol{A_{31}}}{s\mathbf{I} - \boldsymbol{A_{33}}}\Delta\delta_i(s) + \frac{\boldsymbol{A_{32}}}{s\mathbf{I} - \boldsymbol{A_{33}}}\Delta\omega_i(s) \tag{3.21}$$

Substitute (3.19) into (3.20), and (3.22) can be obtained.

$$\left(s - A_{21}\frac{\omega_0}{s}\right)\Delta\omega_i(s) = \boldsymbol{A_{23}}\Delta\boldsymbol{Z}(s) \tag{3.22}$$

Substitute (3.19) into (3.21), and (3.23) can be obtained.

$$\Delta\boldsymbol{Z}(s) = \left(\frac{\boldsymbol{A_{31}}}{s\mathbf{I} - \boldsymbol{A_{33}}}\frac{\omega_0}{s} + \frac{\boldsymbol{A_{32}}}{s\mathbf{I} - \boldsymbol{A_{33}}}\right)\Delta\omega_i(s) \tag{3.23}$$

Substitute (3.23) into (3.22), and (3.24) can be obtained.

$$s=\left(A_{21}+\boldsymbol{A}_{23}\frac{\boldsymbol{A}_{31}}{s\mathbf{I}-\boldsymbol{A}_{33}}\right)\frac{\omega_0}{s}+\left(\boldsymbol{A}_{23}\frac{\boldsymbol{A}_{32}}{s\mathbf{I}-\boldsymbol{A}_{33}}\right) \tag{3.24}$$

Eq. (3.24) shares the same eigenvalue solutions with (3.18) as no information is missing. According to Fig. 3.1, (3.25) can be derived.

$$\Delta P_{e,i}(s)=-T_{J,i}\left(A_{21}\Delta\delta_i(s)+\boldsymbol{A}_{23}\Delta\boldsymbol{Z}(s)\right) \tag{3.25}$$

Eliminate $\Delta\delta_i(s)$ and $\Delta\boldsymbol{Z}(s)$ in (3.25) using (3.19) and (3.23), and then (3.26) can be derived.

$$-\frac{\Delta P_{e,i}(s)}{T_{J,i}\Delta\omega_i(s)}=\left(A_{21}+\boldsymbol{A}_{23}\frac{\boldsymbol{A}_{31}}{s\mathbf{I}-\boldsymbol{A}_{33}}\right)\frac{\omega_0}{s}+\left(\boldsymbol{A}_{23}\frac{\boldsymbol{A}_{32}}{s\mathbf{I}-\boldsymbol{A}_{33}}\right) \tag{3.26}$$

For an electromechanical oscillation mode λ_d, the variable s in (3.24) and (3.26) is replaced by λ_d. By substituting (3.26) into (3.24), (3.27) can be obtained.

$$-\frac{\Delta P_{e,i}(\lambda_d)}{T_{J,i}\Delta\omega_i(\lambda_d)}=\lambda_d \tag{3.27}$$

where $\Delta P_{e,i}(\lambda_d)$ is $\Delta P_{e,i}(s)$ with respect to $s=\lambda_d$; and $\Delta\omega_i(\lambda_d)$ is $\Delta\omega_i(s)$ with respect to $s=\lambda_d$.

In fact, $\Delta P_{e,i}(\lambda_d)$ and $\Delta\omega_i(\lambda_d)$ are actually $\Delta P_{e,i}(w_d \mid \sigma_d)$ and $\Delta\omega_i(w_d \mid \sigma_d)$ based on the discussion in Section 3.3. Substitute (3.27) into (3.17), and (3.28) can be obtained.

$$K_{d,i}^{\lambda_d}=\mathrm{Re}\left(-T_{J,i}\lambda_d\right) \tag{3.28}$$

It can be seen from (3.28) that the proposed EFA is always equivalent to MA for the arbitrary models of synchronous generators in the multi-machine power system, which is summarized as a new **Theorem 3.1** below, where $\boldsymbol{\Lambda}$ is the set of system eigenvalues associated with the i-th generator of a multi-machine power system; λ is an arbitrary

pair of complex numbers; x is the real part of λ; y is the imaginary part of λ ($y\neq0$); and $K_{d,i}^{\lambda}$ is the mode-screened damping torque coefficient of the i-th generator with respect to λ.

Theorem 3.1. *Λ is the set of system eigenvalues associated with the i-th generator of a multi-machine power system.* $\mathrm{Re}(\lambda)=-\frac{K_{d,i}^{\lambda}}{T_{J,i}}$ *holds if a pair of complex numbers* $\lambda=x\pm\mathrm{j}y$ ($y\neq0$) $\in \Lambda$.

The proposed **Theorem 3.1** implies the consistency between the proposed EFA and MA, which hence can provide a clear explanation on the quantitative analysis of the electromechanical oscillation. Interestingly, the new concept proposed in Section 3.2 (i.e., eq. (3.10)) is connected with the real part of the eigenvalue without considering the reactive power, which is one of the highlights and main findings of this chapter. Compared with the work in the literature, the proposed **Theorem 3.1** is a general conclusion for arbitrary types and parameters of synchronous generators and power networks in the multi-machine power system. Even if the structure and parameters of the power network are unknown, the proposed **Theorem 3.1** can be used to quantitatively estimate the damping performance.

3.5 Application Procedure of the Proposed Energy Flow Analysis

In Section 3.4, it is proved that the proposed EFA and MA are consistent, and the proposed mode-screened damping torque coefficient is connected with the eigenvalue, which provides the potential for the application of the proposed EFA in quantitatively estimating the damping performance of system oscillations.

For an unfamiliar power network or a complex system, the frequency of dominant electromechanical oscillation modes can be directly and conveniently observed from the Fourier analysis of the measurements at the terminal of a local generator. In other words, the frequency of the interested electromechanical oscillation mode is not required to be known by the system operators in advance. The variable y in the proposed **Theorem 3.1** can be directly replaced by the angular frequency of an interested electromechanical oscillation mode. Then, the damping performance with respect to the interested electromechanical oscillation mode can be quantitatively investigated by searching the variable x to meet the requirement in the proposed **Theorem 3.1**.

According to the discussions in Section 3.2 and 3.3, the calculation of $K_{d,i}^{\lambda}$ with respect to an arbitrary pair of complex numbers $\lambda=x\pm jy$ ($y\neq 0$) can be conducted by two options below.

Option (1): Refer to the discussion in Section 3.2. $\Delta P_{e,i}(t)$ and $\Delta\omega_i(t)$ are reconstructed as $\Delta P_{e,i}(t\,|\,x)$ and $\Delta\omega_i(t\,|\,x)$ with respect to x. Then, $\Delta P_{e,i}^{y}(t\,|\,x)$ and $\Delta\omega_i^{y}(t\,|\,x)$ are decomposed from $\Delta P_{e,i}(t\,|\,x)$ and $\Delta\omega_i(t\,|\,x)$ with respect to y. After that, the decomposed sub-signals $\Delta P_{e,i}^{y}(t\,|\,x)$ and $\Delta\omega_i^{y}(t\,|\,x)$ are substituted into (3.10) to compute the value of K_{di}^{λ}.

Option (2): Refer to the discussion in Section 3.3. $\Delta P_{e,i}(t)$ and $\Delta\omega_i(t)$ are reconstructed as $\Delta P_{e,i}(t\,|\,x)$ and $\Delta\omega_i(t\,|\,x)$ with respect to x. Then, $\Delta P_{e,i}(w\,|\,x)$ and $\Delta\omega_i(w\,|\,x)$ are obtained from the Fourier analysis of $\Delta P_{e,i}(t\,|\,x)$ and $\Delta\omega_i(t\,|\,x)$. After that, $\Delta P_{e,i}(y\,|\,x)$ and $\Delta\omega_i(y\,|\,x)$ with respect to y are substituted into (3.17) to compute the value of $K_{d,i}^{\lambda}$.

It should be noted that option (1) is in the time domain while option (2) is in the frequency domain, and $K_{d,i}^{\lambda}$ can be calculated from either option.

Based on the discussion above, the real part of the eigenvalue can be estimated by searching *x*, and the steps are illustrated in Fig. 3.2. The original *x* can be set as 0.

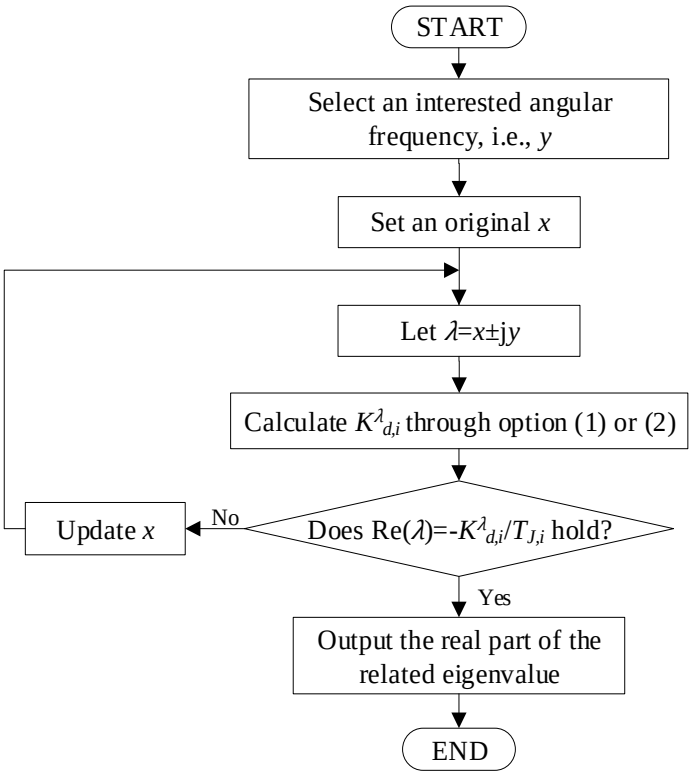

Fig. 3.2. Procedure flowchart of searching real part of eigenvalue.

3.6 Case Studies

The accuracy of the proposed EFA is verified in a 4M2A power system in Subsection 3.6.1, and the application of the proposed EFA in quantitatively investigating the electromechanical oscillations is demonstrated in a 16-machine 5-area (16M5A) power system in Subsection 3.6.2. Finally, a case of a real large-scale power system is further discussed in Subsection 3.6.3.

3.6.1 Verification in a 4-machine 2-area Power System with a Single Measurement

Since the aim of this subsection is to verify the accuracy of the proposed EFA, an interested eigenvalue of the 4M2A power system is selected to illustrate the calculation of the mode-screened damping torque coefficient via both TDI and FDI of the proposed EFA, which has been summarized in Section 3.5.

The line diagram of the 4M2A power system has been given by Fig. 2.5, which is not repeated here. The base capacity of the 4M2A power system is 100 MVA. The four generators are all equipped with AVR and PSS, and the terminal of G_1 is set as the single measurement location.

In order to verify the consistency between the proposed EFA and MA, the 6th-order model is adopted for all four generators in this study, as given by (A.1) in the Appendix A.1. It should be emphasized that the **Definition 3.1** proposed in Section 3.2 and the **Theorem 3.1** proposed in Section 3.4 are not limited to the 6th-order model of the synchronous generator. The parameters of generators are listed in the Appendix A.2. It is assumed that a step-up disturbance occurs to G_1 at 0.5 s and its mechanical power becomes 1.05 times of the original value, lasting for 0.05 s.

$P_{e,1}(t)$ and $\omega_1(t)$ at the terminal of G_1 are recorded for 100 s. Then, the deviations of $P_{e,1}(t)$ and $\omega_1(t)$ from the steady-state values are calculated, i.e., $\Delta P_{e,1}(t)$ and $\Delta\omega_1(t)$. The amplitude-frequency characteristic of $\Delta P_{e,1}(t)$ is analyzed to identify the frequency of dominant electromechanical oscillation modes. The plot of $\Delta P_{e,1}(t)$ is given in Fig. 3.3 (a), and the amplitude-frequency characteristic of $\Delta P_{e,1}(t)$ is given in Fig. 3.3 (b).

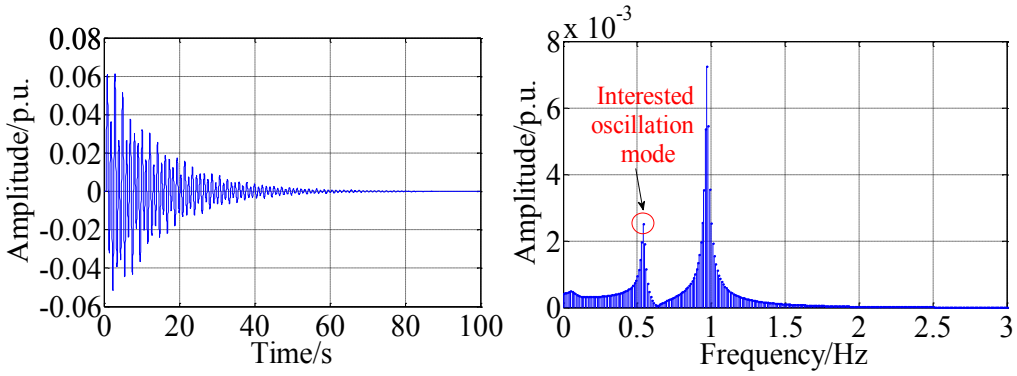

(a) (b)

Fig. 3.3. $\Delta P_{e,1}(t)$ and its amplitude-frequency characteristic in a 4M2A power system. (a). Plot of $\Delta P_{e,1}(t)$ in time domain. (b). Amplitude-frequency characteristic of $\Delta P_{e,1}(t)$ in frequency domain.

Fig. 3.3 (b) shows that G_1 is majorly associated with two electromechanical oscillation modes at around 0.54 Hz and 0.97 Hz. The oscillation mode at around 0.54 Hz is an inter-area oscillation mode, which is selected as the concerned one in this study. Then, the eigenvalue with respect to 0.54 Hz is also calculated from the state matrix of this 4M2A power system, i.e., -0.0820±j3.3977, for the verification purpose.

Since (3.24) is a key step to derive the connection between the proposed EFA and MA in Section 3.4, the correctness of (3.24) is firstly verified in this 4M2A power system. Substitute s=-0.0820±j3.3977 into the right part of (3.24) and the result is -0.0820±j3.3977. It can be found that (3.24) holds when a pair of complex numbers is equal to the related eigenvalue.

Let x=-0.0820 and y=3.3977. According to the discussion in Section 3.5, the mode-screened damping torque coefficient with respect to $\lambda=x\pm jy$=-0.0820±j3.3977 at G_1 (i.e., $K_{d,1}^{\lambda}$) is calculated from (3.10) and (3.17), respectively.

After $K_{d,1}^{\lambda}$ is calculated, the consistency between Re(λ) and $-K_{d,1}^{\lambda}/T_{J,1}$ is verified. The results are listed in Table 3.1. It can be demonstrated that the numerical calculations

from the proposed EFA show a high accuracy.

Table 3.1 Accuracy verification of the proposed EFA at G_1 in a 4M2A power system.

Concerned frequency	Re(λ)	$-K_{d,1}^{\lambda}/T_{J,1}$ ($K_{d,1}^{\lambda}$ is from (3.10))	$-K_{d,1}^{\lambda}/T_{J,1}$ ($K_{d,1}^{\lambda}$ is from (3.17))
0.54 Hz	-0.0820	-0.0832	-0.0821

Apart from this, as one of the most important conclusions in this chapter, the correctness of the proposed **Theorem 3.1** is further verified in the 4M2A power system. The arbitrary pair of complex numbers $x\pm jy$ is generated as λ for the calculation of $-K_{d,1}^{\lambda}/T_{J,1}$, which is repeated for 1000 times. The results are plotted in Fig. 3.4, where the x-axis is the real part of the complex number (i.e., x), the y-axis is the imaginary part of the complex number (i.e., y), and the z-axis is the result calculated from $-K_{d,1}^{\lambda}/T_{J,1}$. The blue circles are the results from $-K_{d,1}^{\lambda}/T_{J,1}$ by the arbitrary pairs of complex numbers, and the red dot is the result from $-K_{d,1}^{\lambda}/T_{J,1}$ by the related eigenvalue (i.e., -0.0820±j3.3977). The coordinate of the red dot is (-0.0820, 3.3977, -0.0821). It is seen from the partially enlarged drawing that the x-coordinate is closest to the z-coordinate for the red dot. In other words, only the red dot makes the transcendental equation in the proposed **Theorem 3.1** hold, which further demonstrates the correctness of the proposed **Theorem 3.1**.

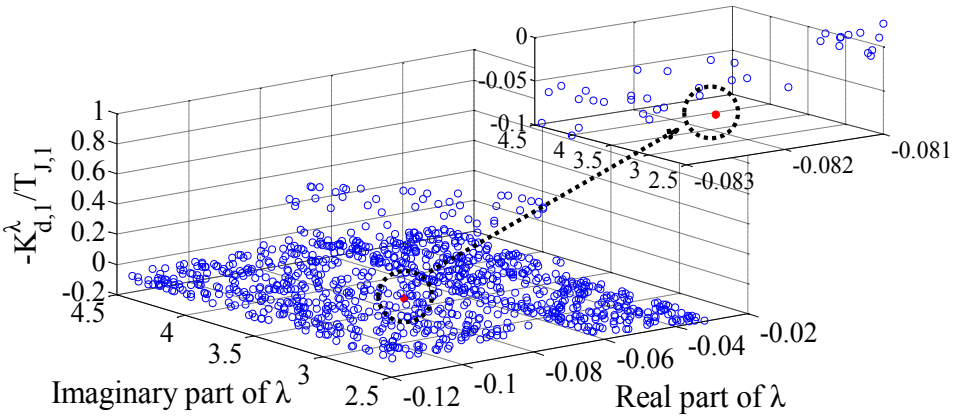

Fig. 3.4. Verification of the proposed **Theorem 3.1** in a 4M2A power system.

More discussions on the above results are highlighted as follows: (1) it is known from Table 3.1 that the proposed EFA can be implemented in both the time and frequency domain; (2) Eq. (3.24) is valid when the variable *s* is a related eigenvalue; and (3) Fig. 3.4 reveals that the proposed **Theorem 3.1** is valid only when a pair of complex numbers $x \pm jy$ are the related eigenvalues of the multi-machine power system.

3.6.2 Application in a 16-machine 5-area Power System with Multiple Measurements

The application of the proposed EFA with multiple measurements at different generators is demonstrated in a 16M5A power system. The line diagram of the 16M5A power system is illustrated in Fig. 3.5. The generators are all equipped with AVR but no PSS. The base capacity of this 16M5A power system is 100 MVA. The parameters of generators are listed in the Appendix A.2, which is cited from [117]. The terminals of the 16 generators are the potential measurement locations. A step-up disturbance happens to G_1 at 0.2 s and its mechanical power becomes 1.05 times of the original value, lasting for 0.1 s.

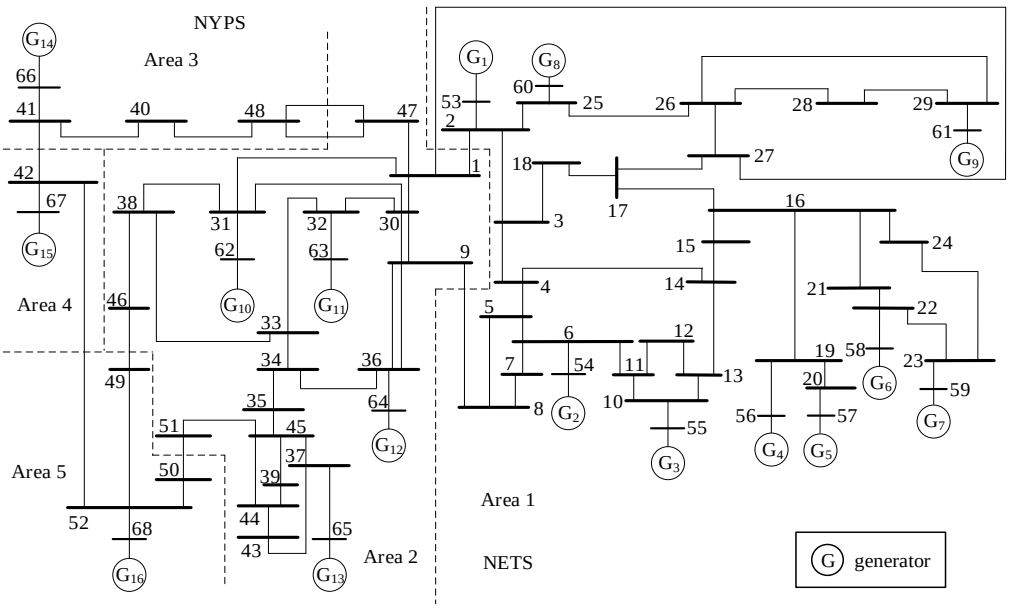

Fig. 3.5. Line diagram of a 16M5A power system.

$\Delta P_{e,1}(t)$ and its amplitude-frequency characteristic are given in Fig. 3.6. $\Delta P_{e,10}(t)$ and its amplitude-frequency characteristic are given in Fig. 3.7. It can be observed from Fig. 3.6 (b) that G_1 is majorly associated with two electromechanical oscillation modes at around 1.39 Hz and 1.44 Hz. Fig. 3.7 (b) further indicates that G_{10} is also associated with the same two oscillation modes as G_1. The damping performances with respect to 1.39 Hz and 1.44 Hz are hence further quantitatively investigated at both G_1 and G_{10}, respectively.

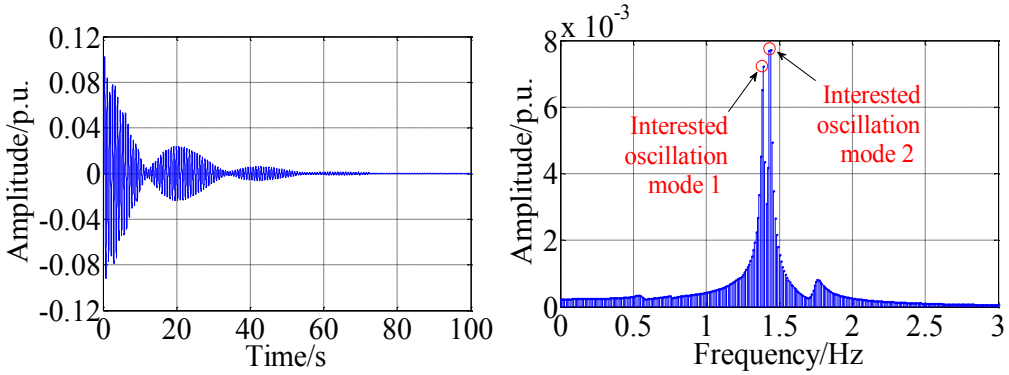

(a) (b)

Fig. 3.6. $\Delta P_{e,1}(t)$ and its amplitude-frequency characteristic in a 16M5A power system. (a). Plot of $\Delta P_{e,1}(t)$ in time domain. (b). Amplitude-frequency characteristic of $\Delta P_{e,1}(t)$ in frequency domain.

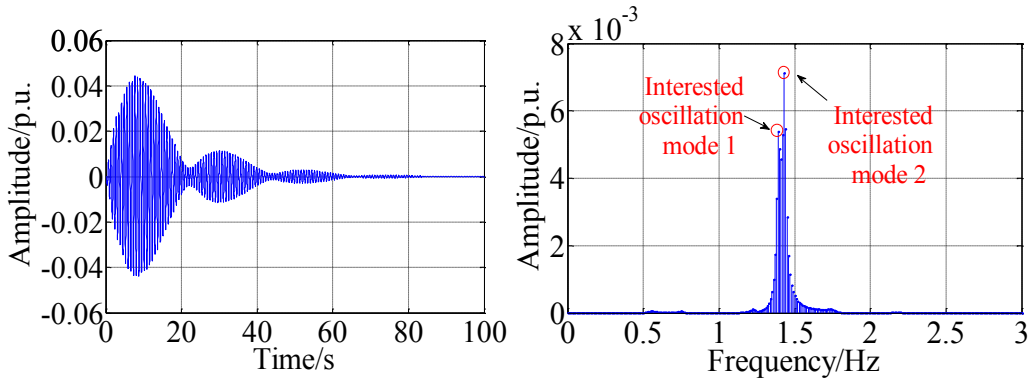

(a) (b)

Fig. 3.7. $\Delta P_{e,10}(t)$ and its amplitude-frequency characteristic in a 16M5A power system. (a). Plot of $\Delta P_{e,10}(t)$ in time domain. (b). Amplitude-frequency characteristic of $\Delta P_{e,10}(t)$ in frequency domain.

When the model of a multi-machine power system is of a high dimension, the proposed EFA demonstrates a clear merit to quantitatively investigate the damping performance of an interested electromechanical oscillation mode, since no complex modelling process is required. As mentioned above, the frequency of dominant electromechanical oscillation modes can be directly observed from the amplitude-frequency characteristic of the measurements. Then, using the steps displayed in Fig. 3.2, the real parts of related eigenvalues are investigated by searching x at the two-dimension plane of $y=2\pi\times1.39=8.7336$ and $y=2\pi\times1.44=9.0478$. The results are given by Fig. 3.8.

It is noted that the horizontal axis of Fig. 3.8 represents the variable x in Fig. 3.2. The task of Fig. 3.8 is to continuously update the value of x to find its value that makes the equation in the proposed **Theorem 3.1** hold. As mentioned in Section V, the original x can be set as 0. The blue curve in Fig. 3.8 is the trajectory of numerical results by continuously updating x from 0 to -0.1, and the crossover point with the red line is the value of x that makes the transcendental equation in the proposed **Theorem 3.1** hold.

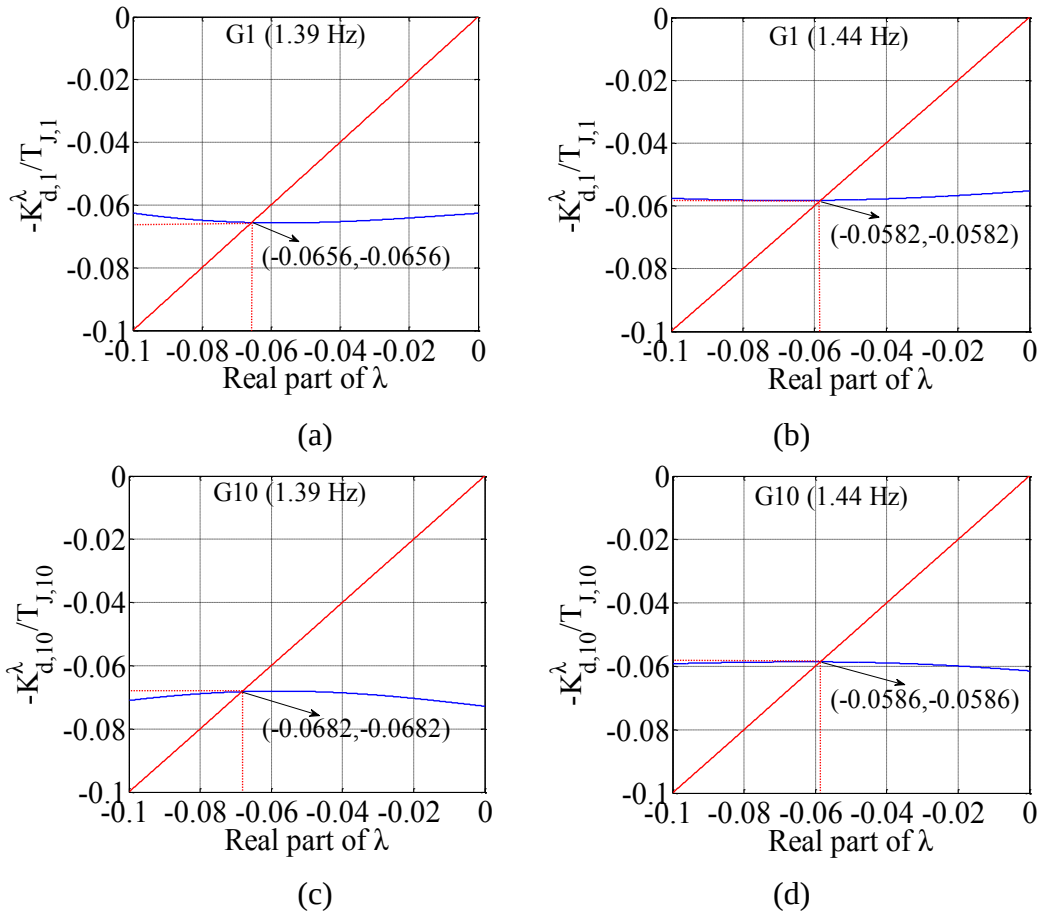

Fig. 3.8. Searching real parts of eigenvalues at G_1 and G_{10} in a 16M5A power system. (a). At G_1 with respect to 1.39 Hz. (b). At G_1 with respect to 1.44 Hz. (c). At G_{10} with respect to 1.39 Hz. (d). At G_{10} with respect to 1.44 Hz.

It should be emphasized here that the searching process of *x* can be actually stopped at the crossover point of the blue curve and red line, while Fig. 3.8 displays a complete process from 0 to -0.1 for a better understanding. For the electromechanical oscillation mode of 1.39 Hz, the real part of the eigenvalue obtained by the proposed method in Fig. 3.2 is -0.0656 at G_1 and -0.0682 at G_{10}. For the electromechanical oscillation mode of 1.44 Hz, the real part of the eigenvalue obtained by the proposed method in Fig. 3.2 is -0.0582 at G_1 and -0.0586 at G_{10}. As a verification, the real eigenvalue of the oscillation mode of 1.39 Hz is given as -0.0668±j8.7220, and the real eigenvalue of the oscillation mode of 1.44 Hz is given as -0.0585±j9.0094. It can be concluded that the

estimated real parts of the eigenvalues are roughly consistent at G_1 and G_{10}. Therefore, the investigation on the real part of the eigenvalue can be done at any generator involved in the interested electromechanical oscillation mode. In addition, Fig. 3.8 also proves that the different electromechanical oscillation modes with similar frequency can be identified accurately via the proposed EFA.

Next, whether the real part of the eigenvalue with respect to an electromechanical oscillation mode can be identified using the proposed procedure in Fig. 3.2 at those generators that are not strongly associated with the mode is verified. The electromechanical oscillation mode of 1.39 Hz is used as an example, and the results are given by Table 3.2. G_1 and G_{10} are strongly associated with this oscillation mode, while G_3 and G_8 are not strongly associated. It can be seen from Table 3.2 that the real part of the eigenvalue with respect to this electromechanical oscillation mode can be identified at G_3 and G_8 that are not strongly associated.

Table 3.2 Estimated real part of eigenvalue of electromechanical oscillation mode of 1.39 Hz by the proposed EFA at multiple generators in a 16M5A power system.

Concerned frequency	Estimated result at G_1	Estimated result at G_{10}	Estimated result at G_3	Estimated result at G_8
1.39 Hz	-0.0656	-0.0682	-0.0690	-0.0653

The damping ratios of multiple concerned electromechanical oscillation modes are estimated to further verify the accuracy of the proposed procedure in Fig. 3.2. The results are shown in Table 3.3. The acceptable range of the absolute error of the damping ratio (%) can be set at ±0.1% in practice. It can be seen from Table 3.3 that the absolute error between the estimated damping ratio by the proposed EFA and the

real damping ratio is within the range ±0.02%. The proposed EFA demonstrates a feasibility for quantitatively investigating the electromechanical oscillation at multiple generators in a multi-machine power system.

Table 3.3 Comparison of estimated damping ratios by the proposed EFA with real damping ratios in a 16M5A power system.

Concerned frequency	Real damping ratio	Estimated damping ratio
0.55 Hz	4.60 %	4.62 %
0.66 Hz	1.89 %	1.90 %
0.75 Hz	1.59 %	1.60 %
0.86 Hz	0.99 %	0.99 %
1.23 Hz	1.32 %	1.33 %
1.39 Hz	0.77 %	0.75 %
1.44 Hz	0.65 %	0.64 %

More discussions on the obtained results are highlighted as follows: (1) Fig. 3.8 illustrates that the real parts of eigenvalues of multiple electromechanical oscillation modes with similar frequency can be accurately identified by the proposed EFA; (2) Table 3.2 shows that the proposed EFA can be applied for quantitatively investigating the damping feature of the electromechanical oscillation mode that is not strongly associated with the measured generator; and (3) Table 3.3 illustrates that the error of the estimated damping ratio is within the acceptable range.

3.6.3 A Case of a Real Large-scale Power System

In this subsection, a case is further discussed in a real large-scale power system with multiple measurements. The configuration of this real provincial power grid at the East China is given in Fig. 3.9 [118]. There are 53 generators and 1713 buses. The voltage level of the transmission network is 500 kV and 220 kV. The abbreviations in Fig. 3.9 represent different regions of this power grid. It is assumed that the parameters and

structures of the power network as well as generators are unknown.

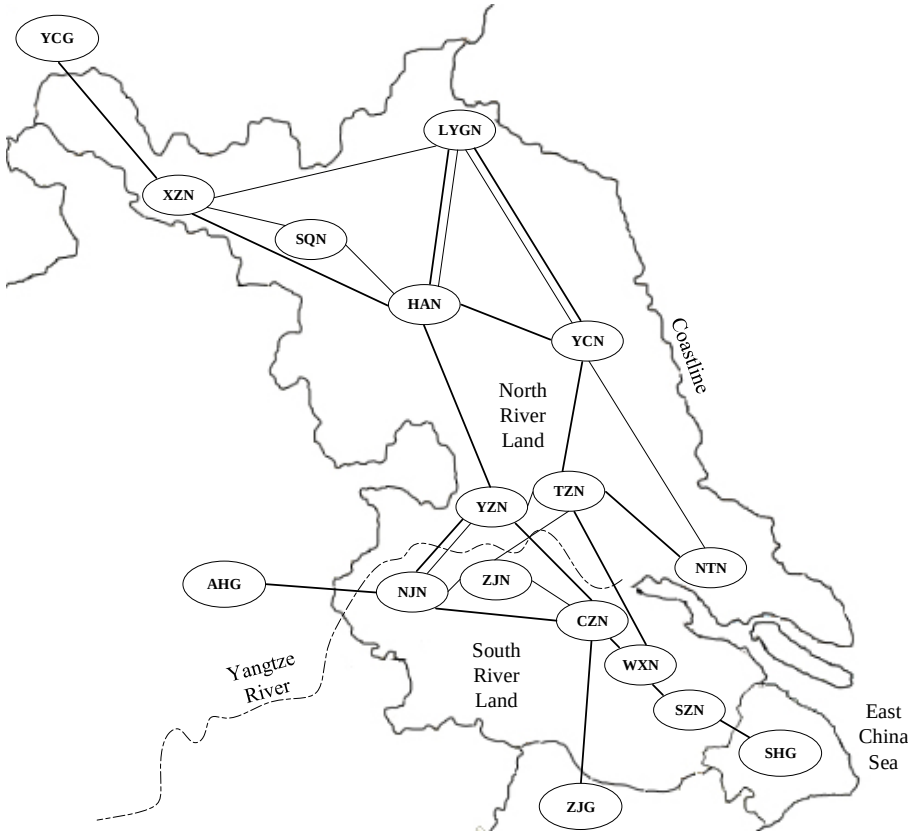

Fig. 3.9. Configuration of a real large-scale power system in East China.

The application of the proposed EFA in estimating the damping performance with respect to an electromechanical oscillation mode has been demonstrated in Subsection 3.6.2 in details, which would not be repeated here. In this subsection, two electromechanical oscillation modes are investigated by the proposed procedure in Section 3.5, and the results are given by Table 3.4.

Table 3.4 Validation of estimated damping ratios by the proposed EFA in a real large-scale power system.

Concerned frequency	Real damping ratio	Estimated damping ratio
0.35 Hz	1.94 %	1.88 %
0.73 Hz	6.36 %	6.44 %

The above two electromechanical oscillation modes are two most concerned inter-

area oscillation modes identified by the provincial system operators. It can be seen from Table 3.4 that the assessment error in this large-scale power system is larger than that in the 16M5A power system, but still acceptable.

When the specific structures and parameters of the power network and generators are unknown in a large-scale power system, MA becomes incapable. However, the proposed EFA in this chapter can link with the eigenvalues for the arbitrary types and parameters of generators and power networks.

3.7 Summary

Some key findings of this chapter are summarized as follows: (1) the mode-screened damping torque coefficient can be calculated in both the time and frequency domain based on the proposed EFA; (2) compared with the research in Chapter 2, the proposed EFA is strictly proved to be equivalent to MA regardless of the specific model of the generator in the multi-machine power system, and it is also interesting to see that this equivalence does not consider the reactive power items of the oscillatory energy flow; (3) the mode-screened damping torque coefficient with respect to an electromechanical oscillation mode is proportional to the real part of the eigenvalue with respect to this oscillation mode; (4) the damping performance of different electromechanical oscillation modes with similar frequency can be identified accurately by the proposed EFA; (5) the proposed EFA is proved to have a high accuracy for quantitatively investigating the damping ratio; (6) the proposed EFA provides the consistent results at multiple generators involved in the same electromechanical

oscillation mode; and (7) the damping ratio can be accurately estimated at the generators that are not strongly associated with the oscillation mode.

Chapter 4

Application of Energy Flow Analysis in Investigating Machine-side Oscillations of Full Converter-based Wind Generation Systems

4.1 Overview

The MSOs of FCWG systems is the critical threat to the reliable wind power supply. The introduction of ARC to the MSC controls of FCWG can effectively improve the oscillatory stability of the PEC-penetrated power grid, but it would also complicate MSOs of FCWG. Thus, it is of great significance to study the damping feature of MSOs of FCWG. In Chapter 3, the quantitative investigation using EFA is limited to the electromechanical oscillations of conventional synchronous generators. In this chapter, the proposed EFA in Chapter 3 is extended and applied to quantitatively investigate MSOs of FCWG. Firstly, the configuration and machine-side control loops of FCWG are briefly introduced. Then, the proposed EFA is extended for quantitatively evaluating the damping feature of MSOs of FCWG in the time domain. After that, the consistency of the extended EFA with MA is proved and revealed, which is applicable for arbitrary control schemes of FCWG. Finally, the extended EFA is applied in numerically investigating multiple types of MSOs of FCWG in case studies.

4.2 Configuration and Machine-side Control Loops of Full Converter-based Wind Generation

The type configuration of FCWG is shown in Fig. 4.1. The main components of FCWG are as follows [119]: (1) a PMSG; (2) the MSC and its controllers; (3) the DC-link, the GSC and their controllers; and (4) the phase-locked loop (PLL), etc.

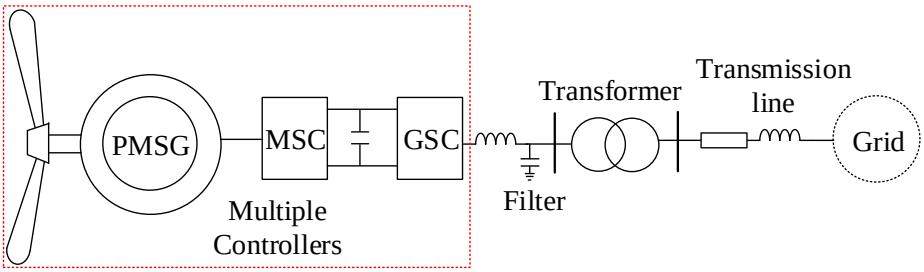

Fig. 4.1. Configuration of FCWG.

The PMSG is commonly known as the type-4 wind turbine generator [120], which is an emerging and promising technique in the wind power industry. Unlike the type-3 wind farm equipment, the PMSG and MSC are decoupled from the external grid by the DC capacitor. That is to say, the PMSG and MSC have no direct interaction with the external grid as the interaction is blocked by the DC capacitor [121][122].

Since this chapter focuses on MSO of FCWG, the machine-side control loops of FCWG are demonstrated in Fig. 4.2, $P_{pm,i}(s)$ is the mechanical power of the i-th PMSG; $P_{we,i}(s)$ is the electric power of the i-th PMSG; $H_{pr,i}$ is the inertia constant of the rotor of the i-th PMSG; $\omega_{pr,i}(s)$ is the angular frequency of the stator of the i-th PMSG; $\omega_{prref,i}(s)$ is the reference angular frequency of the stator of the i-th PMSG; $K_{p\text{-}wt,i}$ is the integral time constant in the control loop of the wind turbine of the i-th PMSG; $K_{pp\text{-}wt,i}$ is the proportional time constant in the control loop of the wind turbine of the i-th PMSG;

and $x_{p\text{-}wt,i}(s)$ is an intermediate variable in the control loop of the wind turbine of the *i*-th PMSG. Generally, there are 3 control loops on the machine side of FCWG, i.e., the wind turbine control loop, *d*-axis current control loop and *q*-axis current control loop. Since the discussion on the extended EFA and its consistency with MA should be general to any control schemes, the *d*-axis current control loop and *q*-axis current control loop are represented in a general manner in Fig. 4.2.

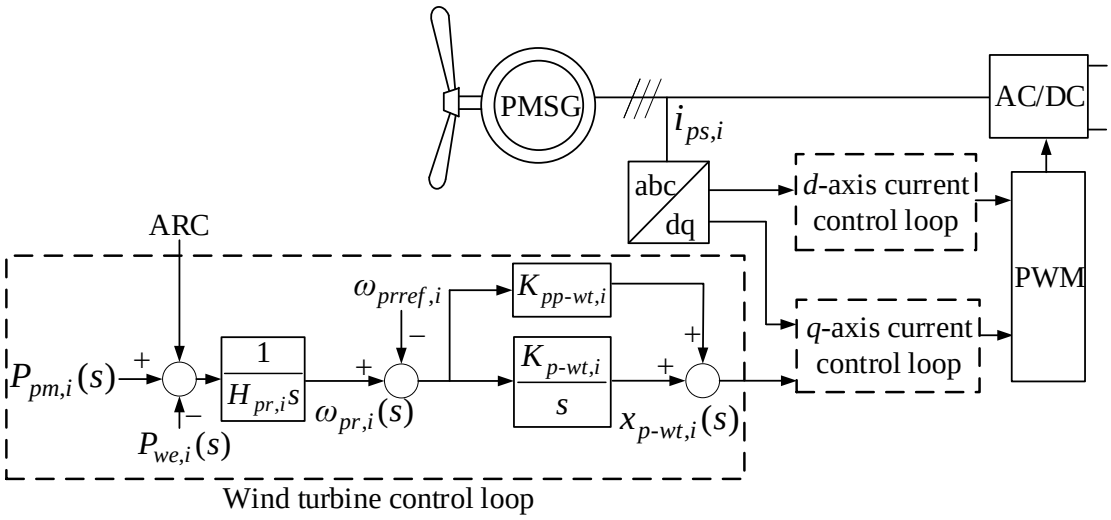

Fig. 4.2. Machine-side control loops of FCWG.

In the case studies of this chapter, a typical scheme of *d*-axis current control loop and *q*-axis current control loop is given in Fig. 4.3. The definition of variables in Fig. 4.3 can be found in [113], which are not repeated here.

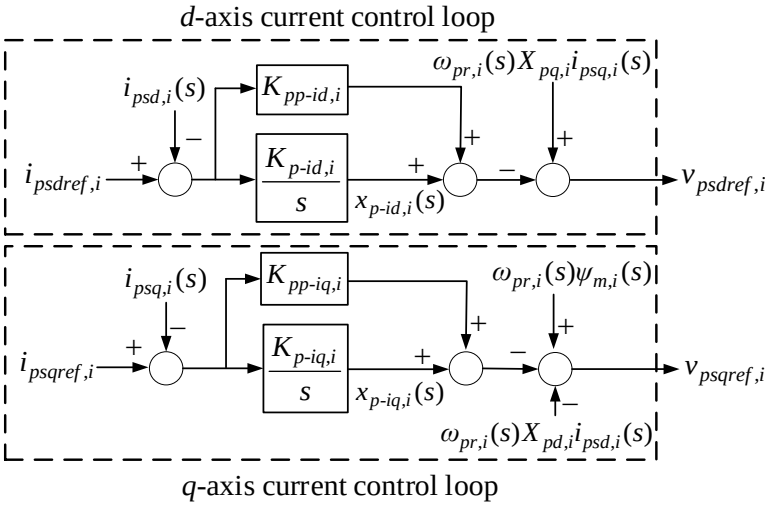

Fig. 4.3. A typical control scheme of MSC.

When there is no ARC, the machine-side dynamics are directly connected at the DC capacitor, which does not interact with the EGOs. That is to say, the inherent MSOs of FCWG are all independent without ARC, and their characteristics are determined by the machine-side structure as well as parameters of FCWG.

As discussed in Chapter 1, the rotor of PMSG can store energy and dynamics. If the FCWG is equipped with an ARC, the potential dynamic of PMSG can be utilized to improve the oscillatory stability of the PEC-penetrated power grid. On the other hand, when an ARC is installed, the EGOs will be introduced to the machine side of FCWG, which can complicate and aggravate MSOs of FCWG. Even the modal resonance between the inherent MSO and EGO can appear. Thus, the wind farm operator must pay more attention to them to ensure both the reliable wind power supply and the oscillatory stability.

The mechanism of ARC is to introduce the disturbance of the external grid to the MSC controls to adjust the power output of FCWG and further to suppress the

instability. The transfer function of ARC is given in Fig. 4.4, where $\Delta P_{ARC\text{-}wt,i}(s)$ is the output signal of ARC to the *i*-th PMSG; T_W is the time constant of the washout filter, K_W is the proportional gain, T_1, T_2, T_3 and T_4 are the time constants of the lead-lag filers, and $\Delta\theta_{pll,i}(s)$ is the input signal of ARC (i.e., the PLL angle variation of the *i*-th FCWG in the frequency domain). It can be seen that an ARC has four main parts: a washout filter, a proportional gain, and two lead-lag filters. The washout filter eliminates the DC component and select the signal with the appropriate frequency that is related to the disturbance of the external grid. The proportional gain adjusts the input signal to a proper magnitude. The two lead-lag filters adjust the compensation angle to a proper one.

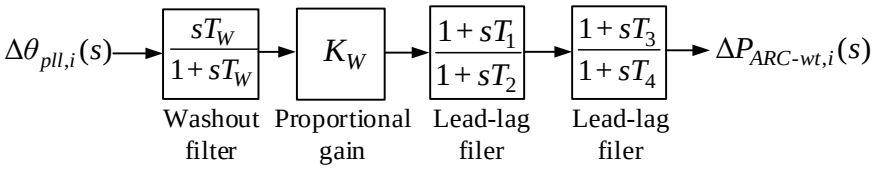

Fig. 4.4. Transfer function of ARC.

4.3 Extension of Energy Flow Analysis for Machine-side Oscillations of Full Converter-based Wind Generation

The typical configuration and machine-side control loops of FCWG have been given in Section 4.2. In this section, the proposed EFA in Chapter 3 is extended for MSOs of FCWG to quantitatively extract the damping feature of the interested MSOs.

According to the definition in Chapter 2 and 3, the energy can be represented as the integral of the product of torque and speed. Based on that, the dissipation of the oscillatory energy flow of the *i*-th PMSG can be calculated by (4.1).

$$W_{dp,i} = \int_0^{+\infty} \Delta T_{pe,i}(t)\Delta\omega_{pr,i}(t)\mathrm{d}t \tag{4.1}$$

where $W_{dp.i}$ is the dissipation of the oscillatory energy flow of the i-th PMSG; $\Delta\omega_{pr,i}(t)$ is the angular frequency deviation of the stator of the i-th PMSG; and $\Delta T_{pe,i}(t)$ is the electric torque imbalance of the i-th PMSG.

In this chapter, the electric torque imbalance of PMSG is defined and decomposed as two components, i.e., (4.2).

$$\Delta T_{pe,i}(t) = K_{pd,i}\Delta\omega_{pr,i}(t) + K_{ps,i}\Delta x_{p-wt,i}(t) \tag{4.2}$$

where $K_{pd,i}$ is the equivalent damping torque coefficient of the i-th PMSG; $K_{ps,i}$ is the equivalent synchronizing torque coefficient of the i-th PMSG; and $\Delta x_{p\text{-}wt,i}(t)$ is the deviation of the intermediate variable in the control loop of the wind turbine of the i-th PMSG in the time domain.

Substitute (4.2) into (4.1), and (4.3) can be further derived.

$$\begin{aligned} W_{dp,i} &= \int_0^{+\infty} K_{pd,i}\Delta\omega_{pr,i}^2(t)\mathrm{d}t + \int_0^{+\infty} K_{ps,i}\Delta x_{p-wt,i}(t)\Delta\omega_{pr,i}(t)\mathrm{d}t \\ &= \int_0^{+\infty} K_{pd,i}\Delta\omega_{pr,i}^2(t)\mathrm{d}t + \frac{1}{2}K_{ps,i}\left(\Delta x_{p-wt,i}^2(\infty) - \Delta x_{p-wt,i}^2(0)\right) \\ &= \int_0^{+\infty} K_{pd,i}\Delta\omega_{pr,i}^2(t)\mathrm{d}t \end{aligned} \tag{4.3}$$

The electric torque imbalance is considered to be approximately equal to the electric power deviation for the i-th PMSG. Thus, the equivalent damping torque coefficient of the i-th PMSG can be derived as (4.4) with/without ARC. It is noted that $\Delta P_{ARC\text{-}wt,i}(t)=0$ in the following two conditions: (1) there is no ARC; or (2) ARC is installed but it does not work since there is no disturbance on the external power grid.

$$K_{pd,i}=\frac{\int_0^{+\infty}\left(\Delta P_{we,i}(t)-\Delta P_{ARC-wt,i}(t)\right)\Delta\omega_{pr,i}(t)\mathrm{d}t}{\int_0^{+\infty}\Delta\omega_{pr,i}^2(t)\mathrm{d}t} \tag{4.4}$$

where $\Delta P_{we,i}(t)$ is the electric power deviation of the i-th PMSG in the time domain; and $\Delta P_{ARC\text{-}wt,i}(t)$ is the output signal of ARC to the i-th PMSG in the time domain.

For the machine side of FCWG, $K_{pd,i}$ obtained by (4.4) is coupled with multiple MSOs and some of them may be the non-inherent MSOs (i.e., EGOs) introduced by ARC. That is to say, $K_{pd,i}$ obtained by (4.4) cannot be effectively used to quantitatively indicate the damping feature of the interested MSO.

For an interested MSO $\lambda_m=\sigma_m\pm\mathrm{j}w_m$, the amplitude and phase angle at w_m can be observed from the plot of the amplitude-frequency spectrum and phase-frequency spectrum of the measurements of PMSG.

The pre-processing of measurements in Chapter 3 is applied to reconstruct $\Delta P_{ARC\text{-}wt,i}(t)$, $\Delta P_{we,i}(t)$ and $\Delta\omega_{pr,i}(t)$ as $\Delta P_{ARC\text{-}wt,i}(t \mid \sigma_m)$, $\Delta P_{we,i}(t \mid \sigma_m)$ and $\Delta\omega_{pr,i}(t \mid \sigma_m)$ with respect to $\sigma=\sigma_m$. After that, $\Delta P_{ARC\text{-}wt,i}(t \mid \sigma_m)$, $\Delta P_{we,i}(t \mid \sigma_m)$ and $\Delta\omega_{pr,i}(t \mid \sigma_m)$ is further decomposed as $\Delta P_{ARC\text{-}wt,i}^{w_m}(t \mid \sigma_m)$, $\Delta P_{we,i}^{w_m}(t \mid \sigma_m)$ and $\Delta\omega_{pr,i}^{w_m}(t \mid \sigma_m)$.

On this basis, the mode-screened damping torque coefficient of the i-th PMSG is given in (4.5).

$$K_{pd,i}^{\lambda_m}=\frac{\int_0^{+\infty}\left(\Delta P_{we,i}^{w_m}(t \mid \sigma_m)-\Delta P_{ARC-wt,i}^{w_m}(t \mid \sigma_m)\right)\Delta\omega_{pr,i}^{w_m}(t \mid \sigma_m)\mathrm{d}t}{\int_0^{+\infty}\left(\Delta\omega_{pr,i}^{w_m}(t \mid \sigma_m)\right)^2\mathrm{d}t} \tag{4.5}$$

where $K_{pd,i}^{\lambda_m}$ is the mode-screened damping torque coefficient of the i-th PMSG with respect to λ_m.

4.4 Modal Analysis for Machine-side Oscillations of Full Converter-based Wind Generation

In this section, MA is discussed for MSOs of FCWG. $\Delta\omega_{pr,i}(t)$ and $\Delta x_{p\text{-}wt,i}(t)$ are chosen as the two focused state variables. The natural damping of PMSG is ignored. According to Fig. 4.2, the focused equations of the *i*-th PMSG are given as (4.6) and (4.7).

$$\frac{\mathrm{d}\Delta\omega_{pr,i}(t)}{\mathrm{d}t}=\frac{1}{H_{pr,i}}\left(\Delta P_{ARC-wt,i}(t)-\Delta P_{we,i}(t)\right) \tag{4.6}$$

$$\frac{\mathrm{d}\Delta x_{p-wt,i}(t)}{\mathrm{d}t}=K_{p-wt,i}\Delta\omega_{pr,i}(t) \tag{4.7}$$

It is noted that $\Delta P_{ARC\text{-}wt,i}(t)=0$ in the following two conditions: (1) there is no ARC; or (2) ARC is installed but it does not work since there is no disturbance on the external power grid.

In order to represent the whole power system considering the arbitrary control schemes of FCWG in the multi-machine environment, the linearization of the whole power system is derived as (4.8).

$$\begin{bmatrix} s\Delta x_{p-wt,i}(s) \\ s\Delta\omega_{pr,i}(s) \\ s\Delta\boldsymbol{Z}(s) \end{bmatrix}=\begin{bmatrix} 0 & K_{p-wt,i} & \boldsymbol{0} \\ A_{21} & 0 & \boldsymbol{A_{23}} \\ \boldsymbol{A_{31}} & \boldsymbol{A_{32}} & \boldsymbol{A_{33}} \end{bmatrix}\begin{bmatrix} \Delta x_{p-wt,i}(s) \\ \Delta\omega_{pr,i}(s) \\ \Delta\boldsymbol{Z}(s) \end{bmatrix} \tag{4.8}$$

where $\Delta x_{p\text{-}wt,i}(s)$ is the frequency-domain form of $\Delta x_{p\text{-}wt,i}(t)$ under the Laplace analysis; $\Delta\omega_{pr,i}(s)$ is the frequency-domain form of $\Delta\omega_{pr,i}(t)$ under the Laplace analysis. Similar to Chapter 3, $\Delta\boldsymbol{Z}(s)$ includes the state variables of the *i*-th FCWG excluding $\Delta\omega_{pr,i}(s)$ and $\Delta x_{p\text{-}wt,i}(s)$, as well as all the state variables of other generating units. The meanings of other variables are the same with those in Chapter 2 and 3, which are not repeated here.

Based on (4.6)-(4.8), the linearized representation of the whole power system considering the arbitrary control schemes of FCWG in the multi-machine environment can be displayed in Fig. 4.5. It is noted here Fig. 4.5 is from the perspective of the machine side of FCWG.

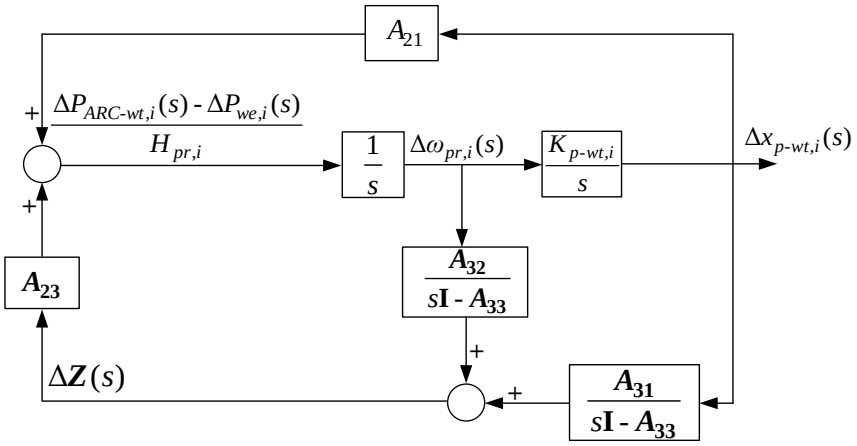

Fig. 4.5. Linearized representation of an FCWG-integrated power system under the Laplace analysis.

From Fig. 4.5, (4.9)-(4.11) can be obtained, respectively.

$$\Delta x_{p-wt,i}(s) = \frac{K_{p-wt,i}}{s}\Delta\omega_{pr,i}(s) \tag{4.9}$$

$$\Delta\omega_{pr,i}(s) = \frac{1}{s}\left(A_{21}\Delta x_{p-wt,i}(s) + \boldsymbol{A_{23}}\Delta\boldsymbol{Z}(s)\right) \tag{4.10}$$

$$\Delta\boldsymbol{Z}(s) = \frac{\boldsymbol{A_{31}}}{s\mathbf{I} - \boldsymbol{A_{33}}}\Delta x_{p-wt,i}(s) + \frac{\boldsymbol{A_{32}}}{s\mathbf{I} - \boldsymbol{A_{33}}}\Delta\omega_{pr,i}(s) \tag{4.11}$$

Substitute (4.9) into (4.10), and (4.12) can be obtained.

$$\left(s - A_{21}\frac{K_{p-wt,i}}{s}\right)\Delta\omega_{pr,i}(s) = \boldsymbol{A_{23}}\Delta\boldsymbol{Z}(s) \tag{4.12}$$

Substitute (4.9) into (4.11), and (4.13) can be obtained.

$$\Delta \boldsymbol{Z}(s) = \left(\frac{\boldsymbol{A_{31}}}{s\mathbf{I} - \boldsymbol{A_{33}}} \frac{K_{p-wt,i}}{s} + \frac{\boldsymbol{A_{32}}}{s\mathbf{I} - \boldsymbol{A_{33}}} \right) \Delta \omega_{pr,i}(s) \tag{4.13}$$

Substitute (4.13) into (4.12), and (4.14) can be obtained.

$$s = \left(A_{21} + \boldsymbol{A_{23}} \frac{\boldsymbol{A_{31}}}{s\mathbf{I} - \boldsymbol{A_{33}}} \right) \frac{K_{p-wt,i}}{s} + \left(\boldsymbol{A_{23}} \frac{\boldsymbol{A_{32}}}{s\mathbf{I} - \boldsymbol{A_{33}}} \right) \tag{4.14}$$

Eq. (4.13) is essentially equivalent to (4.8). According to Fig. 4.5, (4.15) can be also derived.

$$\Delta P_{ARC-wt,i}(s) - \Delta P_{we,i}(s) = H_{pr,i} \left(A_{21} \Delta x_{p-wt,i}(s) + \boldsymbol{A_{23}} \Delta \boldsymbol{Z}(s) \right) \tag{4.15}$$

Eliminate $\Delta x_{p\text{-}wt,i}(s)$ and $\Delta \boldsymbol{Z}(s)$ in (4.15) using (4.9) and (4.13), and then (4.16) can be derived.

$$\frac{\Delta P_{ARC-wt,i}(s) - \Delta P_{we,i}(s)}{H_{pr,i} \Delta \omega_{pr,i}(s)} = \left(A_{21} + \boldsymbol{A_{23}} \frac{\boldsymbol{A_{31}}}{s\mathbf{I} - \boldsymbol{A_{33}}} \right) \frac{K_{p-wt,i}}{s} + \left(\boldsymbol{A_{23}} \frac{\boldsymbol{A_{32}}}{s\mathbf{I} - \boldsymbol{A_{33}}} \right) \tag{4.16}$$

By comparing (4.14) with (4.16), it can be seen that (4.17) can be obtained for an MSO of FCWG.

$$\lambda_m = \frac{\Delta P_{ARC-wt,i}(\lambda_m) - \Delta P_{we,i}(\lambda_m)}{H_{pr,i} \Delta \omega_{pr,i}(\lambda_m)} \tag{4.17}$$

where λ_m is a pair of eigenvalues of an interested MSO of FCWG.

4.5 Consistency of Energy Flow Analysis with Modal Analysis for Machine-side Oscillations of Full Converter-based Wind Generation

In this section, the extended EFA and MA will be proved to be consistent for MSO of FCWG. Similarly, substitute $\Delta P_{ARC\text{-}wt,i}(t \mid \sigma_m)$, $\Delta P_{we,i}(t \mid \sigma_m)$ and $\Delta \omega_{pr,i}(t \mid \sigma_m)$ into the Parseval's Theorem, and then (4.18) and (4.19) can be obtained.

$$\begin{aligned}&\int_0^{+\infty}\left(\Delta P_{we,i}(t\,|\,\sigma_m)-\Delta P_{ARC-wt,i}(t\,|\,\sigma_m)\right)\Delta\omega_{pr,i}(t\,|\,\sigma_m)\mathrm{d}t\\&=\frac{1}{\pi}\int_0^{+\infty}\mathrm{Re}\left(\left(\Delta P_{we,i}(w\,|\,\sigma_m)-\Delta P_{ARC-wt,i}(w\,|\,\sigma_m)\right)\Delta\omega^{*}_{pr,i}(w\,|\,\sigma_m)\right)\mathrm{d}w\end{aligned}\tag{4.18}$$

$$\int_0^{+\infty}\Delta\omega^2_{pr,i}(t\,|\,\sigma_m)\mathrm{d}t=\frac{1}{\pi}\int_0^{+\infty}\mathrm{Re}\left(\Delta\omega_{pr,i}(w\,|\,\sigma_m)\Delta\omega^{*}_{pr,i}(w\,|\,\sigma_m)\right)\mathrm{d}w\tag{4.19}$$

where $\Delta P_{ARC\text{-}wt,i}(w\,|\,\sigma_m)$, $\Delta P_{we,i}(w\,|\,\sigma_m)$ and $\Delta\omega_{pr,i}(w\,|\,\sigma_m)$ are the frequency-domain forms of $\Delta P_{ARC\text{-}wt,i}(t\,|\,\sigma_m)$, $\Delta P_{we,i}(t\,|\,\sigma_m)$ and $\Delta\omega_{pr,i}(t\,|\,\sigma_m)$ under the Fourier analysis.

Then, (4.20) can be derived by applying (4.18) and (4.19).

$$\begin{aligned}&\frac{\int_0^{+\infty}\left(\Delta P_{we,i}(t\,|\,\sigma_m)-\Delta P_{ARC-wt,i}(t\,|\,\sigma_m)\right)\Delta\omega_{pr,i}(t\,|\,\sigma_m)\mathrm{d}t}{\int_0^{+\infty}\Delta\omega^2_{pr,i}(t\,|\,\sigma_d)\mathrm{d}t}\\&=\frac{\int_0^{+\infty}\mathrm{Re}\left(\left(\Delta P_{we,i}(w\,|\,\sigma_m)-\Delta P_{ARC-wt,i}(w\,|\,\sigma_m)\right)\Delta\omega^{*}_{pr,i}(w\,|\,\sigma_m)\right)\mathrm{d}w}{\int_0^{+\infty}\mathrm{Re}\left(\Delta\omega_{pr,i}(w\,|\,\sigma_m)\Delta\omega^{*}_{pr,i}(w\,|\,\sigma_m)\right)\mathrm{d}w}\end{aligned}\tag{4.20}$$

For an MSO $\lambda_m=\sigma_m\pm\mathrm{j}w_m$, since $\Delta P_{ARC\text{-}wt,i}(w_m\,|\,\sigma_m)$, $\Delta P_{we,i}(w_m\,|\,\sigma_m)$, $\Delta\omega_{pr,i}(w_m\,|\,\sigma_m)$ and $\Delta\omega^{*}_{pr,i}(w_m\,|\,\sigma_m)$ are the constant complex numbers, (4.5) is further equivalent to (4.21) on the basis of (4.20).

$$\begin{aligned}K^{\lambda_m}_{pd,i}&=\mathrm{Re}\left(\frac{\left(\Delta P_{we,i}(w_m\,|\,\sigma_m)-\Delta P_{ARC-wt,i}(w_m\,|\,\sigma_m)\right)\Delta\omega^{*}_{pr,i}(w_m\,|\,\sigma_m)}{\Delta\omega_{pr,i}(w_m\,|\,\sigma_m)\Delta\omega^{*}_{pr,i}(w_m\,|\,\sigma_m)}\right)\\&=\mathrm{Re}\left(\frac{\Delta P_{we,i}(w_m\,|\,\sigma_m)-\Delta P_{ARC-wt,i}(w_m\,|\,\sigma_m)}{\Delta\omega_{pr,i}(w_m\,|\,\sigma_m)}\right)\end{aligned}\tag{4.21}$$

By comparing (4.5) with (4.17) and (4.21), it can be seen that the proposed coefficient in (4.5) is always equivalent to the relevant eigenvalue, i.e., (4.22).

$$\mathrm{Re}\left(\lambda_m\right)=-\frac{K^{\lambda_m}_{pd,i}}{H_{pr,i}}\tag{4.22}$$

Eq. (4.22) is general for the arbitrary types of control schemes of FCWG, which can be applied for quantitatively investigating the interested MSOs of FCWG. Then, the

application of (4.22) for estimating the eigenvalue of an interested MSO of FCWG is given as the following steps. Only the pre-processing of measurements is needed, and the complex modeling of the FCWG-integrated power system can be avoided.

Step 1: Collect the measurements $\Delta P_{ARC\text{-}wt,i}(t)$, $\Delta P_{we,i}(t)$ and $\Delta\omega_{pr,i}(t)$ at the i-th PMSG in a period.

Step 2: Conduct the analysis of the amplitude-frequency characteristic of $\Delta P_{we,i}(t)$ (or $\Delta\omega_{pr,i}(t)$), from which the angular frequency of dominant MSOs can be observed, i.e., the imaginary parts of eigenvalues of dominant MSOs.

Step 3: Choose an interested MSO at the angular frequency w_m and give σ_m an initial value as σ_m=0.

Step 4: Calculate $K_{pd,i}^{\lambda_m}$.

Step 5: If abs $\left(-K_{pd,i}^{\lambda_m}/H_{pr,i}-\sigma_m\right)$ is smaller than an acceptable error e, go to Step 7; otherwise, go to Step 6.

Step 6: Update σ_m as $\sigma_m=\sigma_m\pm r$ and go to Step 4. It is noted that r/e should be smaller than 10^{-1}.

Step 7: Output the estimated eigenvalue of the interested MSO.

4.6 Case Studies

In this section, the extended EFA is firstly verified in an FCWG-integrated SMIB power system. Then, the extended EFA is applied to quantitatively investigated the damping feature of multiple types of MSOs of FCWG in an FCWG-integrated 4M2A power system.

4.6.1 Verification in a Single-machine Infinite-bus Power System with a Full Converter-based Wind Generation

The correctness of (4.22) is firstly verified in an FCWG-integrated SMIB power system. The line diagram of this FCWG-integrated SMIB power system is illustrated in Fig. 4.6. There is an FCWG installed at bus 2 with no ARC. The base capacity of this SMIB power system is 100 MVA. A step-up disturbance happens to PMSG at 0.2 s and its mechanical power becomes 1.1 times of the original value, which lasts for 0.1 s. There is no disturbance on the external grid. In this case study, PMSG and MSC are actually decoupled from the external grid. The parameters of FCWG and conventional synchronous generator are given in the Appendix A.3, which is cited from [113].

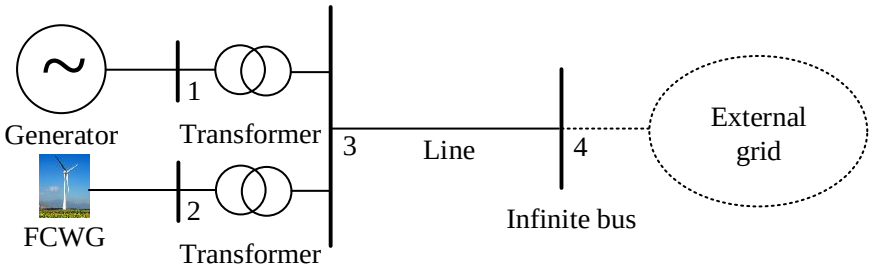

Fig. 4.6. Line diagram of an SMIB power system with an FCWG.

The plot of $\Delta P_{we,1}(t)$ and its amplitude-frequency characteristic are given in Fig. 4.7. Since the purpose of this case study is to verify the correctness of (4.22), the eigenvalue of an interested MSO is directly given, i.e., λ_m=-0.0883±j3.0530. Then, the calculation of $-K_{pd,i}^{\lambda_m}/H_{pr,1}$ is conducted, and the result is -0.0883 (i.e., $-K_{pd,i}^{\lambda_m}/H_{pr,1}$=-0.0883). It can be seen that (4.22) is valid.

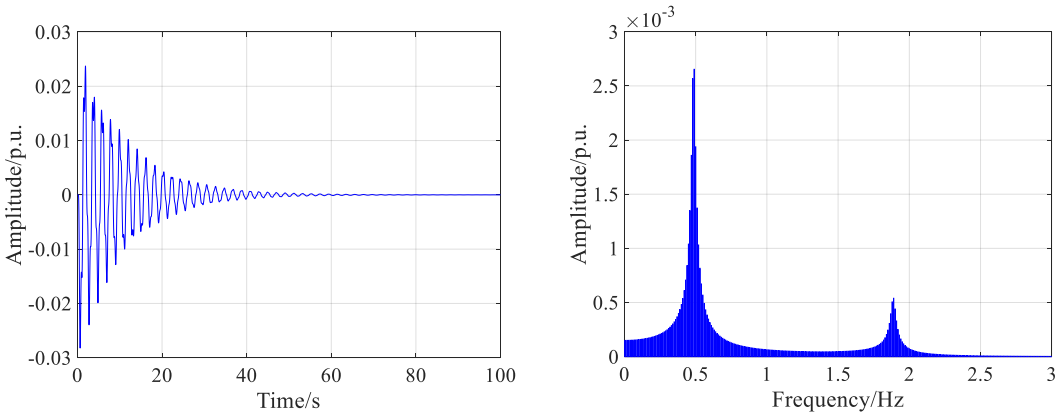

(a) (b)

Fig. 4.7. $\Delta P_{we,1}(t)$ and its amplitude-frequency characteristic in an FCWG-integrated SMIB power system. (a). Plot of $\Delta P_{we,1}(t)$ in time domain. (b). Amplitude-frequency characteristic of $\Delta P_{we,1}(t)$ in frequency domain.

The steps proposed at the end of Section 4.5 can be feasible, and the estimation of the interested eigenvalue using the proposed steps will be carried out in the next subsection.

4.6.2 Application in a 4-machine 2-area Power System with a Full Converter-based Wind Generation

The line diagram of an FCWG-integrated 4M2A power system is given by Fig. 4.8. There is an FCWG installed at bus 5 with the integration of an ARC. The base capacity of this power system is 100 MVA. The parameters of FCWG and conventional synchronous generators are given in the Appendix A.3, which is cited from [113].

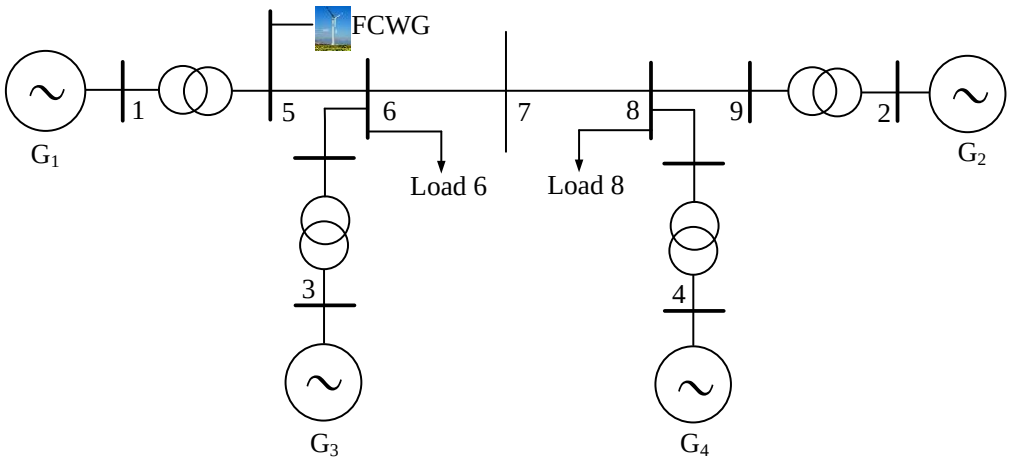

Fig. 4.8. Line diagram of a 4M2A power system with an FCWG.

(1) Scenario 4.1 (PMSG disturbance)

In Scenario 4.1, there is no disturbance on the external power grid, but a disturbance occurs to the mechanical power of PMSG at 0.2 s and its value becomes 1.05 of the original one, which lasts for 0.1 s.

The plot of $\Delta P_{we,1}(t)$ and its amplitude-frequency characteristic are given in Fig. 4.9. It can be seen that there are two inherent MSOs excited at 0.41 Hz and 1.54 Hz, which are selected as the interested ones.

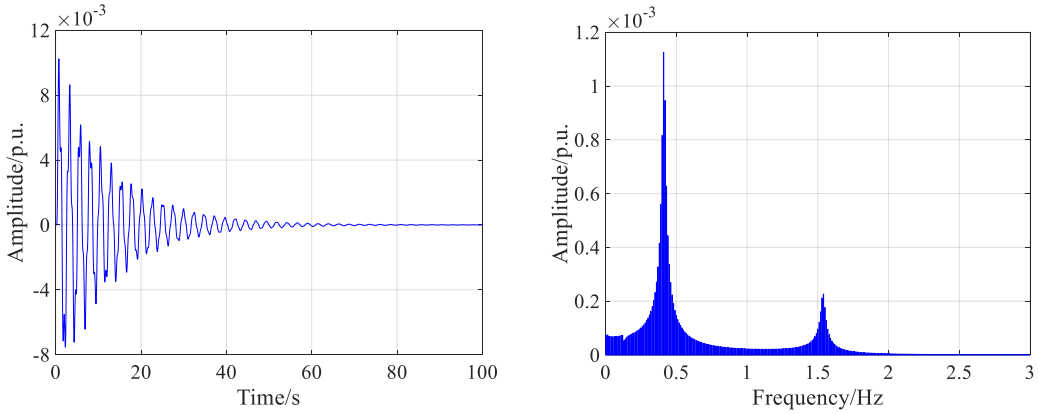

(a) (b)

Fig. 4.9. $\Delta P_{we,1}(t)$ and its amplitude-frequency characteristic in Scenario 4.1 in an FCWG-integrated 4M2A power system. (a). Plot of $\Delta P_{we,1}(t)$ in time domain. (b). Amplitude-frequency characteristic of $\Delta P_{we,1}(t)$ in frequency domain.

The imaginary parts of the interested eigenvalues are estimated as $2\pi \times 0.41j = 2.5761j$ and $2\pi \times 1.54j = 9.6761j$. According to the mentioned Steps 1-7 at the end of Section 4.5, the real parts of eigenvalues of the inherent MSOs at around 0.41 Hz and 1.54 Hz are estimated. The results are listed in Table 4.1.

Table 4.1 Application of EFA for estimating eigenvalues of interested MSOs in Scenario 4.1 of an FCWG-integrated 4M2A power system.

Interested frequency	Real eigenvalue	Estimated eigenvalue
0.41 Hz (inherent)	-0.0761±2.5889j	-0.0761±2.5761j
1.54 Hz (inherent)	-0.0997±9.6595j	-0.0998±9.6761j

It is noted that the real eigenvalues are calculated from the state matrix, which acts as a comparison. It can be found that the numerical estimation from the proposed Steps 1-7 has a high accuracy.

Through the study in Scenario 4.1, it can be revealed that the machine-side disturbances such as continuous wind fluctuations will only trigger the inherent MSOs, and the non-inherent MSO will not be excited even if the ARC is installed. The damping feature of the inherent MSOs of FCWG can be evaluated accurately by the extended EFA in this chapter.

(2) Scenario 4.2 (external grid disturbance)

In Scenario 4.2, there is no disturbance on the machine side of FCWG originally. A disturbance occurs to the mechanical power of G_1 (i.e., a conventional synchronous generator in this 4M2A power system) at 0.2 s and its value becomes 1.05 of the original one, which lasts for 0.1 s.

The plot of $\Delta P_{we,1}(t)$ and its amplitude-frequency characteristic are given in Fig. 4.10, and the plot of $\Delta P_{ARC\text{-}wt,1}(t)$ and its amplitude-frequency characteristic are given in Fig. 4.11.

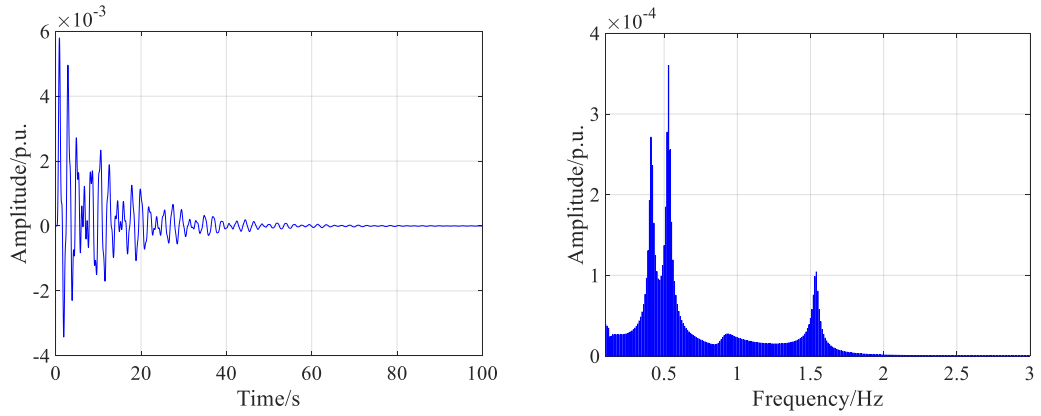

(a) (b)

Fig. 4.10. $\Delta P_{we,1}(t)$ and its amplitude-frequency characteristic in Scenario 4.2 in an FCWG-integrated 4M2A power system. (a). Plot of $\Delta P_{we,1}(t)$ in time domain. (b). Amplitude-frequency characteristic of $\Delta P_{we,1}(t)$ in frequency domain.

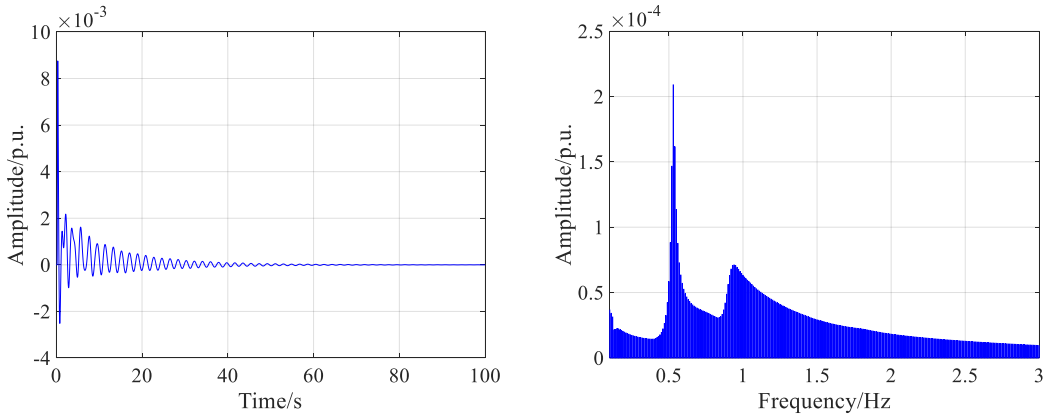

(a) (b)

Fig. 4.11. $\Delta P_{ARC\text{-}wt,1}(t)$ and its amplitude-frequency characteristic in Scenario 4.2 in an FCWG-integrated 4M2A power system. (a). Plot of $\Delta P_{ARC\text{-}wt,1}(t)$ in time domain. (b). Amplitude-frequency characteristic of $\Delta P_{ARC\text{-}wt,1}(t)$ in frequency domain.

It can be seen from Fig. 4.10 that there are three dominant MSOs at 0.41 Hz, 0.53 Hz, and 1.54 Hz monitored on the machine side of FCWG. It is known from Fig. 4.11 that the non-inherent MSO of 0.53 Hz is actually the inter-area oscillation mode of the external power grid that is introduced by ARC to the machine side of FCWG. While the

MSOs of 0.41 Hz and 1.54 Hz are the inherent ones of FCWG that are excited by the ARC.

The imaginary part of the eigenvalue of the non-inherent MSO is estimated as $2\pi\times0.53j=3.3301j$. According to the mentioned Steps 1-7 at the end of Section 4.5, the real parts of interested eigenvalues are estimated. The results are listed in Table 4.2. It can be found that the numerical estimations from the proposed Steps 1-7 demonstrates a high accuracy in Scenario 4.2.

Table 4.2 Application of EFA for estimating eigenvalues of interested MSOs in Scenario 4.2 of an FCWG-integrated 4M2A power system.

Interested frequency	Real eigenvalue	Estimated eigenvalue
0.41 Hz (inherent)	-0.0761±2.5889j	-0.0760±2.5761j
0.53 Hz (non-inherent)	-0.0682±3.3264j	-0.0682±3.3301j
1.54 Hz (inherent)	-0.0997±9.6595j	-0.0998±9.6761j

Through the study in Scenario 4.2, it can be seen that the disturbance of the external grid can be propagated to the machine side through ARC and excite the inherent MSOs of FCWG. The non-inherent MSO of FCWG can be only triggered by the disturbances of the external grid and introduced by ARC to the machine side of FCWG. The damping feature of both types of MSOs can be assessed by the extended EFA in this chapter.

(3) Scenario 4.3 (both PMSG and external grid disturbances)

In Scenario 4.3, a three-phase short-circuit fault occurs to the external power grid at 0.2 s, which lasts for 0.1 s. Meanwhile, a continuous disturbance happens to the mechanical power of PMSG.

The plot of $\Delta P_{we,1}(t)$ and its amplitude-frequency characteristic are given in Fig. 4.12.

It can be seen that the three-phase short-circuit fault of the external power grid can bring a great risk to the machine side dynamics of FCWG through ARC.

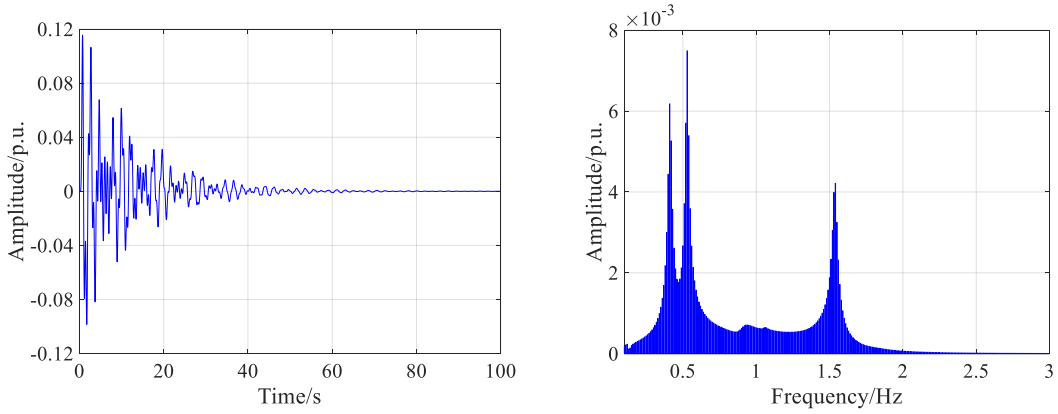

(a) (b)

Fig. 4.12. $\Delta P_{we,1}(t)$ and its amplitude-frequency characteristic in Scenario 4.3 in an FCWG-integrated 4M2A power system. (a). Plot of $\Delta P_{we,1}(t)$ in time domain. (b). Amplitude-frequency characteristic of $\Delta P_{we,1}(t)$ in frequency domain.

The real parts of eigenvalues of the interested MSOs are estimated, and the results are listed in Table 4.3, which still shows a high accurate.

Table 4.3 Application of EFA for estimating eigenvalues of interested MSOs in Scenario 4.3 of an FCWG-integrated 4M2A power system.

Interested frequency	Real eigenvalue	Estimated eigenvalue
0.41 Hz (inherent)	-0.0761±2.5889j	-0.0761±2.5761j
0.53 Hz (non-inherent)	-0.0682±3.3264j	-0.0681±3.3301j
1.54 Hz (inherent)	-0.0997±9.6595j	-0.0998±9.6761j

Through the study in Scenario 4.3, it can be indicated that the superposition of the short-circuit fault of the external grid and the disturbance of PMSG can pose a great threat to machine-side dynamics of FCWG. Both disturbances would contribute to the amplitude of the inherent MSOs. The extended EFA still possesses a high accuracy in this scenario.

(4) Scenario 4.4 (modal resonance)

In Scenario 4.4, the settings of disturbances of the external grid and PMSG are same with that in Scenario 4.3, but the setting of parameters of MSC is different from those in Scenario 4.3. The frequency of the inherent MSO becomes closer to that of the non-inherent MSO in this scenario.

The plot of $\Delta P_{we,1}(t)$ and its amplitude-frequency characteristic are given in Fig. 4.13. It can be seen that the amplitudes at 0.53 Hz and 0.58 Hz are much larger than the two in Scenario 4.3.

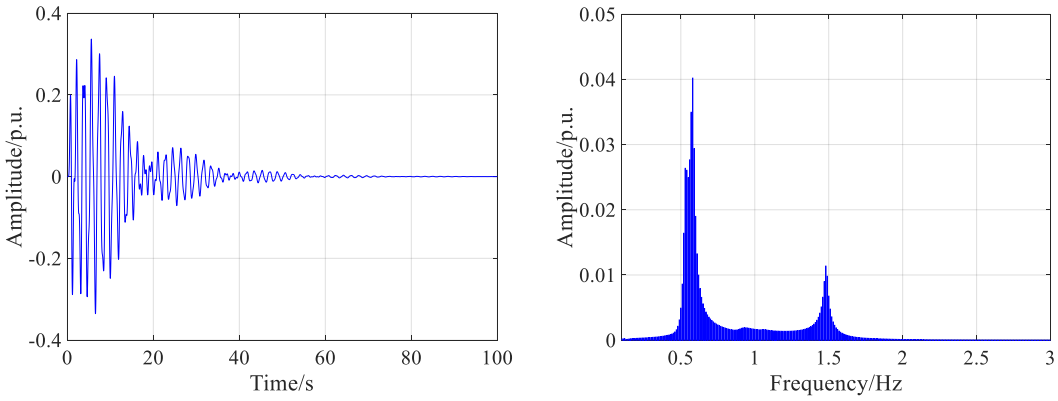

(a) (b)

Fig. 4.13. $\Delta P_{we,1}(t)$ and its amplitude-frequency characteristic in Scenario 4.4 in an FCWG-integrated 4M2A power system. (a). Plot of $\Delta P_{we,1}(t)$ in time domain. (b). Amplitude-frequency characteristic of $\Delta P_{we,1}(t)$ in frequency domain.

There are three dominant MSOs at 0.53 Hz, 0.58 Hz and 1.48 Hz. Among them, the MSO of 0.53 Hz is the non-inherent one introduced by ARC, and the MSOs of 0.58 Hz and 1.48 Hz are the inherent ones. The real eigenvalues and estimated eigenvalues are list in Table 4.4.

Table 4.4 Application of EFA for estimating eigenvalues of interested MSOs in Scenario 4.4 of an FCWG-integrated 4M2A power system.

Interested frequency	Real eigenvalue	Estimated eigenvalue
0.53 Hz (non-inherent)	-0.0751±3.3227j	-0.0752±3.3301j
0.58 Hz (inherent)	-0.0799±3.6447j	-0.0799±3.6442j
1.48 Hz (inherent)	-0.0889±9.3138j	-0.0890±9.2991j

Through the study in Scenario 4.4, it can be concluded that the improper parameter settings of controllers can cause the modal resonance between the inherent and non-inherent MSOs of FCWG. The extended EFA can accurately estimate the damping feature of MSOs to reduce this potential risk.

4.7 Summary

The key findings of this chapter are listed as follows: (1) the inherent MSO of FCWG can be excited by the disturbance of PMSG, while the non-inherent MSO would not be excited by the disturbance of PMSG regardless of the installation of ARC. The damping feature of inherent MSOs of FCWG can be investigated by the extended EFA accurately and efficiently; (2) when ARC is used, the EGO excited by the disturbance of the external grid can be introduced to the machine side of FCWG and becomes the non-inherent MSO. The inherent MSOs of FCWG can also be excited by the propagation of disturbances of the external grid through ARC. The extended EFA can perform satisfactorily in obtaining the damping feature of both the inherent and non-inherent MSO introduced by ARC; (3) the superposition of the short-circuit fault of the external grid and the disturbance of PMSG can significantly deteriorate the machine-

side dynamic performance of FCWG especially for inherent MSOs in terms of the oscillatory amplitude, and the accuracy of the estimated damping feature of MSOs can be also guaranteed under more severe disturbance condition; and (4) when the frequency of the inherent MSO is closer to that of the non-inherent MSO introduced by ARC, the severe modal resonance can be triggered on the machine side of FCWG, and the accuracy of the extended EFA can be still ensured under this resonance condition.

Chapter 5

Generalization of Energy Flow Analysis for Investigating Various Oscillations in Power Electronic Converter-penetrated Power Systems

5.1 Overview

In Chapter 3, the quantitative investigation of electromechanical oscillations of conventional synchronous generators using EFA is proposed. In Chapter 4, the EFA is extended to the machine side of FCWG to quantitatively investigate MSOs of FCWG. The PECs have brought diversified dynamics to the modern power system, and the EFA in Chapter 3 and 4 still shows the limitation to tackle the various oscillations in the PEC-penetrated power system. Therefore, it is necessary to further widen the application of EFA to investigate the oscillatory stability of PEC-penetrated power systems. In this chapter, the generalized oscillation loop is structured based on the second-order differential operations in a studied control loop of PEC. On this basis, the proposed EFA in Chapter 3 is generalized for quantitatively investigating various oscillations in the PEC-penetrated power system. Finally, taking the GSC of the FCWG system as an example, the application of the generalized EFA is further discussed and tested considering the potential modal resonance between the inherent GSO and non-inherent GSO (i.e., EGO) to consolidate the oscillatory stability of the PEC-penetrated power system.

5.2 Generalization of Oscillation Loop and Energy Flow Analysis in Power Electronic Converter-penetrated Power Systems

The schematic of the PEC-penetrated power grid is shown in Fig. 5.1. In this section, the electromechanical oscillation loop of the conventional synchronous generator is generalized to PECs, and the proposed EFA in Chapter 3 is further generalized to quantitatively investigate the various oscillations of the PEC-penetrated power grid, i.e., the generalized EFA.

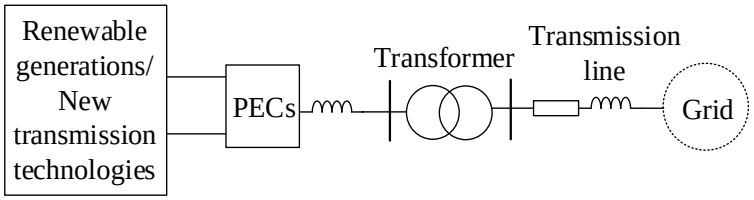

Fig. 5.1. Schematic of a PEC-penetrated power grid.

The feature of the electromechanical oscillation loop of the synchronous generator is that it has the second-order differential operations for two state variables, i.e., the power angle deviation and angular frequency deviation. With the help of this feature, a generalized oscillation loop is structured.

Two state variables of the second-order differential operations are selected in the studied control loop of PEC. In order to represent the whole power system considering the arbitrary types and control schemes of PECs, the linearization of the whole power system is derived as (5.1).

$$\begin{bmatrix} s\Delta SV_{1,i}(s) \\ s\Delta SV_{2,i}(s) \\ s\Delta \boldsymbol{Z}(s) \end{bmatrix} = \begin{bmatrix} A_{11} & A_{12} & \boldsymbol{A_{13}} \\ A_{21} & A_{22} & \boldsymbol{A_{23}} \\ \boldsymbol{A_{31}} & \boldsymbol{A_{32}} & \boldsymbol{A_{33}} \end{bmatrix} \begin{bmatrix} \Delta SV_{1,i}(s) \\ \Delta SV_{2,i}(s) \\ \Delta \boldsymbol{Z}(s) \end{bmatrix} \tag{5.1}$$

where $\Delta SV_{1,i}(s)$ and $\Delta SV_{2,i}(s)$ are the first and second selected state variable of the

studied control loop of the *i*-th PEC, respectively; A_{11}, A_{12}, $\boldsymbol{A_{13}}$, A_{21}, A_{22}, $\boldsymbol{A_{23}}$, $\boldsymbol{A_{31}}$, $\boldsymbol{A_{32}}$ and $\boldsymbol{A_{33}}$ are the block sub-matrices of the state matrix; and $\Delta\boldsymbol{Z}(s)$ that includes the state variables of the whole system except $\Delta SV_{1,i}(s)$ and $\Delta SV_{2,i}(s)$.

Then, (5.2)-(5.4) can be obtained, respectively.

$$\Delta SV_{1,i}(s) = \frac{A_{12}}{s - A_{11}} \Delta SV_{2,i}(s) + \frac{\boldsymbol{A_{13}}}{s - A_{11}} \Delta \boldsymbol{Z}(s) \tag{5.2}$$

$$\Delta SV_{2,i}(s) = \frac{A_{21}}{s - A_{22}} \Delta SV_{1,i}(s) + \frac{\boldsymbol{A_{23}}}{s - A_{22}} \Delta \boldsymbol{Z}(s) \tag{5.3}$$

$$\Delta \boldsymbol{Z}(s) = \frac{\boldsymbol{A_{31}}}{s\mathbf{I} - \boldsymbol{A_{33}}} \Delta SV_{1,i}(s) + \frac{\boldsymbol{A_{32}}}{s\mathbf{I} - \boldsymbol{A_{33}}} \Delta SV_{2,i}(s) \tag{5.4}$$

According to (5.2)-(5.4), the construction of the generalized oscillation loop with respect to a studied control loop of PEC is shown in Fig. 5.2, where $F(s)$ is an equation with respect to $\Delta SV_{2,i}(s)$.

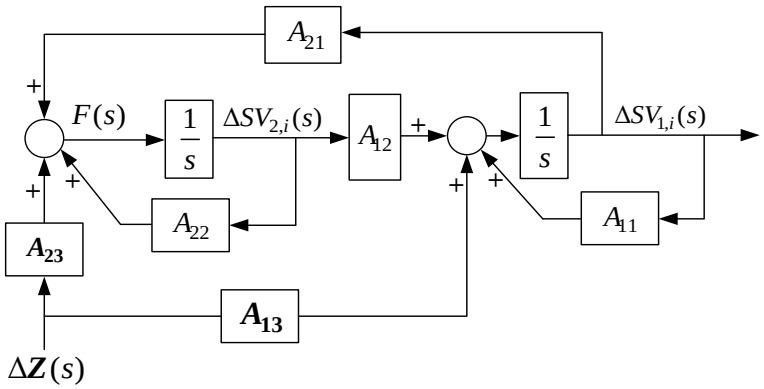

Fig. 5.2. Construction of a generalized oscillation loop with respect to a studied control loop of PEC.

For the generalized oscillation loop of the *i*-th PEC in a system, the virtual torque deviation provided by the external controllers of the generalized oscillation loop is defined as follows

$$\Delta T_{v,i}(s) = K_{vd,i}\Delta SV_{2,i}(s) + K_{vs,i}\Delta SV_{1,i}(s) \tag{5.5}$$

where $\Delta T_{v,i}(s)$ is the virtual torque deviation provided by the external controllers of the generalized oscillation loop of the i-th PEC; $K_{vd,i}$ and $K_{vs,i}$ are the virtual damping and synchronizing torque coefficients related to $\Delta T_{v,i}(s)$.

It can be seen from Fig. 5.2 that $\Delta SV_{2,i}(s)$ acts as the virtual angular frequency in the generalized oscillation loop. According to the definition of the energy, the generalized oscillatory energy flow dissipation is defined as (5.6).

$$W_{vd,i} = \int_0^{+\infty} \Delta T_{v,i}(t)\Delta SV_{2,i}(t)\mathrm{d}t = \int_0^{+\infty} K_{vd,i}\left(\Delta SV_{2,i}(t)\right)^2\mathrm{d}t \tag{5.6}$$

where $W_{vd,i}$ is the generalized oscillatory energy flow dissipation of the i-th PEC.

Thus, (5.7) can be further derived. $F(t)$ is the time-domain form of $F(s)$. The virtual natural damping is reflected from A_{22}, and the virtual non-natural damping is reflected from $K_{vd,i}$.

$$\begin{aligned} K_{vd,i} &= \frac{\int_0^{+\infty}\left(F(t) - A_{12}\Delta SV_{1,i}(t) - A_{22}\Delta SV_{2,i}(t)\right)\Delta SV_{2,i}(t)\mathrm{d}t}{\int_0^{+\infty}\left(\Delta SV_{2,i}(t)\right)^2\mathrm{d}t} \\ &= \frac{\int_0^{+\infty} F(t)\Delta SV_{2,i}(t)\mathrm{d}t}{\int_0^{+\infty}\left(\Delta SV_{2,i}(t)\right)^2\mathrm{d}t} - A_{22} \end{aligned} \tag{5.7}$$

The methodology in Chapter 3 is generalized for the quantitative investigation of the oscillatory stability of PEC-penetrated power systems.

Substitute (5.3) and (5.4) into (5.2), and then (5.8) can be derived.

$$\Delta SV_{1,i}(s) = \frac{\frac{A_{12}}{s - A_{11}} + \frac{\boldsymbol{A_{13}}}{s - A_{11}}\frac{\boldsymbol{A_{32}}}{s\mathbf{I} - \boldsymbol{A_{33}}}}{1 - \frac{\boldsymbol{A_{13}}}{s - A_{11}}\frac{\boldsymbol{A_{31}}}{s\mathbf{I} - \boldsymbol{A_{33}}}}\Delta SV_{2,i}(s) \tag{5.8}$$

Substitute (5.2) and (5.3) into (5.4), and then (5.9) can be derived.

$$\Delta \boldsymbol{Z}(s)=\left(\frac{\boldsymbol{A_{31}}}{s\mathbf{I}-\boldsymbol{A_{33}}}\frac{\frac{A_{12}}{s-A_{11}}+\frac{\boldsymbol{A_{13}}}{s-A_{11}}\frac{\boldsymbol{A_{32}}}{s\mathbf{I}-\boldsymbol{A_{33}}}}{1-\frac{\boldsymbol{A_{13}}}{s-A_{11}}\frac{\boldsymbol{A_{31}}}{s\mathbf{I}-\boldsymbol{A_{33}}}}+\frac{\boldsymbol{A_{32}}}{s\mathbf{I}-\boldsymbol{A_{33}}}\right)\Delta SV_{2,i}(s) \tag{5.9}$$

Substitute (5.8) and (5.9) into (5.3), and (5.10) can be obtained.

$$s=\left(A_{21}+\boldsymbol{A_{23}}\frac{\boldsymbol{A_{31}}}{s\mathbf{I}-\boldsymbol{A_{33}}}\right)\frac{\frac{A_{12}}{s-A_{11}}+\frac{\boldsymbol{A_{13}}}{s-A_{11}}\frac{\boldsymbol{A_{32}}}{s\mathbf{I}-\boldsymbol{A_{33}}}}{1-\frac{\boldsymbol{A_{13}}}{s-A_{11}}\frac{\boldsymbol{A_{31}}}{s\mathbf{I}-\boldsymbol{A_{33}}}}+\boldsymbol{A_{23}}\frac{\boldsymbol{A_{32}}}{s\mathbf{I}-\boldsymbol{A_{33}}}+A_{22} \tag{5.10}$$

Similarly, (5.11) can be also derived.

$$\frac{F(s)}{\Delta SV_{2,i}(s)}=\left(A_{21}+\boldsymbol{A_{23}}\frac{\boldsymbol{A_{31}}}{s\mathbf{I}-\boldsymbol{A_{33}}}\right)\frac{\frac{A_{12}}{s-A_{11}}+\frac{\boldsymbol{A_{13}}}{s-A_{11}}\frac{\boldsymbol{A_{32}}}{s\mathbf{I}-\boldsymbol{A_{33}}}}{1-\frac{\boldsymbol{A_{13}}}{s-A_{11}}\frac{\boldsymbol{A_{31}}}{s\mathbf{I}-\boldsymbol{A_{33}}}}+\boldsymbol{A_{23}}\frac{\boldsymbol{A_{32}}}{s\mathbf{I}-\boldsymbol{A_{33}}}+A_{22} \tag{5.11}$$

Substitute a pair of eigenvalues of an interested oscillation $\lambda_g=\sigma_g\pm \mathrm{j}w_g$ observed in the studied control loop of PEC, and (5.12) can be obtained.

$$\frac{F(\lambda_g)}{\Delta SV_{2,i}(\lambda_g)}=\lambda_g \tag{5.12}$$

Convert (5.12) from the frequency domain to time domain by the Parseval's theorem, i.e., (5.13). Eq. (5.13) is the time-domain form of the generalized EFA-based methodology.

$$\sigma_g=\frac{\int_0^{+\infty}F^{w_g}(t\,|\,\sigma_g)\Delta SV_{2,i}^{w_g}(t\,|\,\sigma_g)\,\mathrm{d}t}{\int_0^{+\infty}\left(\Delta SV_{2,i}^{w_g}(t\,|\,\sigma_g)\right)^2\mathrm{d}t} \tag{5.13}$$

where $\Delta SV_{2,i}^{w_g}(t\,|\,\sigma_g)$ is the reconstructed and decomposed signal from $\Delta SV_{2,i}(t)$; and $\Delta SV_{2,i}(t)$ is the time-domain form of $\Delta SV_{2,i}(s)$. Specifically, $\Delta SV_{2,i}(t)$ is multiplied by

$e^{-\sigma_g t}$ and then is decomposed with respect to w_g. $F^{w_g}(t \mid \sigma_g)$ is the reconstructed and decomposed signal from $F(t)$; and $F(t)$ is the time-domain form of $F(s)$. Specifically, $F(t)$ is multiplied by $e^{-\sigma_g t}$ and then is decomposed with respect to w_g.

5.3 Application of Generalized Oscillation Loop and Energy Flow Analysis for Grid-side Converter of Full Converter-based Wind Generation

5.3.1 Control Loops of Grid-side Converter of Full Converter-based Wind Generation

In this section, FCWG is taken as an example to demonstrate and explain the application of the generalized oscillation loop and EFA for GSOs of FCWG.

The main components of FCWG have been discussed in Chapter 4, which are not repeated here. Generally, PMSG and MSC do not respond to the dynamics of the external power grid since they are decoupled from the external power grid by the DC-link.

Since this chapter focuses on the GSOs of FCWG, the typical control loops of GSC and PLL are introduced in Fig. 5.3 and 5.4, respectively. It can be seen that there are mainly four control loops for GSC: DC capacitor voltage control loop, *d*-axis current control loop, *q*-axis current control loop, and reactive power control loop.

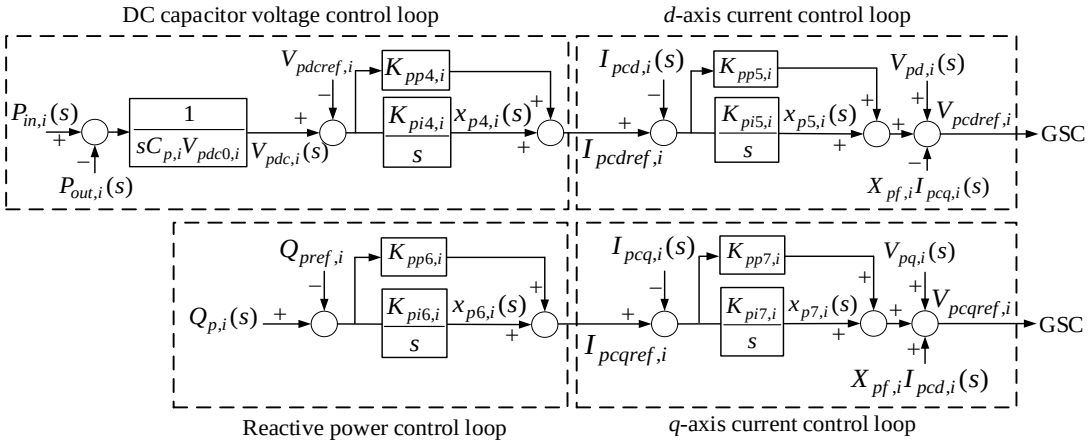

Fig. 5.3. The control configuration of GSC of FCWG.

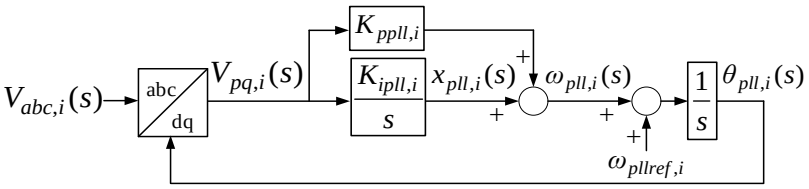

Fig.5.4. The control configuration of PLL of FCWG.

In Fig. 5.3, the meanings of major variables of the DC capacitor voltage control loop of the *i*-th FCWG are as follows: $V_{pdc,i}(s)$ is the DC voltage across the capacitor, $x_{p4,i}(s)$ is an intermediate variable, $P_{in,i}(s)$ is the active power input, $P_{out,i}(s)$ is the active power output, $C_{p,i}$ is the capacitance, $V_{pdc0,i}$ is the steady-state value of DC voltage, $K_{pp4,i}$ is the proportional time constant, $K_{pi4,i}$ is the integral time constant. For reactive power, *d*-axis and *q*-axis current control loops of the *i*-th FCWG, $I_{pcd,i}(s)$ and $I_{pcq,i}(s)$ are the *d*-axis and *q*-axis output currents of GSC, $x_{p5,i}(s)$, $x_{p6,i}(s)$ and $x_{p7,i}(s)$ are intermediate variables, $K_{pp5,i}$, $K_{pp6,i}$ and $K_{pp7,i}$ are proportional time constants, $K_{pi5,i}$, $K_{pi6,i}$ and $K_{pi7,i}$ are integral time constants; $V_{pcd,i}(s)$ and $V_{pcq,i}(s)$ are the *d*-axis and *q*-axis output voltages of GSC, $\Delta V_{pd,i}(s)$ and $\Delta V_{pq,i}(s)$ are the *d*-axis and *q*-axis voltages at the point of common coupling (PCC), respectively. In Fig. 5.4, the meanings of major variables of PLL of

the *i*-th FCWG are as follows: $x_{pll,i}(s)$ is an intermediate variable, $K_{ppll,i}$ is the proportional time constant, $K_{ipll,i}$ is the integral time constant. For the above-mentioned variables, prefix Δ can represent the deviation of the related variable, which will not be repeated in Subsection 5.3.2 and 5.3.3.

5.3.2 Demonstration in DC Capacitor Voltage Control Loop

For the DC capacitor voltage control loop of GSC of the *i*-th FCWG, $\Delta SV_{1,i}(s)$ is $\Delta x_{p4,i}(s)$, and $\Delta SV_{2,i}(s)$ is $\Delta V_{pdc,i}(s)$. The related differential equations are shown as follows

$$s\Delta x_{p4,i}(s) = K_{pi4,i}\Delta V_{pdc,i}(s) \tag{5.14}$$

$$s\Delta V_{pdc,i}(s) = \frac{1}{C_{p,i}V_{pdc0,i}}\left(\Delta P_{in,i}(s) - \Delta P_{out,i}(s)\right) \tag{5.15}$$

The output power from the DC-link can be represented as

$$\Delta P_{out,i}(s) = V_{pd0,i}\Delta I_{pcd,i}(s) + V_{pq0,i}\Delta I_{pcq,i}(s) + I_{pcd0,i}\Delta V_{pd,i}(s) + I_{pcq0,i}\Delta V_{pq,i}(s) \tag{5.16}$$

where $I_{pcd0,i}$ and $I_{pcq0,i}$ are the steady-state values of *d*-axis and *q*-axis output currents of GSC, respectively. $V_{pd0,i}$ and $V_{pq0,i}$ are the steady-state values of *d*-axis and *q*-axis voltages at PCC, respectively.

Then, (5.15) can be further derived as

$$\begin{aligned} &sC_{p,i}V_{pdc0,i}\Delta V_{pdc,i}(s) = \Delta P_{in,i}(s) - K_{pp4,i}V_{pd0,i}\Delta V_{pdc,i}(s) \\ &-V_{pd0,i}\Delta x_{p4,i}(s) - V_{pq0,i}\Delta I_{pcq,i}(s) - I_{pcd0,i}\Delta V_{pd,i}(s) - I_{pcq0,i}\Delta V_{pq,i}(s) \end{aligned} \tag{5.17}$$

Thus, the generalized oscillation loop with respect to the DC capacitor voltage control loop of GSC of the *i*-th FCWG is derived in Fig. 5.5.

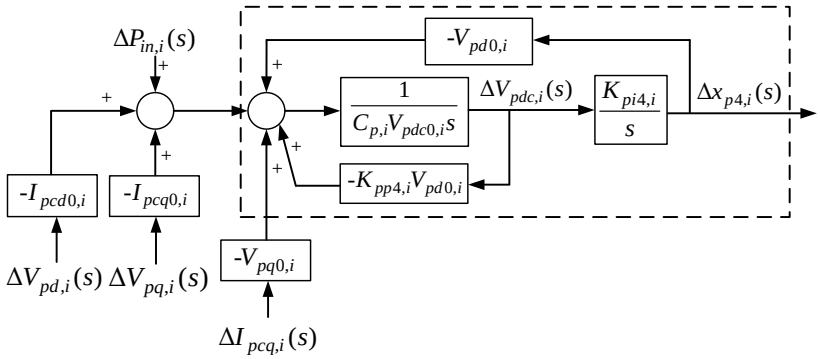

Fig. 5.5. Generalized oscillation loop with respect to DC capacitor voltage control loop of GSC.

The virtual inertia constant $M_{dc,i}$, virtual natural damping coefficient $D_{dc,i}$, virtual natural synchronizing coefficient $S_{dc,i}$ in the DC capacitor voltage control loop can be derived as

$$\begin{cases} M_{dc,i} = C_{p,i}V_{pdc0,i} \\ D_{dc,i} = K_{pp4,i}V_{pd0,i} \\ S_{dc,i} = K_{pi4,i}V_{pd0,i} \end{cases} \tag{5.18}$$

Thus, the pair of open-loop eigenvalues $\lambda_{dc0,i}$ of the inherent GSO of the DC capacitor voltage control loop of the i-th FCWG are calculated as

$$\lambda_{dc0,i} = \frac{-D_{dc,i} \pm \sqrt{D_{dc,i}^2 - 4M_{dc,i}S_{dc,i}}}{2M_{dc,i}} \tag{5.19}$$

Substitute related variables into (5.13), the close-loop damping $\sigma_{dc,i}$ of the inherent/non-inherent GSO of the DC capacitor voltage control loop of the i-th FCWG with respect to the oscillation angular frequency $w_{dc,i}$ is given by (5.20).

$$\sigma_{dc,i} = \frac{\int_0^{+\infty} \left(\Delta P_{in,i}^{w_{dc,i}}(t \mid \sigma_{dc,i}) - \Delta P_{out,i}^{w_{dc,i}}(t \mid \sigma_{dc,i}) \right) \Delta V_{pdc,\,i}^{w_{dc,i}}(t \mid \sigma_{dc,i}) \, \mathrm{d}t}{C_{p,i}V_{pdc0,i} \int_0^{+\infty} \left(\Delta V_{pdc,\,i}^{w_{dc,i}}(t \mid \sigma_{dc,i}) \right)^2 \mathrm{d}t} \tag{5.20}$$

5.3.3 Demonstration in Phase Locked Loop

For the PLL, $\Delta SV_{1,i}(s)$ is $\Delta\theta_{pll,i}(s)$, and $\Delta SV_{2,i}(s)$ is $\Delta x_{pll,i}(s)$. The related differential equations are shown as follows

$$s\Delta\theta_{pll,i}(s) = \Delta x_{pll,i}(s) + K_{ppll,i}\Delta V_{pq,i}(s) \tag{5.21}$$

$$s\Delta x_{pll,i}(s) = K_{ipll,i}\Delta V_{pq,i}(s) \tag{5.22}$$

Generally, $\Delta V_{pq,i}(s)$ can be represented as (5.23).

$$\Delta V_{pq,i}(s) \approx V_{pcc0,i}\left(\Delta\theta_{pcc,i}(s) - \Delta\theta_{pll,i}(s)\right) \tag{5.23}$$

where $V_{pcc0,i}$ is the steady-state value of the PCC voltage, and $\Delta\theta_{pcc,i}(s)$ is the deviation of the PCC voltage angle.

Consequently, the generalized oscillation loop with respect to PLL of the *i*-th FCWG is derived as Fig. 5.6.

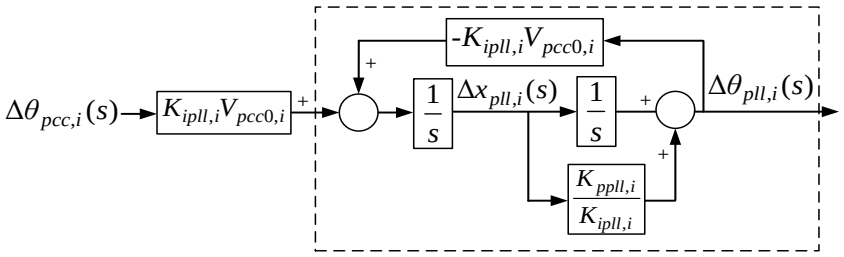

Fig. 5.6. Generalized oscillation loop with respect to PLL.

The virtual inertia constant $M_{pll,i}$, virtual damping coefficient $D_{pll,i}$, virtual synchronizing coefficient $S_{pll,i}$ of PLL of the *i*-th FCWG can be derived as

$$\begin{cases} M_{pll,i} = 1 \\ D_{pll,i} = V_{pcc0,i}K_{ppll,i} \\ S_{pll,i} = V_{pcc0,i}K_{ipll,i} \end{cases} \tag{5.24}$$

Thus, the pair of open-loop eigenvalues $\lambda_{pll0,i}$ of the inherent GSO in PLL of the *i*-

th FCWG are calculated as

$$\lambda_{pll0,i} = \frac{-D_{pll,i} \pm \sqrt{D_{pll,i}^2 - 4M_{pll,i}S_{pll,i}}}{2M_{pll,i}} \tag{5.25}$$

Substitute the related variables into (5.13), the close-loop damping $\sigma_{pll,i}$ of the inherent/non-inherent GSO in PLL of the *i*-th FCWG with respect to the oscillation angular frequency $w_{pll,i}$ can be calculated from (5.26).

$$\sigma_{pll,i} = \frac{\int_0^{+\infty} K_{ipll,i}\Delta V_{pq,i}^{w_{pll,i}}(t \mid \sigma_{pll,i})\Delta x_{pll,i}^{w_{pll,i}}(t \mid \sigma_{pll,i})\,\mathrm{d}t}{\int_0^{+\infty}\left(\Delta x_{pll,i}^{w_{pll,i}}(t \mid \sigma_{pll,i})\right)^2\,\mathrm{d}t} \tag{5.26}$$

It is worth pointing out that the open-loop analysis has very limited influence on the calculation of the oscillation frequency (i.e. the imaginary part of eigenvalue). Thus, the simplification is suitable for the parameter setting of control loops of GSC to prevent potential resonance with EGO.

5.4 Case Studies

The generalized EFA in Section 5.3 is verified in Subsections 5.4.1 through an FCWG-integrated 4M2A power system. Then the application of the generalized oscillation loop and generalized EFA to consolidate the oscillatory stability of the PEC-penetrated power system is discussed in Subsection 5.4.2 through an FCWG-integrated 16M5A power system.

5.4.1 Verification in a 4-machine 2-area Power System with a Full Converter-based Wind Generation

The line diagram of a 4M2A power system with an FCWG has been given by Fig.

4.8, which is not repeated here. There is an FCWG installed at bus 5. The base capacity of this power system is 100 MVA. A disturbance occurs to the mechanical power of G_1 at 0.2 s and its value becomes 1.05 of the original one, which lasts for 0.1 s. The major parameters of control loops of GSC of FCWG are given in the Appendix A.5.

(1) Scenario 5.1

In this scenario, there is no resonance among each oscillation mode. Fig. 5.7 shows the characteristics of $\Delta V_{pdc,i}(t)$ in both time and frequency domains. It can be seen that there are mainly two modes in the DC capacitor voltage control loop, in which 0.53 Hz is the non-inherent GSO (i.e., the EGO) and 0.28 Hz is the inherent GSO of the DC capacitor voltage control loop. Table 5.1 provides the verification of the quantitative assessment of GSOs in the DC capacitor voltage control loop using the generalized EFA.

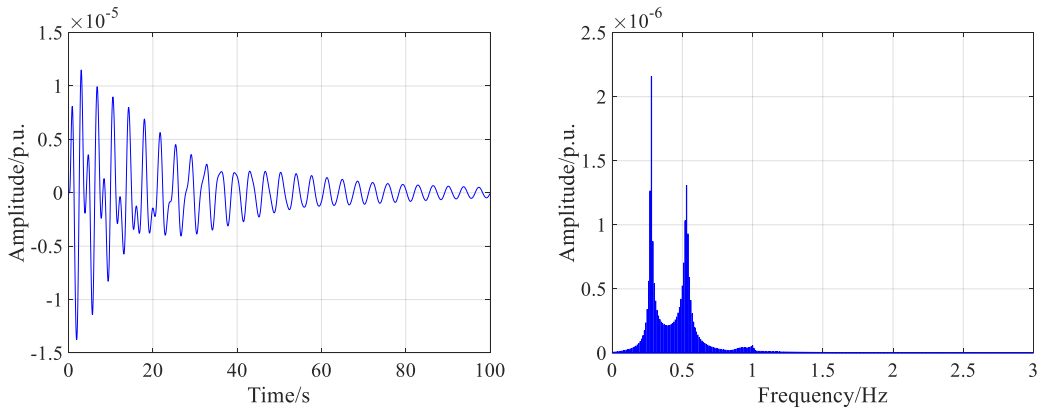

(a) (b)

Fig. 5.7. $\Delta V_{pdc,i}(t)$ and its amplitude-characteristic in Scenario 5.1 in an FCWG-integrated 4M2A power system. (a). Plot of $\Delta V_{pdc,i}(t)$ in time domain. (b) Amplitude-frequency characteristic of $\Delta V_{pdc,i}(t)$ in frequency domain.

Table 5.1 Verification of EFA for estimating eigenvalues of interested GSOs in DC capacitor voltage control loop in Scenario 5.1 of an FCWG-integrated 4M2A power system.

Interested mode	Real eigenvalue	Estimated eigenvalue
0.53 Hz (non-inherent GSO)	-0.0707±3.3278j	-0.0707±3.3301j
0.28 Hz (inherent GSO)	-0.0266±1.7410j	-0.0266±1.7593j

Fig. 5.8 shows the characteristics of $\Delta V_{pq,i}(t)$ in both time and frequency domains. It can be seen that there are mainly two modes in the PLL, in which 0.53 Hz is the non-inherent GSO (i.e., the EGO) and 1.0 Hz is the inherent GSO of PLL. Table 5.2 provides the verification of the quantitative assessment of GSOs in PLL using the generalized EFA.

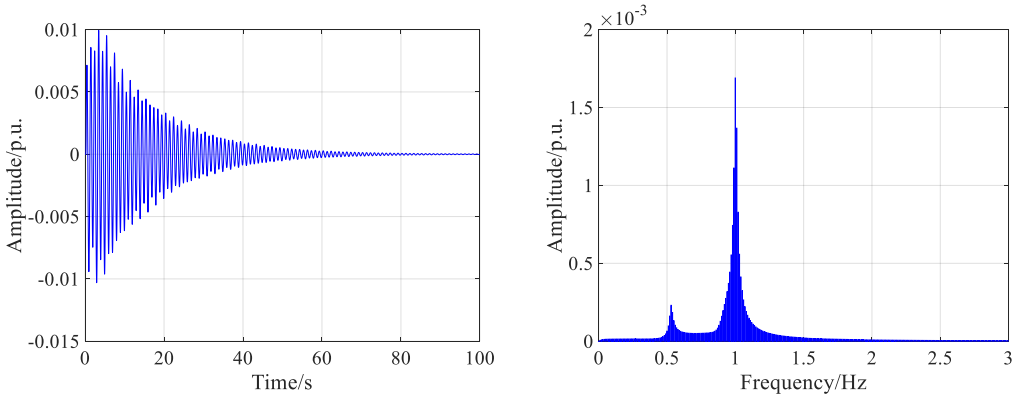

(a) (b)

Fig. 5.8. $\Delta V_{pq,i}(t)$ and its amplitude-characteristic in Scenario 5.1 in an FCWG-integrated 4M2A power system. (a). Plot of $\Delta V_{pq,i}(t)$ in time domain. (b). Amplitude-frequency characteristic of $\Delta V_{pq,i}(t)$ in frequency domain.

Table 5.2 Verification of EFA for estimating eigenvalues of interested GSOs in PLL in Scenario 5.1 of an FCWG-integrated 4M2A power system.

Interested mode	Real eigenvalue	Estimated eigenvalue
0.53 Hz (non-inherent GSO)	-0.0707±3.3278j	-0.0707±3.3301j
1.0 Hz (inherent GSO)	-0.0626±6.2994j	-0.0626±6.2832j

Through this scenario, the following conclusions can be summarized: in the case of

no resonance, both inherent and non-inherent GSOs can be observed in the related control loop of GSC, and the generalized EFA showes a good accuracy.

(2) Scenario 5.2

In this scenario, there is a resonance between the non-inherent GSO (i.e., EGO) and inherent GSO in the DC capacitor voltage control loop. Specifically, through adjusting the integral time constant of the DC capacitor voltage control loop, the frequency of its inherent GSO gradually approaches that of its non-inherent GSO.

When the frequency of the inherent GSO of the DC capacitor voltage control loop approaches that of the non-inherent GSO, the resonance phenomenon can occur. Fig. 5.9 shows the characteristics of $\Delta V_{pdc,i}(t)$ in both time and frequency domains in this scenario. It can be seen that the oscillatory amplitude is obviously increased, that is to say, the harm of the oscillation is greatly increased. Table 5.3 provides the verification of the related quantitative assessment in this scenario.

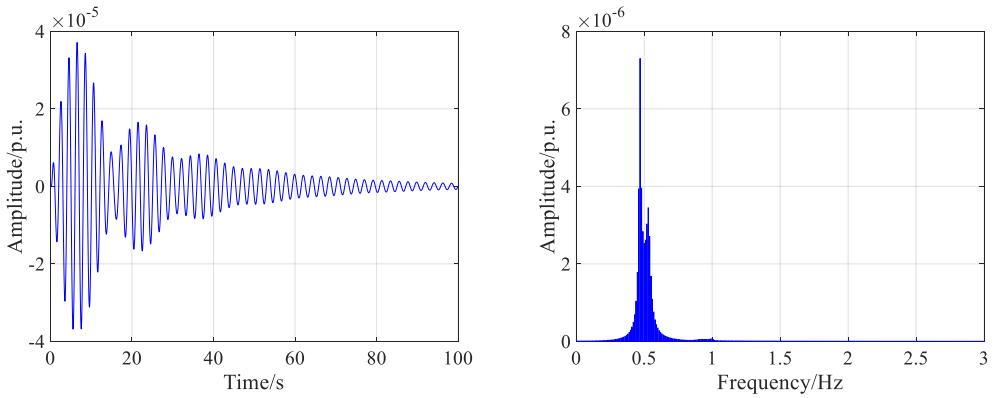

(a) (b)

Fig. 5.9. $\Delta V_{pdc,i}(t)$ and its amplitude-characteristic in Scenario 5.2 in an FCWG-integrated 4M2A power system. (a). Plot of $\Delta V_{pdc,i}(t)$ in time domain. (b). Amplitude-frequency characteristic of $\Delta V_{pdc,i}(t)$ in frequency domain.

Table 5.3 Verification of EFA for estimating eigenvalues of interested GSOs in DC capacitor voltage control loop in Scenario 5.2 of an FCWG-integrated 4M2A power system.

Interested mode	Real eigenvalue	Estimated eigenvalue
0.53 Hz (non-inherent GSO)	-0.0857±3.3481j	-0.0861±3.3301j
0.47 Hz (inherent GSO)	-0.0360±2.9397j	-0.0360±2.9531j

Through this scenario, the following conclusions can be summarized: when the frequency of the inherent GSO approaches that of the non-inherent GSO from small to large in the DC capacitor voltage control loop, the inherent GSO plays a positive role for the damping of the non-inherent GSO. The generalized EFA shows a good accuracy.

(3) Scenario 5.3

On the basis of Scenario 5.2, through further adjusting the integral time constant of the DC capacitor voltage control loop, the frequency of the inherent GSO becomes slightly higher than that of the non-inherent GSO in the DC capacitor voltage control loop, i.e., Scenario 5.3.

In this scenario, the inherent GSO still shows the resonance effect with the non-inherent GSO in the DC capacitor voltage control loop. Fig. 5.10 shows the characteristics of $\Delta V_{pdc,i}(t)$ in both time and frequency domains in this scenario. Table 5.4 provides the verification of the related quantitative assessment in this scenario.

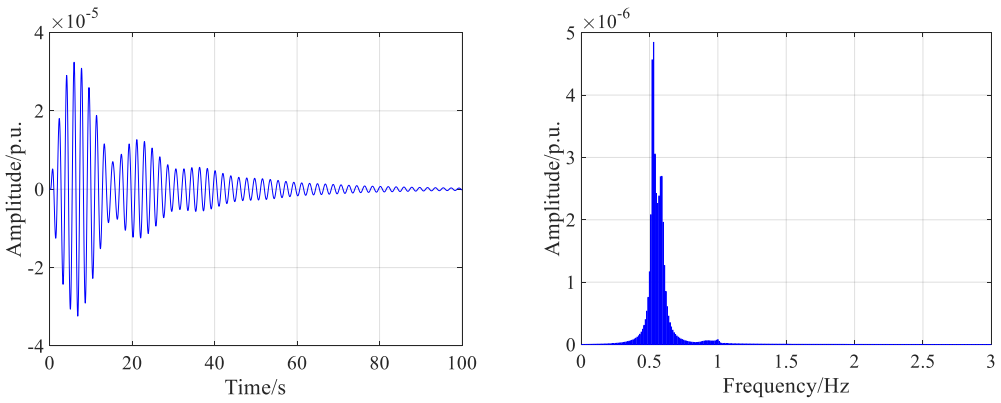

(a) (b)

Fig. 5.10. $\Delta V_{pdc,i}(t)$ and its amplitude-characteristic in Scenario 5.3 in an FCWG-integrated 4M2A power system. (a). Plot of $\Delta V_{pdc,i}(t)$ in time domain. (b). Amplitude-frequency characteristic of $\Delta V_{pdc,i}(t)$ in frequency domain.

Table 5.4 Verification of EFA for estimating eigenvalues of interested GSOs in DC capacitor voltage control loop in Scenario 5.3 of an FCWG-integrated 4M2A power system.

Interested mode	Real eigenvalue	Estimated eigenvalue
0.53 Hz (non-inherent GSO)	-0.0449±3.2943j	-0.0449±3.3301j
0.59 Hz (inherent GSO)	-0.0981±3.7054j	-0.0980±3.7071j

Through this scenario, the following conclusions can be summarized: when the frequency of the inherent GSO exceeds that of the non-inherent GSO in the DC capacitor voltage control loop, the inherent GSO plays a negative role for the damping of the non-inherent GSO. The generalized EFA still shows a good accuracy.

(4) Scenario 5.4

In this scenario, there is a resonance between the inherent and non-inherent GSOs of PLL. Specifically, through adjusting the integral time constant of PLL, the oscillation frequency of the inherent GSO of PLL gradually approaches to that of the non-inherent GSO (i.e., EGO).

Fig. 5.11 shows the characteristics of $\Delta V_{pq,i}$ (t) in both time and frequency domains in this scenario. It can be seen that the resonance can occur, and the harm of the oscillation is obviously increased. Table 5.5 provides the verification of the related quantitative assessment in this scenario.

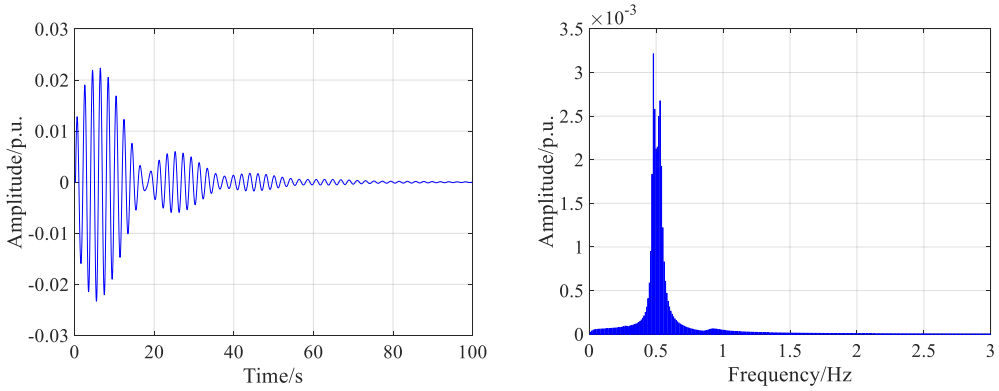

(a) (b)

Fig. 5.11. $\Delta V_{pq,i}(t)$ and its amplitude-characteristic in Scenario 5.4 in an FCWG-integrated 4M2A power system. (a). Plot of $\Delta V_{pq,i}(t)$ in time domain. (b). Amplitude-frequency characteristic of $\Delta V_{pq,i}(t)$ in frequency domain.

Table 5.5 Verification of EFA for estimating eigenvalues of interested GSOs in PLL in Scenario 5.4 of an FCWG-integrated 4M2A power system.

Interested mode	Real eigenvalue	Estimated eigenvalue
0.53 Hz (non-inherent GSO)	-0.0850±3.3312j	-0.0852±3.3301j
0.48 Hz (inherent GSO)	-0.0549±3.0111j	-0.0548±3.0159j

Through this scenario, the following conclusions can be summarized: when there is a resonance between the inherent and non-inherent GSOs in PLL, and the frequency of the inherent GSO is slightly less than that of the non-inherent GSO, the inherent GSO plays a positive role for the damping of the non-inherent GSO. The generalized EFA can still show a good performance.

(5) Scenario 5.5

On the basis of Scenario 5.4, by further adjusting the integral time constant of PLL, the frequency of the inherent GSO becomes slightly higher than that of the non-inherent GSO in PLL, i.e., Scenario 5.5.

In this scenario, the inherent GSO of PLL still shows the resonance effect with the non-inherent GSO of PLL. Fig. 5.12 shows the characteristics of $\Delta V_{pq,i}$ (t) in both time and frequency domains. It can be seen that the harm of the oscillation is still severe. Table 5.6 provides the verification of the related quantitative assessment in this scenario.

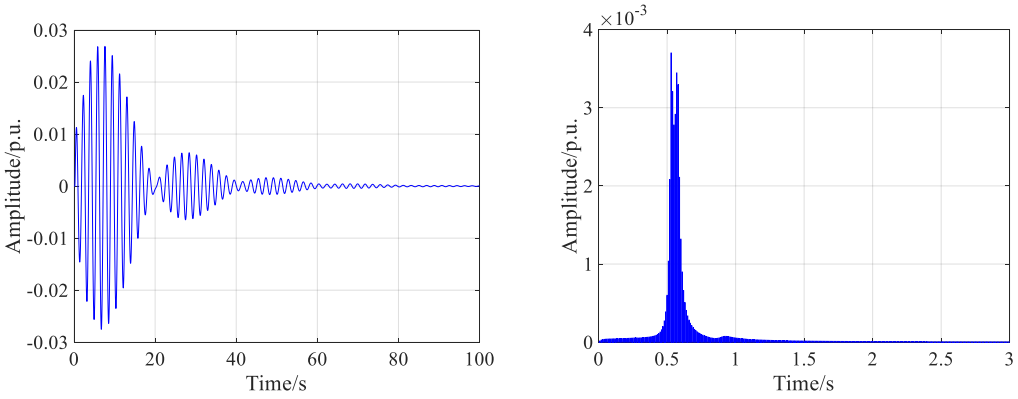

(a) (b)

Fig. 5.12. $\Delta V_{pq,i}(t)$ and its amplitude-characteristic in Scenario 5.5 in an FCWG-integrated 4M2A power system. (a). Plot of $\Delta V_{pq,i}(t)$ in time domain. (b). Amplitude-frequency characteristic of $\Delta V_{pq,i}(t)$ in frequency domain.

Table 5.6 Verification of EFA for estimating eigenvalues of interested GSOs in PLL in Scenario 5.5 of an FCWG-integrated 4M2A power system.

Interested mode	Real eigenvalue	Estimated eigenvalue
0.53 Hz (non-inherent GSO)	-0.0587±3.3252j	-0.0587±3.3301j
0.57 Hz (inherent GSO)	-0.0809±3.6269j	-0.0816±3.5814j

Through this scenario, the following conclusions can be summarized: when the frequency of the inherent GSO of PLL slightly exceeds that of the non-inherent GSO of PLL, the inherent GSO plays a negative role for the damping of the non-inherent

GSO. The generalized EFA is still perfect for the quantitative assessment.

When there is the resonance between the inherent GSO and the non-inherent GSO, the wind system operator should pay more attention to the oscillatory stability and modify the control parameters to consolidate the stability if necessary.

5.4.2 Application in a 16-machine 5-area Power System with a Full Converter-based Wind Generation

The line diagram of the 16M5A power system with an FCWG is illustrated in Fig. 5.13. The capacity of this FCWG is 1.0 MVA. The generators are all equipped with AVR but no PSS. The base capacity of this 16M5A power system is 100 MVA. The main parameters of control loops of GSC of FCWG are listed in the Appendix 5.4. A step-up disturbance happens to G_1 at 0.2 s and its mechanical power becomes 1.05 times of the original value, lasting for 0.1 s.

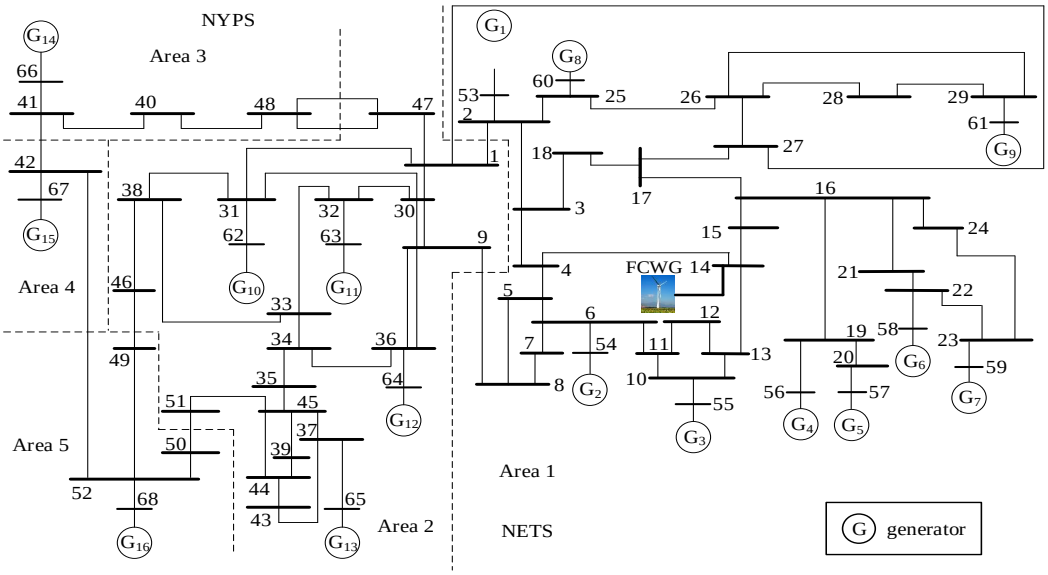

Fig. 5.13. Line diagram of a 16M5A power system with an FCWG.

It is assumed that the wind system operator is familiar with the frequencies of the

main EGOs. As discussed in Section 5.3, the open-loop analysis has very limited influence on the frequency (i.e. the imaginary part of the eigenvalue), which is suitable for the parameter setting to adjust the frequency of the inherent GSO. Thus, the resonance can be avoided by adjusting the integral time constant of the control loop of GSC.

In the case that the resonance cannot be avoided due to some reasons, the analysis of the virtual natural damping in Section 5.3 also provides the basis for the wind system operator to adjust the virtual natural damping of the inherent GSO to consolidate the stability.

Taking the PLL as an example, the real parts of eigenvalues and oscillation frequencies of the inherent and non-inherent GSOs observed in PLL are recorded as the case of no resonance in Table 5.7.

When the integral time constant of PLL changes from 43 to 12, there is an obvious resonance between the inherent and non-inherent GSOs of PLL, and their real parts of eigenvalues as well as oscillation frequencies are recorded as the case of with resonance & no PLL adjustment in Table 5.7. It can be seen that the damping of the inherent GSO of PLL decreases significantly compared with the case of no resonance. If the wind system operator wants to increase the damping of the inherent GSO of PLL to its original level, the wind system operator can adjust the proportional time constant of PLL from 0.12 to 0.17 to increase the virtual natural damping of the inherent GSO of PLL, and the results are recorded as the case of with resonance & PLL adjustment in Table 5.7.

Table 5.7 An example of application of generalized oscillation loop and EFA in PLL of an FCWG-integrated 16M5A power system for consolidating the stability.

Interested mode	No resonance		With resonance & no PLL adjustment		With resonance & PLL adjustment	
	Damping	Frequency	Damping	Frequency	Damping	Frequency
Inherent GSO	-0.0597	1.01 Hz	-0.0370	0.52 Hz	-0.0529	0.52 Hz
Non-inherent GSO	-0.1348	0.57 Hz	-0.1581	0.57 Hz	-0.1656	0.57 Hz

5.5 Summary

The key findings of this chapter are listed as follows: (1) when there is the resonance between the inherent and non-inherent GSOs of the DC capacitor voltage control loop or PLL, the inherent and non-inherent GSOs show the obvious modal influence between each other; (2) the quantitative assessment of the damping of inherent and non-inherent GSOs can be conducted with the help of the generalized EFA; and (3) with the help of the generalized oscillation loop, the oscillatory stability is consolidated by improving the virtual natural damping of the inherent GSO when the large-scale system model is unknown.

Chapter 6

Conclusions and Future Work

6.1 Conclusions

With the rapid development of various renewable power generations and emerging transmission technologies, the increasing number of PECs have penetrated to the power grid, which considerably complicates the dynamics and hence oscillations of the conventional power system. In order to investigate the emerging oscillation problems without the precise and high-dimensional modeling in the large-scale system, a measurement-based method (i.e., EFA) is systematically studied. The conclusions of this thesis are summarized as follows.

(1) DTA and EFA are derived to be essentially consistent. Specifically, the aggregated damping torque coefficient is newly defined and derived for DTA to characterize the integration effect of the damping contribution from the whole power system. Then, the pre-processing of measurements at the terminal of a local generator is conducted for EFA, and the frequency-decomposed energy attenuation coefficient is defined to screen and determine the damping contribution with respect to the frequency of interest. On this basis, the strict proof on the connection between DTA and EFA is carried out in assessing the damping performance of electromechanical oscillations of power systems, which is general for arbitrary models of synchronous generators in multi-machine power systems.

(2) A novel EFA is proposed with two implementation forms (i.e., TDI and FDI) to quantitatively investigate the electromechanical oscillation. For TDI, the new concept of the mode-screened damping torque coefficient with respect to an electromechanical oscillation mode is defined. For FDI, the Parseval's Theorem is applied to transform the proposed EFA from the time domain to frequency domain. On this basis, the connection between the proposed EFA and MA is essentially revealed in quantitatively investigating the electromechanical oscillation of the multi-machine power systems. The conclusion drawn is general to arbitrary models and parameters of synchronous generators. Hence, the proposed EFA indicates a prospect for the quantitative investigation of electromechanical oscillations in the large-scale multi-machine power systems without models.

(3) The proposed EFA in (2) is extended for quantitatively investigating MSOs of FCWG, and its consistency with MA is strictly revealed considering the arbitrary control schemes of FCWG in the multi-machine environment. On this basis, the extended EFA is applied to investigate the damping feature of multiple types of MSOs of FCWG in different scenarios through the case studies.

(4) With the help of the second-order differential operations in the studied control loop of PEC, a generalized oscillation loop is structured. Then, the proposed EFA in (2) is further generalized to quantitatively investigate various oscillations in the PEC-penetrated power systems. Taking the GSC of the FCWG system as an example, the generalized oscillation loop and generalized EFA are further demonstrated to investigate GSOs considering the potential resonance. The generalized oscillation loop

and generalized EFA have the prospect to consolidate the oscillatory stability of the large-scale PEC-penetrated power system when the system model is unknown.

The research in this thesis has the following practical values: (1) as any oscillation problem is essentially reflected by the dissipation of the oscillatory energy flow, the EFA can provide a clear physical understanding about the damping mechanism of oscillation modes; (2) the assessment is a model-free design based on WAMS and data analytics technique, which is suitable for the large-scale PEC-penetrated power system with unknown or changing internal control; and (3) the monitoring and analyzing technique only need the local information and hence is more efficient and reliable, which can easily coordinate with damping control strategies to mitigate the oscillations and align with the system development trend.

The social influence is summarized as follows: (1) the research in this thesis is beneficial to both the stable power grid operation and sustainable development, which is crucial to the modern society; and (2) this thesis can further increase the development of renewable generations and new transmission technologies.

6.2 Future Work

This thesis has proposed a series of EFA theories to investigate the various oscillations of PEC-penetrated power systems. To make the current work more comprehensive, the following work can be conducted in the future.

(1) The proposed EFA theories can be applied to more types of renewable power generation systems, such as the doubly fed induction generator-based wind farm and

photovoltaic power generation system.

(2) The proposed EFA theories can be further tested in the new transmission technologies-integrated power system to deal with more kinds of emerging oscillation problems.

(3) The proposed EFA theories can be tested in the time sequential simulation. On this basis, the planning and operation strategies can be proposed for the modern power grid with the integration of renewable power generations and new transmission technologies.

Appendix

A.1 Models and Parameter Settings in Case Studies of Chapter 2

The 6th-order model of synchronous generators is given by (A.1). The transfer functions of AVR and PSS of the *i*-th generator are shown in Fig. A.1.

$$\begin{cases} \dfrac{\mathrm{d}\delta_i(t)}{\mathrm{d}t} = \omega_0\left(\omega_i(t)-1\right) \\ \dfrac{\mathrm{d}\omega_i(t)}{\mathrm{d}t} = \dfrac{1}{T_{J,i}}\left(P_{m,i}(t)-P_{e,i}(t)-D_i\left(\omega_i(t)-1\right)\right) \\ \dfrac{\mathrm{d}E'_{q,i}(t)}{\mathrm{d}t} = \dfrac{1}{T'_{d0,i}}\left(-E_{q,i}(t)+E_{fd,i}(t)\right) \\ \dfrac{\mathrm{d}E'_{fd,i}(t)}{\mathrm{d}t} = \dfrac{1}{T_{a,i}}\left(-E'_{fd,i}(t)+K_{a,i}\left(V_{tref,i}-V_{t,i}(t)+u_{pss,i}(t)\right)\right) \\ \dfrac{\mathrm{d}Y_i(t)}{\mathrm{d}t} = \dfrac{\left(\omega_i(t)-1\right)+T_{4,i}\dfrac{\mathrm{d}\omega_i(t)}{\mathrm{d}t}-Y_i(t)}{T_{3,i}} \\ \dfrac{\mathrm{d}u_{pss,i}(t)}{\mathrm{d}t} = \dfrac{K_{pss,i}Y_i(t)+K_{pss,i}T_{2,i}\dfrac{\mathrm{d}Y_i(t)}{\mathrm{d}t}-u_{pss,i}(t)}{T_{1,i}} \end{cases} \tag{A.1}$$

where $T'_{d0,i}$ denotes the time constant of the field winding of the *i*-th generator; $E_{q,i}(t)$ denotes the *q*-axis excitation voltage of the *i*-th generator; $E_{fd,i}(t)$ denotes the excitation voltage of the *i*-th generator; $E'_{fd,i}(t)$ denotes the transient excitation voltage of the *i*-th generator; $V_{t,i}(t)$ denotes the output voltage of the *i*-th generator; $V_{tref,i}$ is the output voltage reference of the *i*-th generator; $u_{pss,i}(t)$ denotes the stabilizing signal of PSS of the *i*-th generator; $K_{a,i}$ is the gain of AVR of the *i*-th generator; $T_{a,i}$ is the time constant of AVR of the *i*-th generator; $Y_i(t)$ is the intermediate variable of the *i*-th generator; $K_{pss,i}$ is the proportional coefficient of PSS of the *i*-th generator; and $T_{1,i}$, $T_{2,i}$,$T_{3,i}$ and

$T_{4,i}$ are the time constants of PSS of the i-th generator.

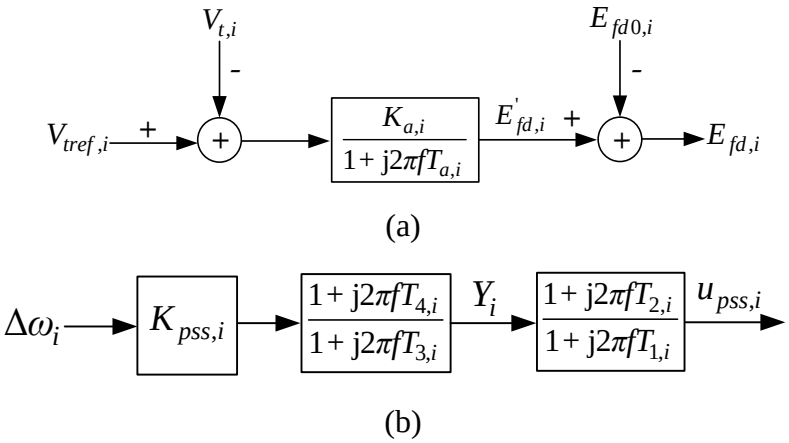

Fig. A.1. Transfer functions of AVR and PSS of the i-th generator under the Fourier analysis. (a) Transfer function of AVR. (b) Transfer function of PSS.

The parameters in the SMIB power system are listed as follows.

T_J=8.0 s; D=0; ω_0=314.0 rad/s; T'_{d0}=5.0 s;

X_d=0.8 p.u.; X_q=0.4 p.u.; X'_d=0.05 p.u.; P_{m0}=0.6 p.u.;

X_t=0.3 p.u.; V_1=V_t=1.05 p.u.; V_2=1.0 p.u.; V_{tref}=1.05 p.u.;

K_a=10.0; T_a=0.01 s; K_{pss}=0; T_2=T_4=0; and T_1=T_3=9999.

where X_d is the d-axis synchronous reactance; X_q is the q-axis synchronous reactance; X'_d is the d-axis transient reactance; V_1 and V_2 are the voltage at nodes 1 and 2; X_t is the reactance of the transmission line and transformer; P_{m0} is the initial mechanical power; the meanings of other parameters have been given in (2.1) and (A.1).

The parameters in the 4M2A power system are listed as follows.

$T_{J,1}$=$T_{J,2}$=117.0 s; $T_{J,3}$=$T_{J,4}$=111.15 s; D_1=D_2=D_3=D_4=0;

$\omega_{0,1}$=$\omega_{0,2}$=$\omega_{0,3}$=$\omega_{0,4}$=314.0 rad/s; $P_{m0,1}$=8.67 p.u.;

$P_{m0,2}$=$P_{m0,3}$=$P_{m0,4}$=7.0 p.u.; $X_{d,1}$=$X_{d,2}$=$X_{d,3}$=$X_{d,4}$=0.2 p.u.;

$X_{q,1}$=$X_{q,2}$=$X_{q,3}$=$X_{q,4}$=0.1889 p.u.; $X'_{d,1}$=$X'_{d,2}$=$X'_{d,3}$=$X'_{d,4}$=0.0333 p.u.;

$T'_{d0,1}$=$T'_{d0,2}$=$T'_{d0,3}$=$T'_{d0,4}$=8.0 s; $V_{t,1}$=$V_{t,3}$=1.03 p.u.;

$V_{t,2}$=$V_{t,4}$=1.01 p.u.; $V_{tref,1}$=$V_{tref,3}$=1.03 p.u.; $V_{tref,2}$=$V_{tref,4}$=1.01 p.u.;

X_{15}=X_{36}=X_{29}=X_{48}=0.0167 p.u.; X_{56}=X_{89}=0.025 p.u.;

X_{67}=X_{78}=0.055 p.u.; P_{load6}=9.67 p.u.; Q_{load6}=1.00 p.u.;

P_{load8}=20.0 p.u.; Q_{load8}=1.0 p.u.; Q_{c6}=-2.0 p.u.; Q_{c8}=-3.5 p.u.

where X_{15}, X_{36}, X_{29}, X_{48}, X_{56}, X_{89}, X_{67}, and X_{78} are the reactance of transmission lines and transformers of this 4M2A power system; P_{load6}, Q_{load6}, P_{load8}, and Q_{load8} are the active power and reactive power of loads in this 4M2A power system; and Q_{c6} and Q_{c8} are the reactive power compensation at loads.

A.2 Parameter Settings in Case Studies of Chapter 3

The parameters of generators in the 4M2A power system are listed as follows.

$T_{J,1}$=$T_{J,2}$=117.0 s; $T_{J,3}$=$T_{J,4}$=111.15 s; D_1=D_2=D_3=D_4=0;

$K_{a,1}$=$K_{a,2}$=$K_{a,3}$=$K_{a,4}$=65.0; $T_{a,1}$=$T_{a,2}$=$T_{a,3}$=$T_{a,4}$=0.1 s;

$K_{pss,1}$=$K_{pss,2}$=$K_{pss,3}$=$K_{pss,4}$=8.5; $T_{1,1}$=$T_{1,2}$=$T_{1,3}$=$T_{1,4}$=5.5 s;

$T_{2,1}$=$T_{2,2}$=$T_{2,3}$=$T_{2,4}$=3.5 s; $T_{3,1}$=$T_{3,2}$=$T_{3,3}$=$T_{3,4}$=5.5 s;

$T_{4,1}$=$T_{4,2}$=$T_{4,3}$=$T_{4,4}$=3.5 s; $P_{m,1}$=8.67 p.u.; $P_{m,2}$=$P_{m,3}$=$P_{m,4}$=7.0 p.u.

The parameters of generators in the 16M5A power system are listed as follows.

$T_{J,1}$=42.0 s; $T_{J,2}$=30.2 s; $T_{J,3}$=35.8 s; $T_{J,4}$=28.6 s; $T_{J,5}$=26.0 s;

$T_{J,6}$=34.8 s; $T_{J,7}$=26.4 s; $T_{J,8}$=24.3 s; $T_{J,9}$=34.5 s; $T_{J,10}$=31.0 s;

$T_{J,11}$=28.2 s; $T_{J,12}$=92.3 s; $T_{J,13}$=496.0 s; $T_{J,14}$=$T_{J,15}$=300.0 s;

$T_{J,16}$=450.0 s; D_1~D_{16}=0; $K_{a,1}$~$K_{a,16}$=3.95, $T_{a,1}$~$T_{a,16}$=0.1 s;

$K_{pss,1}$~$K_{pss,16}$=0, $T_{1,1}$~$T_{1,16}$=9999 s; $T_{2,1}$~$T_{2,16}$=0 s;

$T_{3,1}$~$T_{3,16}$=9999 s; $T_{4,1}$~$T_{4,16}$=0 s; $P_{m,1}$=2.5 p.u.; $P_{m,2}$=5.45 p.u.;

$P_{m,3}$=6.5 p.u.; $P_{m,4}$=6.32 p.u.; $P_{m,5}$=5.052 p.u.; $P_{m,6}$=7.0 p.u.;

$P_{m,7}$=5.6 p.u.; $P_{m,8}$=5.4 p.u.; $P_{m,9}$=8.0 p.u.; $P_{m,10}$=5.0 p.u.;

$P_{m,11}$=10.0 p.u.; $P_{m,12}$=13.5 p.u.; $P_{m,13}$=36.1258 p.u.;

$P_{m,14}$=17.85 p.u.; $P_{m,15}$=10.0 p.u.; $P_{m,16}$=40.0 p.u.

A.3 Parameter Settings in Case Studies of Chapter 4

The parameters of PMSG in the SMIB power system are as follows.

$P_{pm,1}$=1.0 p.u.; $H_{pr,1}$=8.0 s; $X_{pd,1}$=0.2 p.u.; $X_{pq,1}$=0.2 p.u.; $X_{pf,1}$=0.02 p.u.

where $X_{pd,1}$ is the *d*-axis reactance of the stator winding; $X_{pq,1}$ is the *q*-axis reactance of the stator winding; and $X_{pf,1}$ is the filter reactance.

The parameters of MSC in the SMIB power system are as follows.

$K_{pp\text{-}wt,1}$=1.25; $K_{p\text{-}wt,1}$=70.0; $K_{pp\text{-}iq,1}$=0.08; $K_{p\text{-}iq,1}$=30.0;

$K_{pp\text{-}id,1}$=1.01; $K_{p\text{-}id,1}$=10.0

The parameters of the conventional synchronous generator in the SMIB power system are as follows. The meanings of variables can be found in the Appendix A.1, which are not repeated here.

T_J=8.0 s; D=0; ω_0=314.0 rad/s; T'_{d0}=5.0 s; X_d=0.8 p.u.; X_q=0.4 p.u.;

X'_d=0.05 p.u.; P_{m0}=0.6 p.u.

The parameters of PMSG in the 4M2A power system are as follows.

$P_{pm,1}$=1.0 p.u.; $H_{pr,1}$=8.0 s; $X_{pd,1}$=0.2 p.u.; $X_{pq,1}$=0.2 p.u.; $X_{pf,1}$=0.02 p.u.

The parameters of MSC in Scenarios 4.1-4.3 of the 4M2A power system are as follows.

$K_{pp\text{-}wt,1}$=1.05; $K_{p\text{-}wt,1}$=50.0; $K_{pp\text{-}iq,1}$=0.07; $K_{p\text{-}iq,1}$=20.0; $K_{pp\text{-}id,1}$=0.04; $K_{p\text{-}id,1}$=30.0

The parameters of MSC in Scenario 4.4 of the 4M2A power system are as follows.

$K_{pp\text{-}wt,1}$=1.05; $K_{p\text{-}wt,1}$=92.0; $K_{pp\text{-}iq,1}$=0.07; $K_{p\text{-}iq,1}$=20.0; $K_{pp\text{-}id,1}$=0.04; $K_{p\text{-}id,1}$=30.0

The parameters of ARC in the 4M2A power system are as follows:

T_1=0.3 s; T_2=0.03 s; T_3=0.3 s; T_4=0.03 s; T_W=0.05 s; K_W=0.8

The parameters of conventional synchronous generators in the 4M2A power system are as follows.

$T_{J,1}$=$T_{J,2}$=117.0 s; $T_{J,3}$=$T_{J,4}$=111.15 s; D_1=D_2=D_3=D_4=0;

ω_0=314.0 rad/s; $T'_{d0,1}$=$T'_{d0,2}$=$T'_{d0,3}$=$T'_{d0,4}$=8.0 s;

$X_{d,1}$=$X_{d,2}$=$X_{d,3}$=$X_{d,4}$=0.2 p.u.; $X_{q,1}$=$X_{q,2}$=$X_{q,3}$=$X_{q,4}$=0.1889 p.u.;

$X'_{d,1}$=$X'_{d,2}$=$X'_{d,3}$=$X'_{d,4}$=0.0333 p.u.; $P_{m0,1}$=6.0 p.u.;

$P_{m0,3}$=7.5 p.u.; $P_{m0,2}$=$P_{m0,4}$=7.0 p.u.

A.4 Parameter Settings in Case Studies of Chapter 5

The parameters of GSC of FCWG in the 4M2A power system are listed as follows.

$K_{pp5,1}$=0.5; $K_{pi5,1}$=100; $K_{pp6,1}$=1.0; $K_{pi6,1}$=10.0; $K_{pp7,1}$=0.5; $K_{pi7,1}$=100.0;

Scenario 5.1: $K_{pp4,1}$=1.0; $K_{pi4,1}$=90.0; $K_{ppll,1}$=0.12; $K_{ipll,1}$=39.27;

Scenario 5.2: $K_{pp4,1}$=1.0; $K_{pi4,1}$=260.0; $K_{ppll,1}$=0.12; $K_{ipll,1}$=39.27;

Scenario 5.3: $K_{pp4,1}$=1.0; $K_{pi4,1}$=400.0; $K_{ppll,1}$=0.12; $K_{ipll,1}$=39.27;

Scenario 5.4: $K_{pp4,1}$=1.0; $K_{pi4,1}$=90.0; $K_{ppll,1}$=0.12; $K_{ipll,1}$=9.0;

Scenario 5.5: $K_{pp4,1}$=1.0; $K_{pi4,1}$=90.0; $K_{ppll,1}$=0.12; $K_{ipll,1}$=13.0

The parameters of GSC of FCWG in the 16M5A power system are listed as follows.

$K_{pp4,1}$=0.5; $K_{pi4,1}$=20.0; $K_{pp5,1}$=0.2; $K_{pi5,1}$=80.0; $K_{pp6,1}$=3.1; $K_{pi6,1}$=10.0;

$K_{pp7,1}$=0.5; $K_{pi7,1}$=50.0; $K_{ppll,1}$=0.12; $K_{ipll,1}$=43.0

References

[1] S. Su, Y. Hu, T. Yang, S. Wang, Z. Liu, X. Wei, M. Xia, Y. Ota, and K. Yamashita, "Research on an electric vehicle owner-friendly charging strategy using photovoltaic generation at office sites in major Chinese cities," *Energies*, vol. 11, no. 2, p. 421, Feb. 2018.

[2] D. Solatialkaran, F. Zare, T. K. Saha, and R. Sharma, "A novel approach in filter design for grid-connected inverters used in renewable energy systems," *IEEE Transactions on Sustainable Energy*, vol. 11, no. 1, pp. 154 - 164, Jan. 2020.

[3] S. Su, Y. Hu, L. He, K. Yamashita, and S. Wang, "An assessment procedure of distribution network reliability considering photovoltaic power integration," *IEEE Access*, vol. 7, pp. 60171-60185, May 2019.

[4] D. Kumar, V. Gupta, and R. C. Jha, "Implementation of FACTS devices for improvement of voltage stability using evolutionary algorithm," in *2016 IEEE 1st International Conference on Power Electronics, Intelligent Control and Energy Systems (ICPEICES)*, Delhi, India, Jul. 2016, pp. 1-6.

[5] M. Mehrasa, E. Pouresmaeil, S. Zabihi, and J. P. Catalão, "Dynamic model, control and stability analysis of MMC in HVDC transmission systems," *IEEE Transactions on Power Delivery*, vol. 32, no. 3, pp. 1471-1482, Jun. 2017.

[6] Y. Hu, S. Su, L. He, X. Wu, T. Ma, Z. Liu, and X. Wei, "A real-time multilevel energy management strategy for electric vehicle charging in a smart electric energy distribution system," *Energy Technology*, vol. 7, no. 5, p. 1800705, May 2019.

[7] Y. Cheng and C. Zhang, "Configuration and operation combined optimization for EV battery swapping station considering PV consumption bundling," *Protection and Control of Modern Power Systems*, vol. 2, no. 1, p. 26, Jul. 2017.

[8] M. Zhao, X. Yuan, J. Hu, and Y. Yan, "Voltage dynamics of current control time-scale in a VSC-connected weak grid," *IEEE Transactions on Power Systems*, vol. 31, no. 4, pp. 2925-2937, Jul. 2016.

[9] M. F. Firuzi, A. Roosta, and M. Gitizadeh, "Stability analysis and decentralized control of inverter-based ac microgrid," *Protection and Control of Modern Power Systems*, vol. 4, no. 1, p. 6, Mar. 2019.

[10] J. Khazaei, Z. Miao, and L. Piyasinghe, "Impedance-model-based MIMO analysis of power synchronization control," *Electric Power Systems Research*, vol. 154, pp. 341-351, Jan. 2018.

[11] J. Shair, H. Li, J. Hu, and X. Xie, "Power system stability issues, classifications and research prospects in the context of high-penetration of renewables and power electronics," *Renewable and Sustainable Energy Reviews*, vol. 145, p. 111111, Jul. 2021.

[12] G. Magdy, G. Shabib, A. A. Elbaset, and Y. Mitani, "Optimized coordinated control of LFC and SMES to enhance frequency stability of a real multi-source power system considering high renewable energy penetration," *Protection and Control of Modern Power Systems*, vol. 3, no. 1, p. 39, Dec. 2018.

[13] Z. Ma, H. Chen, and Y. Chai, "Analysis of voltage stability uncertainty using stochastic response surface method related to wind farm correlation," *Protection and Control of Modern Power Systems*, vol. 2, no. 1, p. 20, May 2017.

[14] J. Chen, X. Li, M. A. Mohamed, and T. Jin, "An adaptive matrix pencil algorithm based-wavelet soft-threshold denoising for analysis of low frequency oscillation in power systems," *IEEE Access*, vol. 8, pp. 7244–7255, Jan. 2020.

[15] A. Salgotra and S. Pan, "Model based PI power system stabilizer design for damping low frequency oscillations in power systems," *ISA Transactions*, vol. 76, pp. 110–121, May 2018.

[16] D. V. Nair and M. Murty, “Reconfigurable control as actuator fault-tolerant control design for power oscillation damping,” *Protection and Control of Modern Power Systems*, vol. 5, no. 1, pp. 1–12, Feb. 2020.

[17] K. Gu, F. Wu, and X.-P. Zhang, “Sub-synchronous interactions in power systems with wind turbines: a review,” *IET Renewable Power Generation,* vol. 13, no. 1, pp. 4-15, Jan. 2019.

[18] H. Ghasemi, G. Gharehpetian, S. A. Nabavi-Niaki, and J. Aghaei, “Overview of subsynchronous resonance analysis and control in wind turbines,” *Renewable and Sustainable Energy Reviews,* vol. 27, pp. 234-243, Nov. 2013.

[19] H. Liu, X. Xie, Y. Li, H. Liu, and Y. Hu, “A small-signal impedance method for analyzing the SSR of series-compensated DFIG-based wind farms,” in *2015 IEEE Power & Energy Society General Meeting*, Denver, CO, USA, Jul. 2015, pp. 1-5.

[20] L. Fan, R. Kavasseri, Z. L. Miao, and C. Zhu, “Modeling of DFIG-based wind farms for SSR analysis,” *IEEE Transactions on Power Delivery*, vol. 25, no. 4, pp. 2073-2082, Oct. 2010.

[21] H. Liu, X. Xie, Y. Li, H. Liu, and Y. Hu, “Mitigation of SSR by embedding subsynchronous notch filters into DFIG converter controllers,” *IET Generation, Transmission & Distribution*, vol. 11, no. 11, pp. 2888-2896, Aug. 2017.

[22] Y. Xu and Y. Cao, “Sub-synchronous oscillation in PMSGs based wind farms caused by amplification effect of GSC controller and PLL to harmonics,” *IET Renewable Power Generation*, vol. 12, no. 7, pp. 844-850, May 2018.

[23] Z. Zheng, Z. An, and C. Shen, “Evaluation method for equivalent models of PMSG-based wind farms considering randomness,” *IEEE Transactions on Sustainable Energy*, vol. 10, no. 3, pp. 1565 - 1574, Jul. 2019.

[24] “IEEE IBR SSO Taskforce.” Available: https://sites.google.com/view/windsso/home (accessed Aug. 28, 2022)

[25] “IEEE PES Task Force on Oscillation Source Location.” Available: http://web.eecs.utk.edu/~kaisun/TF/index.html. (accessed Aug. 28, 2022)

[26] “Recent Research Results at USF on Wind Integration System Oscillation Issues.” Available: https://drive.google.com/file/d/1D3N_J1YpuhdQw4B-QHrjQRR6v4wm6kFx/view. (accessed Aug. 28, 2022)

[27] I. S. R. W. Group, “Reader’s guide to subsynchronous resonance,” *IEEE Transactions on Power Systems*, vol. 7, no. 1, pp. 150-157, Feb. 1992.

[28] L. Wang, X. Xie, H. Liu, Y. Zhan, J. He, and C. Wang, “Review of emerging SSR/SSO issues and their classifications,” *The Journal of Engineering*, vol. 2017, no. 13, pp. 1666-1670, Jan. 2018.

[29] X. Xie, X. Zhang, H. Liu, H. Liu, Y. Li, and C. Zhang, “Characteristic analysis of subsynchronous resonance in practical wind farms connected to series-compensated transmissions,” *IEEE Transactions on Energy Conversion*, vol. 32, no. 3, pp. 1117-1126, Sep. 2017.

[30] J. Chen, P. Shrestha, S.-H. Huang, N. Sarma, J. Adams, D. Obadina, and J. Ballance, “Use of synchronized phasor measurements for dynamic stability monitoring and model validation in ERCOT,” in *2012 IEEE Power and Energy Society General Meeting*, San Diego, CA, USA, Jul. 2012, pp. 1-7.

[31] J. Ma, P. Zhang, H.-j. Fu, B. Bo, and Z.-y. Dong, “Application of phasor measurement unit on locating disturbance source for low-frequency oscillation,” *IEEE Transactions on Smart Grid*, vol. 1, no. 3, pp. 340-346, Dec. 2010.

[32] S. A. N. Sarmadi and V. Venkatasubramanian, “Inter-area resonance in power systems from forced oscillations,” *IEEE Transactions on Power Systems*, vol. 31, no. 1, pp. 378-386, Jan. 2016.

[33] H. Hu, Y. Zhou, X. Li, and K. Lei, “Low-frequency oscillation in electric railway depot: A comprehensive review,” *IEEE Transactions on Power Electronics*, vol. 36, no. 1, pp. 295–314, Jan. 2021.

[34] L. Huang, H. Xin, and Z. Wang, “Damping low-frequency oscillations through VSC-HVDC stations operated as virtual synchronous machines,” *IEEE Transactions on Power Electronics*, vol. 34, no. 6, pp. 5803–5818, Jun. 2019.

[35] Y. Hashmy, Z. Yu, D. Shi, and Y. Weng, “Wide-area measurement system-based low frequency oscillation damping control through reinforcement learning,” *IEEE Transactions on Smart Grid*, vol. 11, no. 6, pp. 5072–5083, Nov. 2020.

[36] X. Zhang, C. Lu, S. Liu, and X. Wang, “A review on wide-area damping control to restrain inter-area low frequency oscillation for large-scale power systems with increasing renewable generation,” *Renewable and Sustainable Energy Reviews*, vol. 57, pp. 45-58, May 2016.

[37] B. Dasu, M. Sivakumar, and R. Srinivasarao, “Interconnected multi-machine power system stabilizer design using whale optimization algorithm,” *Protection and Control of Modern Power Systems*, vol. 4, no. 1, pp. 1–11, Feb. 2019.

[38] C. Li, W. Zhang, and R. Liu, “Forced low frequency oscillation of wind-integrated power systems,” in *2016 IEEE Power & Energy Society Innovative Smart Grid Technologies Conference (ISGT)*, Minneapolis, MN, Sep. 2016, pp. 1–5.

[39] Y. Liao, Z. Liu, H. Zhang, and B. Wen, “Low-frequency stability analysis of single-phase system with dq-frame impedance approach-part II: stability and frequency analysis,” *IEEE Transactions on Industry Applications*, vol. 54, no. 5, pp. 5012-5024, Sep. 2018.

[40] Z. Liu, G. Zhang, and Y. Liao, “Stability research of high-speed railway EMUs and traction network cascade system considering impedance matching,” *IEEE Transactions on Industry Applications*, vol. 52, no. 5, pp. 4315-4326, Sep. 2016.

[41] W. Du, Q. Fu, and H. F. Wang, “Power system small-signal angular stability affected by virtual synchronous generators,” *IEEE Transactions on Power Systems*, vol. 34, no. 4, pp. 3209–3219, Jul. 2019.

[42] Y. Zhan, X. Xie, H. Liu, H. Liu, and Y. Li, "Frequency-domain modal analysis of the oscillatory stability of power systems with high-penetration renewables," *IEEE Transactions on Sustainable Energy*, vol. 10, no. 3, pp. 1534–1543, Jul. 2019.

[43] J. L. Rueda, J. C. Cepeda, I. Erlich, A. W. Korai, and F. M. Gonzalez-Longatt, "Probabilistic approach for risk evaluation of oscillatory stability in power systems," in *Power Factory Applications for Power System Analysis*. Switzerland: Springer Cham, 2014, pp. 249-266.

[44] J. Shair, X. Xie, and G. Yan, "Mitigating subsynchronous control interaction in wind power systems: existing techniques and open challenges," *Renewable and Sustainable Energy Reviews,* vol. 108, pp. 330-346, Jul. 2019.

[45] R. Shah, N. Mithulananthan, and R. Bansal, "Oscillatory stability analysis with high penetrations of large-scale photovoltaic generation," *Energy Conversion and Management,* vol. 65, pp. 420-429, Jan. 2013.

[46] J. Xu, P. K. Kanyingi, K. Wang, G. Li, B. Han, and X. Jiang, "Probabilistic small signal stability analysis with large scale integration of wind power considering dependence," *Renewable and Sustainable Energy Reviews*, vol. 69, pp. 1258-1270, Mar. 2017.

[47] R. K. Varma and M. Akbari, "Simultaneous fast frequency control and power oscillation damping by utilizing PV solar system as PV-STATCOM," *IEEE Transactions on Sustainable Energy*, vol. 11, no. 1, pp. 415–425, Jan. 2020.

[48] G. Zhang, W. Hu, D. Cao, Q. Huang, J. Yi, Z. Chen, and F. Blaabjerg, "Deep reinforcement learning-based approach for proportional resonance power system stabilizer to prevent ultra-low-frequency oscillations," *IEEE Transactions on Smart Grid*, vol. 11, no. 6, pp. 5260–5272, Nov. 2020.

[49] D. Chitara, K. R. Niazi, A. Swarnkar, and N. Gupta, "Cuckoo search optimization algorithm for designing of a multimachine power system

stabilizer," *IEEE Transactions on Industry Applications,* vol. 54, no. 4, pp. 3056–3065, Jul. 2018.

[50] C. H. N. S. Kalyan, and G. S. Rao, "Impact of communication time delays on combined LFC and AVR of a multi-area hybrid system with IPFC-RFBs coordinated control strategy," *Protection and Control of Modern Power Systems*, vol. 6, no. 1, pp. 1–20, Mar. 2021.

[51] G. Gurrala and I. Sen, "Power system stabilizers design for interconnected power systems," *IEEE Transactions on Power Systems*, vol. 25, no. 2, pp. 1042–1051, May 2010.

[52] H. Wang and W. Du, *Analysis and Damping Control of Power System Low-frequency Oscillations*. New York, US: Springer, 2016.

[53] J. Bi, H. Sun, S. Xu, R. Song, B. Zhao, and Q. Guo, "Mode-based damping torque analysis method in power system low-frequency oscillations," *CSEE Journal of Power and Energy Systems,* Early Access, Oct. 2020.

[54] S. Q. Bu, X. Zhang, J. B. Zhu, and X. Liu, "Comparison analysis on damping mechanisms of power systems with induction generator based wind power generation," *International Journal of Electrical Power & Energy Systems*, vol. 97, pp. 250–261, Apr. 2018.

[55] S. W. Xia, S. Q. Bu, X. Zhang, Y. Xu, B. Zhou, and J. B. Zhu, "Model reduction strategy of doubly-fed induction generator-based wind farms for power system small-signal rotor angle stability analysis," *Applied Energy*, vol. 222, pp. 608–620, Jul. 2018.

[56] S. Bu, W. Du, and H. Wang, "Model validation of DFIGs for power system oscillation stability analysis," *IET Renewable Power Generation*, vol. 11, no. 6, pp. 858–866, May 2017.

[57] F. J. Swift and H. F. Wang, "The connection between modal analysis and electric torque analysis in studying the oscillation stability of multi-machine

power systems," *International Journal of Electrical Power & Energy Systems*, vol. 19, no. 5, pp. 321–330, Jun. 1997.

[58] W. Du, J. Bi, C. Lv, and T. Littler, "Damping torque analysis of power systems with DFIGs for wind power generation," *IET Renewable Power Generation*, vol. 11, no. 1, pp. 10–19, Jan. 2017.

[59] W. Du, X. Chen, and H. F. Wang, "Power system electromechanical oscillation modes as affected by dynamic interactions from grid-connected PMSGs for wind power generation," *IEEE Transactions on Sustainable Energy*, vol. 8, no. 3, pp. 1301–1312, Jul. 2017.

[60] Y. Ge, W. Du, T. Littler, and S. Q. Bu, "Damping torque analysis of AVR in large-scale multi-machine power systems," in *2nd IET Renewable Power Generation Conference*, Beijing, China, Sep. 2013, pp. 1-4.

[61] J. Seppanen, S.-K. Au, J. Turunen, and L. Haarla, "Bayesian approach in the modal analysis of electromechanical oscillations," *IEEE Transactions on Power Systems*, vol. 32, no. 1, pp. 316–325, Jan. 2017.

[62] S. Rezaee, A. Radwan, M. Moallem, and J. Wang, "Voltage source converters connected to very weak grids: Accurate dynamic modeling, small-signal analysis, and stability improvement," *IEEE Access*, vol. 8, pp. 201120–201133, Nov. 2020.

[63] J. L. Domínguez-García, O. Gomis-Bellmunt, F. D. Bianchi, and A. Sumper, "Power oscillation damping supported by wind power: a review," *Renewable and Sustainable Energy Reviews*, vol. 16, no. 7, pp. 4994-5006, Sep. 2012.

[64] R. Shah, N. Mithulananathan, and K. Y. Lee, "Design of robust power oscillation damping controller for large-scale PV plant," in *2012 IEEE Power and Energy Society General Meeting*, San Diego, CA, USA, Jul. 2012, pp. 1-8.

[65] M. Wu, L. Xie, L. Cheng, and R. Sun, "A study on the impact of wind farm spatial distribution on power system sub-synchronous oscillations," *IEEE Transactions on Power Systems*, vol. 31, no. 3, pp. 2154-2162, May 2016.

[66] A. M. Vural, “Contribution of high voltage direct current transmission systems to inter-area oscillation damping: A review,” *Renewable and Sustainable Energy Reviews,* vol. 57, pp. 892-915, May 2016.

[67] H. Hasanvand, M. R. Arvan, B. Mozafari, and T. Amraee, “Coordinated design of PSS and TCSC to mitigate interarea oscillations,” *International Journal of Electrical Power & Energy Systems,* vol. 78, pp. 194-206, Jun. 2016.

[68] W. Du, H. Wang, and S. Bu, *Small-Signal Stability Analysis of Power Systems Integrated with Variable Speed Wind Generators*. Cham, Switzerland: Springer, 2018.

[69] T. Zhou, Z. Chen, S. Bu, H. Tang, and Y. Liu, “Eigen-analysis considering time-delay and data-loss of WAMS and ITS application to WADC design based on damping torque analysis,” *Energies,* vol. 11, no. 11, p. 3186, Nov. 2018.

[70] M. Amin and M. Molinas, “Small-signal stability assessment of power electronics based power systems: a discussion of impedance-and eigenvalue-based methods,” *IEEE Transactions on Industry Applications,* vol. 53, no. 5, pp. 5014-5030, Sep. 2017.

[71] L. Chen, F. Xu, Y. Min, M. Wang, and W. Hu, “Transient energy dissipation of resistances and its effect on power system damping,” *International Journal of Electrical Power & Energy Systems,* vol. 91, pp. 201–208, Oct. 2017.

[72] W. Du, X. Chen, and H. F. Wang, “Impact of dynamic interactions introduced by the DFIGs on power system electromechanical oscillation modes,” *IEEE Transactions on Power Systems,* vol. 32, no. 6, pp. 4954–4967, Nov. 2017.

[73] J. Luo, S. Bu, and F. Teng, “An optimal modal coordination strategy based on modal superposition theory to mitigate low frequency oscillation in FCWG penetrated power systems,” *International Journal of Electrical Power & Energy Systems,* vol. 120, p. 105975, Sep. 2020.

[74] Z. Zhu, G. Geng, and Q. Jiang, “Power system dynamic model reduction based on extended Krylov subspace method,” *IEEE Transactions on Power Systems*, vol. 31, no. 6, pp. 4483–4494, Nov. 2016.

[75] Y. Yang, J. Zhao, H. Liu, Z. Qin, J. Deng, and J. Qi, “A matrix-perturbation-theory-based optimal strategy for small-signal stability analysis of large-scale power grid,” *Protection and Control of Modern Power Systems*, vol. 3, no. 1, pp. 1–11, Nov. 2018.

[76] S. Q. Bu, X. Zhang, S. W. Xia, Y. Xu, B. Zhou, and X. Lu, “Reducing model complexity of DFIG-based wind turbines to improve the efficiency of power system stability analysis,” *Energy Procedia*, vol. 142, pp. 971-976, Dec. 2017.

[77] C. Chen, W. Du, H. Wang, and T. Littler, “Sub-synchronous oscillations in power systems caused by grid-connected wind farms-A survey of mechanism studies,” *CSEE Journal of Power and Energy Systems*, vol. 4, no. 4, pp. 495-503, Dec. 2018.

[78] J. Sun, M. Li, Z. Zhang, T. Xu, J. He, H. Wang, and G. Li, “Renewable energy transmission by HVDC across the continent: System challenges and opportunities,” *CSEE Journal of Power and Energy Systems*, vol. 3, no. 4, pp. 353-364, Dec. 2017.

[79] H. Silva-Saravia, Y. Wang, H. Pulgar-Painemal, and K. Tomsovic, “Oscillation energy based sensitivity analysis and control for multi-mode oscillation systems,” in *2018 IEEE Power & Energy Society General Meeting*, Portland, OR, USA, Aug. 2018, pp. 1-5.

[80] L. G. Meegahapola, S. Bu, D. P. Wadduwage, C. Y. Chung, and X. Yu, “Review on oscillatory stability in power grids with renewable energy sources: Monitoring, analysis, and control using synchrophasor technology,” *IEEE Transactions on Industrial Electronics*, vol. 68, no. 1, pp. 519–531, Jan. 2021.

[81] J. Zhao, Y. Zhang, P. Zhang, X. Jin, and C. Fu, “Development of a WAMS based test platform for power system real time transient stability detection and

control," *Protection and Control of Modern Power Systems*, vol. 1, no. 1, pp. 1–11, Jun. 2016.

[82] X. Wu, X. Chen, M. Shahidehpour, Q. Zhou, and L. Fan, "Distributed cooperative scheme for forced oscillation location identification in power systems," *IEEE Transactions on Power Systems*, vol. 35, no. 1, pp. 374–384, Jan. 2020.

[83] Y. Yu, Y. Min, L. Chen, and Y. Zhang, "Disturbance source location of forced power oscillation using energy functions," *Automation of Electric Power Systems*, vol. 34, no. 5, pp. 1–6, Mar. 2010.

[84] L. Chen, Y. Min, and W. Hu, "An energy-based method for location of power system oscillation source," *IEEE Transactions on Power Systems*, vol. 28, no. 2, pp. 828–836, May 2013.

[85] Y. Shu, X. Zhou, and W. Li, "Analysis of low frequency oscillation and source location in power systems," *CSEE Journal of Power and Energy Systems*, vol. 4, no. 1, pp. 58–66, Mar. 2018.

[86] I. Singh, V. K. R. Chiluka, D. J. Trudnowski, and M. Donnelly, "A strategy for oscillation source location using closed-contour grouping and energy-flow spectra," in *2020 IEEE/PES Transmission and Distribution Conference and Exposition*, Chicago, IL, USA, Oct. 2020, pp. 1-5.

[87] S. Feng, B. Zheng, P. Jiang, and J. Lei, "A two-level forced oscillations source location method based on phasor and energy analysis," *IEEE Access*, vol. 6, pp. 44318–44327, Aug. 2018.

[88] Y. Yu, S. Grijalva, J. J. Thomas, L. Xiong, P. Ju, and Y. Min, "Oscillation energy analysis of inter-area low-frequency oscillations in power systems," *IEEE Transactions on Power Systems*, vol. 31, no. 2, pp. 1195–1203, Mar. 2016.

[89] Z. Sun, G. Cai, D. Yang, and C. Liu, "Application of power system energy structures to track dominated oscillation paths and generator damping

contribution during low-frequency oscillations," *International Journal of Electrical Power & Energy Systems*, vol. 104, pp. 52–68, Jan. 2019.

[90] Z. Sun, G. Cai, D. Yang, C. Liu, B. Wang, and L. Wang, "A method for the evaluation of generator damping during low-frequency oscillations," *IEEE Transactions on Power Systems*, vol. 34, no. 1, pp. 109–119, Jan. 2019.

[91] L. Chen, Y. Min, X. Lu, X. Xu, Y. Li, Y. Zhang, and Q. Chen, "Online emergency control to suppress frequency oscillations based on damping evaluation using dissipation energy flow," *International Journal of Electrical Power & Energy Systems*, vol. 103, pp. 414–420, Dec. 2018.

[92] R. Xie and D. J. Trudnowski, "Tracking the damping contribution of a power system component under ambient conditions," *IEEE Transactions on Power Systems*, vol. 33, no. 1, pp. 1116–1117, Jan. 2018.

[93] H. Cai, S. Q. Bu, Z.Y. Peng, C. Wu, X. M. Yi and W. C. Qi, "Consistency of damping torque and energy flow dissipation coefficient in oscillation stability analysis," in *2018 International Conference on Power System Technology (POWERCON)*, Guangzhou, China, Nov. 2018, pp. 1-7.

[94] Y. Ren, X. Wang, L. Chen, Y. Min, G. Li, L. Wang, and L. Yin, "Component damping evaluation in sub-synchronous oscillation based on transient energy flow method," *IET Generation, Transmission & Distribution*, vol. 14, no. 3, pp. 460–469, Feb. 2020.

[95] L. Chen, M. Sun, Y. Min, X. Xu, J. Xi, and Y. Li, "Online monitoring of generator damping using dissipation energy flow computed from ambient data," *IET Generation, Transmission & Distribution*, vol. 11, no. 18, pp. 4430–4435, Dec. 2017.

[96] S. Maslennikov, B. Wang, and E. Litvinov, "Dissipating energy flow method for locating the source of sustained oscillations," *International Journal of Electrical Power & Energy Systems*, vol. 88, pp. 55–62, Jun. 2017.

[97] L. Chen, Y. Min, Y.-P. Chen, and W. Hu, “Evaluation of generator damping using oscillation energy dissipation and the connection with modal analysis,” *IEEE Transactions on Power Systems*, vol. 29, no. 3, pp. 1393–1402, May 2014.

[98] L. Chen, Y. Min, and W. Hu, “Low frequency oscillation analysis and oscillation source location based on oscillation energy. Part one: Mathematical foundation and energy flow computation,” *Automation of Electric Power Systems*, vol. 36, no. 3, pp. 22–27, Feb. 2012.

[99] L. Chen, Y. Chen, Y. Min, W. Hu, and K. Zhang, “Low frequency oscillation analysis and oscillation source location based on oscillation energy. Part two: Method for oscillation source location and case studies,” *Automation of Electric Power Systems*, vol. 36, no. 4, pp. 1–5, Feb. 2012.

[100] L. Chen, Y. Min, Y. Chen, M. Lu, and Y. Zhang, “Relationship between oscillation energy analysis and eigenvalue analysis and assessment of generator damping,” *Automation of Electric Power Systems*, vol. 37, no. 19, pp. 33–40, Oct. 2013.

[101] J. Luo, Y. Zou, S. Bu, and U. Karaagac, “Converter-driven stability analysis of power systems integrated with hybrid renewable energy sources,” *Energies*, vol. 14, no. 14, p. 4290, Jul. 2021.

[102] M. Quester, F. Loku, O. E. Azzati, L. Noris, Y. Yang, and A. Moser, “Investigating the converter-driven stability of an offshore HVDC system,” *Energies*, vol. 14, no. 8, p. 2341, Apr. 2021.

[103] L. Kong, Y. Xue, L. Qiao, and F. Wang, “Review of small-signal converter-driven stability issues in power systems,” *IEEE Open Access Journal of Power and Energy*, vol. 9, pp. 29–41, 2022.

[104] Y. Li, K. Meng, and Z. Y. Dong, “Converter-driven voltage instability in weak grid considering cross-domain impedance,” *2020 IEEE Power & Energy Society General Meeting (PESGM)*. pp. 1-5, Montreal, QC, Canada, Aug. 2020.

[105] H. Du, J. Yan, M. Ghafouri, R. Zgheib, M. Kassouf, and M. Debbabi, "Modeling of cyber attacks against converter-driven stability of PMSG-based wind farms with intentional subsynchronous resonance," *2021 IEEE International Conference on Communications, Control, and Computing Technologies for Smart Grids*, Aachen, Germany, Oct. 2021, pp. 391-397.

[106] F. Gao, X. Zheng, S. Bozhko, C. I. Hill, and G. Asher, "Modal analysis of a PMSG-based DC electrical power system in the more electric aircraft using eigenvalues sensitivity," *IEEE Transactions on Transportation Electrification*, vol. 1, no. 1, pp. 65–76, Jun. 2015.

[107] J. Li, S. Wang, L. Ye, and J. Fang, "A coordinated dispatch method with pumped-storage and battery-storage for compensating the variation of wind power," *Protection and Control of Modern Power Systems*, vol. 3, no. 1, pp. 1–14, Jan. 2018.

[108] F. R. Badal, P. Das, S. K. Sarker, and S. K. Das, "A survey on control issues in renewable energy integration and microgrid," *Protection and Control of Modern Power Systems*, vol. 4, no. 1, pp. 1–27, Apr. 2019.

[109] J. Luo, S. Bu, J. Zhu, and C. Y. Chung, "Modal shift evaluation and optimization for resonance mechanism investigation and mitigation of power systems integrated with FCWG," *IEEE Transactions on Power Systems*, vol. 35, no. 5, pp. 4046–4055, Sep. 2020

[110] H. Liu, X. Xie, J. He, T. Xu, Z. Yu, C. Wang, and C. Zhang, "Subsynchronous interaction between direct-drive PMSG based wind farms and weak AC networks," *IEEE Transactions on Power Systems*, vol. 32, no. 6, pp. 4708–4720, Nov. 2017.

[111] H. T. Mokui, M. Mohseni, and M. A. S. Masoum, "Implementation of space vector based hysteresis current control for full converter wind generation system," in *2011 IEEE PES Innovative Smart Grid Technologies*, pp. 1–7, Perth, WA, Australia, Nov. 2011.

[112] S. Feng, K. Wang, J. Lei, and Y. Tang, “Influences of DC bus voltage dynamics in modulation algorithm on power oscillations in PMSG-based wind farms,” *International Journal of Electrical Power & Energy Systems*, vol. 124, p. 106387, Jan. 2021.

[113] J. Luo, S. Bu, and C. Y. Chung, “Design and comparison of auxiliary resonance controllers for mitigating modal resonance of power systems integrated with wind generation,” *IEEE Transactions on Power Systems*, vol. 36, no. 4, pp. 3372–3383, Jul. 2021.

[114] J. Luo, S. Bu, and J. Zhu, “A novel PMU-based adaptive coordination strategy to mitigate modal resonance between full converter-based wind generation and grids,” *IEEE Journal of Emerging and Selected Topics in Power Electronics*, vol. 9, no. 6, pp. 7173–7182, Dec. 2021.

[115] P. Kundur, N. J. Balu, and M. G. Lauby, *Power System Stability and Control*. McGraw-hill New York, 1994.

[116] X.-F. Wang, Y. Song, and M. Irving, *Modern Power Systems Analysis*. New York, US: Springer, 2008.

[117] G. Rogers, *Power System Oscillations*. Norwell, MA, USA: Kluwer, 2000.

[118] S. Q. Bu, W. Du, H. F. Wang, and S. Gao, “Power angle control of grid-connected doubly fed induction generator wind turbines for fault ride-through,” *IET Renewable Power Generation*, vol. 7, no. 1, pp. 18–27, Jan. 2013.

[119] U. Karaagac, J. Mahseredjian, R. Gagnon, H. Gras, H. Saad, L. Cai, I. Kocar, A. Haddadi, E. Farantatos, S. Bu, K. W. Chan, and L. Wang, “A generic EMT-type model for wind parks with permanent magnet synchronous generator full size converter wind turbines,” *IEEE Power and Energy Technology Systems Journal*, vol. 6, no. 3, pp. 131–141, Sep. 2019.

[120] M. N. I. Sarkar, L. G. Meegahapola, and M. Datta, “Reactive power management in renewable rich power grids: A review of grid-codes, renewable

generators, support devices, control strategies and optimization algorithms," *IEEE Access*, vol. 6, pp. 41458–41489, May 2018.

[121] E. V. Larsen, "Wind generators and series-compensated AC transmission lines," in *2012 IEEE Power and Energy Society General Meeting*, pp. 1-4, San Diego, CA, USA, Jul. 2012.

[122] H. T. Ma, P. B. Brogan, K. H. Jensen, and R. J. Nelson, "Sub-synchronous control interaction studies between full-converter wind turbines and series-compensated AC transmission lines," in *2012 IEEE Power and Energy Society General Meeting*, pp. 1-5, San Diego, CA, USA, Jul. 2012.

List of Publications

1. Yong Hu, Siqi Bu, Bin Zhou, Yi Liu, and Cheng-Wei Fei, "Impedance-based oscillatory stability analysis of high power electronics-penetrated power systems—A survey," *IEEE Access*, vol. 7, pp. 120774–120787, Aug. 2019.

2. Yong Hu, Siqi Bu, Xin Zhang, Chi Yung Chung, and Hui Cai, "Connection between damping torque analysis and energy flow analysis in damping performance evaluation for electromechanical oscillations in power systems," *Journal of Modern Power Systems and Clean Energy*, vol. 10, no. 1, pp. 19–28, Jan. 2022.

3. Yong Hu, Siqi Bu, Shijun Yi, Jiebei Zhu, Jianqiang Luo, and Yanli Wei, "A novel energy flow analysis and its connection with modal analysis for investigating electromechanical oscillations in multi-machine power systems," *IEEE Transactions on Power Systems*, vol. 37, no. 2, pp. 1139–1150, Mar. 2022.

4. Yong Hu, Siqi Bu, and Jianqiang Luo, "Application of energy flow analysis in investigating machine-side oscillations of full converter-based wind generation systems," *IET Renewable Power Generation*, vol. 16, no. 5, pp. 900–911, Apr. 2022.

5. Yong Hu and Siqi Bu, "Generalization of energy flow analysis for investigating various oscillations in power electronic converter-penetrated power systems," Ready for Submission.

6. Siqi Bu and Yong Hu, "Method, appliance, equipment and storage medium for monitoring the damping of wide-band oscillations in power systems," China Patent (in Chinese), Under Review.

7. Siqi Bu and Yong Hu, "Method, appliance, equipment and storage medium for suppressing wide-band oscillations in power systems," China Patent (in Chinese), Under Review.

8. Yong Hu and Siqi Bu, “A novel energy flow analysis and its connection with modal analysis for investigating electromechanical oscillations in multi-machine power systems,” *2022 IEEE Power & Energy Society General Meeting*, Denver, CO, USA, Jul. 2022.

9. Yi You, Yong Hu, and Siqi Bu, “PMU data issues and countermeasure techniques in cyber-physical power systems: A survey,” *2021 IEEE Sustainable Power and Energy Conference (iSPEC)*, Nanjing, China, Dec. 2021, pp. 4278–4285.

10. Jianqiang Luo, Siqi Bu, Jiaxin Wen, Qian Hu, Yong Hu, and Qi Wang, “Strong resonance identification and mitigation in PMSG integrated power systems,” *International Conference on Power, Energy and Electrical Engineering*, 2019.

11. Jianqiang Luo, Siqi Bu, Jiaxin Wen, Qian Hu, Qi Wang, and Yong Hu, “Parameter optimization of POM tuning in mitigating modal exclusion effect on power system small signal stability,” *The 18th HUST Annual Research Symposium*, 2019.